GNSS PRECISE POINT POSITIONING USING LOW-COST GNSS RECEIVERS

MANINDER SINGH GILL

A THESIS SUBMITTED TO FACULTY OF GRADUATE STUDIES IN PARTIAL FULFILLMENT OF THE REQUIREMENTS FOR THE DEGREE OF MASTER OF SCIENCE

GRADUATE PROGRAMME IN EARTH AND SPACE SCIENCE
YORK UNIVERSITY
TORONTO

August 2018

Abstract

There are positioning techniques available such as Real-Time Kinematic (RTK) which allow user to obtain few cm-level positioning, but require infrastructure cost, i.e., setting up local or regional networks of base stations to provide corrections. Precise Point Positioning (PPP) using dual-frequency receivers is a popular standalone technique to process GNSS data by applying precise satellite orbit and clock correction along with other corrections to produce cm to dm-level positioning.

At the time of writing, almost all low-cost and ultra-low-cost (few $10s) GNSS units are single-frequency chips. Single-frequency PPP poses challenges in terms of effectively mitigating ionospheric delay and the multipath, as there is no second frequency to remove the ionospheric delay. The quality of measurements also deteriorates drastically from geodetic-grade to ultra-low-cost hardware. Given these challenges, this study attempts to improve the performance of single-frequency PPP using geodetic-grade hardware, and to capture the potential positioning performance of this new generation of low-cost and ultra-low-cost GNSS chips.

Raw measurement analysis and post-fit residuals show that measurements from cellphones are more prone to multipath compared to signals from geodetic-grade and low-cost receivers. Horizontal accuracy of a few-centimetres is demonstrated with geodetic-grade hardware. Whereas accuracy of few-decimetres is observed from low-cost and ultra-low-cost GNSS hardware. With multi-constellation processing, improvements in accuracy and reductions in convergence time over initial 60 minutes period, are also demonstrated with three different set of GNSS hardware. Horizontal and vertical rms of 37 cm and 51 cm, respectively, is achieved using a cellphone.

Acknowledgements

First, I would like to extend my sincere gratitude to my supervisor Dr. Sunil Bisnath, for his continuous support, and the dedication and inspiration that he provided throughout this work. The late Thursday evening meetings have been of immense help, not only to move my research forward, but they also helped me to broaden my understanding and skill-set in the field of navigation and positioning. I also appreciate the valuable inputs from Garrett Seepersad and John Aggrey during this study. I would also like to acknowledge NSERC for providing the financial assistance for this research.

Last but not least, I want to acknowledge the endless support of my wife and parents without whom this journey would not have been the same.

Table of Contents

List of Tables

List of Figures

List of Acronyms

AC	Analysis Centres
C/A-code	Coarse/Acquisition code
BeiDou	China Navigation Satellite System
C/N_0	Carrier-to- noise density
DCB	Differential Code Biases
Galileo	European Navigation Satellite System
GIM	Global Ionospheric Map
GLONASS	Russian Navigation Satellite System
GNSS	Global Navigation Satellite System
GPS	Global Positioning System
GRAPHIC	GRoup And PHase Ionospheric Correction
IGS	International GNSS Service
IONEX	IONsphere map EXchange
NavIC	Indian Regional Navigation Satellite System
NRCan	Natural Resources of Canada
PPP	Precise Point Positioning
RHCP	Right hand circularly polarized
RINEX	Receiver Independent Exchange
RMS	Root mean square
RTK	Real-Time Kinematic
SF	Single-frequency
S/N	Signal-to-noise ratio
STEC	Slant total electron content
TEC	Total electron content
VTEC	Vertical total electron content
QZSS	Quasi-Zenith Satellite System
ZPD	Zenith path delay

Chapter 1 Introduction

Advancement in electronic chip manufacturing has revolutionized the Global Navigation Satellite Systems industry. The quality of the new generation of low-cost (few $100s) GNSS chips has improved drastically over a few years. Since 2016, pseudorange and carrier-phase measurements are available from devices running the Android N of higher operating system on mobile. Newer applications in autonomous navigation, sports, gaming, personal navigation make use of low-cost or ultra-low-cost GNSS hardware. These new, evolving applications are in non-traditional GNSS markets, and demand a precise solution at an affordable cost.

Development of new GNSSs and user technology over the years has brought new features and possibilities to the consumer market. With the launch of new GNSS constellations, densely spread spectra over 1146-1616 MHz and miniaturization of GNSS chipsets have played a vital role in revolutionizing the technology that is GNSS. With Precise Point Positioning (PPP), it is now possible to obtain centimetre-level accuracy using a single geodetic-grade receiver (Bisnath and Gao 2009). With the development of new features and ever-evolving applications such as gaming, autonomus navigation, etc., there is a demand from the consumer market to provide high-accuracy (few cm-dm level) positioning solution at a lower cost.

To obtain high-accuracy positioning solution from low-cost (few $100s) and ultra-low-cost (few $10s) GNSS receivers, calls for careful accounting of measurement errors in particular ionospheric refraction and multipath signals. This research will focus on using low-cost and ultra-low-cost GNSS receivers with only L1 and C/A-code measurements. PPP using low-cost GNSS receivers requires different mathematical models from that of typical dual-frequency, which involves

assigning different weights in the single-frequency estimation process. Further, the stochastic weighting scheme in the estimation process changes from geodetic to ultra-low-cost GNSS hardware, purely because of the quality of raw measurements degrades as one moves from geodetic receivers to ultra-low-cost GNSS receivers. In addition, biases in the low-cost hardware measurements are larger, thus affecting the convergence behaviour and accuracy of the single-frequency PPP solution. Therefore, the objectives of this research are to (1) investigate and compare the positioning solution from geodetic-grade GNSS hardware with those from ultra-low-cost and low-cost GNSS hardware, and (2) improve the capability and performance of PPP using low-cost and ultra-low-cost hardware by efficiently mitigating the ionospheric refraction and assigning optimal weights in the estimation process.

1.1 Motivation for research

Over the last few years, the positioning landscape in the automotive, agricultural, fleet tracking, and gaming industries is changing very rapidly. All major automotive manufacturers are working towards autonomous vehicles, and use sensor such as GNSS chips, IMUs, LIDARs, etc. in complex decision-making required for safe navigation. A high accuracy and robust positioning solution is required for complex tasks, such as lane detection and changing. Positioning techniques such as Real Time Kinematic (RTK), can provide a few cm-level accuracy, but require a dense network of stations to transmit corrections. Such infrastructure of GNSS stations costs millions of dollars.

PPP is another alternate positioning technique which does not rely on another station to mitigate the atmospheric errors. Over the last couple of decades, dual-frequency PPP has been extensively researched and studied in academia, government agencies and in GNSS industry. Numerous PPP positioning engines have been developed over the years, demonstrating few cm-level accuracies

in both static and kinematic mode (Kouba and Héroux 2001; Bisnath and Gao 2009; Landau et al., 2009; Banville, 2014; Aggrey 2015; Laurichesse and Blot 2016).

Low-cost (few $100s) and ultra-low-cost (few $10s) GNSS chips are predominately used in the autonomous navigation (cars and UAVs), sports, wrist-bands, gaming, personal navigation, etc. It is estimated that approximately 99% of the GNSS receivers are single-frequency units, and at the time of writing almost all low-cost and ultra-low-cost (contained in cellphones) GNSS receivers are single-frequency chips. PPP with L1-only data from geodetic-grade and low-cost receivers has also been investigated by Beran et al. (2003); Chen and Gao (2005); Choy (2009); Cai et al. (2017). Single-frequency PPP faces numerous challenges in terms of dealing with ionospheric delay and multipath. The quality of raw measurements from ultra-low-cost receivers is also quite poor compared to the geodetic-quality measurements (Riley et al. 2018; Gill et al. 2017). Different mathematical models are required in the filtering process to consider the quality of measurements, and to appropriately mitigate the multipath. In this research, an attempt is made to compare the quality of raw measurements from three different grades of receivers and optimal filtering techniques are also presented for data processing from each set of hardware. Positioning performance from all three grades of hardware is also compared.

Because of the high-accuracy positioning solution with low-cost and ultra-low-cost could provide a multitude of benefits and will also help in emerging applications in the new fields. The primary motive of this study is to investigate an alternate, low positioning infrastructure, and cost-effective positioning technique which could be effectively used with geodetic-grade, low-cost and ultra-low-cost GNSS hardware.

1.2 Research objectives

At present, as discussed above, the vast majority of GNSS receivers are single-frequency. Low-cost and ultra-low-cost GNSS chips are finding their way into the automotive industry and in to consumer hand-handheld devices. In 2016, Google announced that raw pseudorange and carrier-phase measurements can be accessed from a few models of tablets and cellphones operating Android N or higher (Banville and Van Diggelen, 2016). The goal of this research is to develop and refine algorithms for single-frequency PPP, which are not only suitable for the geodetic applications but also adaptable to produce a best possible PPP solution using low-cost and ultra-low-cost GNSS chips. In order to achieve this aim, the following research objectives are formulated:

Adding a multi-constellation, single-frequency processing capability to the YORK-PPP software. Implementation of an extended Kalman filter along with different process and observation models, for different hardware and applications. The software development is done keeping in mind the modularity and scalability of the PPP software.

1. Analysis and comparison of the raw observations from geodetic-grade, low-cost and ultra-low-cost hardware.
2. Assessment of uncombined and combined single-frequency PPP solution from three different grades of hardware.
3. Comparison of GPS-only solutions from a tablet to the combined GPS + GLONASS solutions.

1.3 Thesis organization

Chapter 1 provides the introduction, research objectives and motivation to this research. Chapter 2 provides the background of the study, an overview of GNSS, along with different positioning modes with the brief description of the relevant error sources. Classification of different grades of GNSS receivers is also discussed. Chapter 3 explains the process and measurement models for single-frequency Precise Point Positioning (PPP). It also discusses the different methods to obtain a single-frequency PPP solution. Chapter 4 gives a description of the research software and then discusses the quality control algorithms/procedures used within the PPP software. The chapter ends with a description of available methods to mitigate the ionospheric delay. Chapter 5 examines the single-frequency PPP solution from geodetic, low-cost and ultra-low-cost hardware. The focus is on comparing various solutions (to be described later) using an uncombined filter and the so-called GRAPHIC linear combination. This chapter concludes with the comparison of GPS-only solutions from ultra-low-cost hardware to GPS + GLONASS. Chapter 6 concludes the findings of this study and also provides recommendations for the future work.

Chapter 2 Background

The technique of finding position of points on the Earth's surface using distant objects such as Sun, stars, planets has been used for centuries. However, it was only in the space age that it became possible to develop a sophisticated satellite system for high accuracy positioning and navigation, which not only provided global coverage, but also could be used anytime, and in all-weather conditions. The US Navy Navigation Satellite System, Transit, was the world's first satellite-based positioning system to operate globally, and was based on Doppler shift measurements of a signal as the satellite transited with a navigational accuracy of 25-500 m (Langley et al., 2017).

The Global Positioning System (GPS) was introduced in 1978 and has much superior performance to Transit. This new system (GPS) was based on using the range measurements and has a different constellation design than the Transit, offering global, 24-hour continuous coverage for military users and reduced accuracy for civilian users. Since then, it has become the backbone of a whole body of navigation and positioning technologies. During the 1980s, the USSR also launched Global'naya Navigatsionnaya Sputnikova Sistema (GLONASS), the second fully operational global navigation satellite system.

At the time of writing, the U.S., Russia, the European Union (E.U) and China are operating and developing their individual Global Navigation Satellite Systems (GNSS's): GPS, GLONASS, Galileo and BeiDou, respectively. India and Japan have their individual Regional Navigation Satellite Systems (RNSS's): NavIC and QZSS, respectively. All GNSSs and RNSSs are radio-positioning and time transferring systems, that use the ranging measurements. To compute a position, a GNSS receiver and antenna are required at the user's end, which measures the time required for the GNSS signal to propagate from a satellite to the receiver (Leick et al. 2015).

Having multiple GNSSs and RNSSs can provide multitude of benefits to users in terms of improving accuracy, robustness, and ability to navigate and position in environments with limited satellite visibility. This chapter provides a brief description of each GNSS and each RNSS. Measurement types and available positioning modes along with the error sources are also discussed. Since this research was focused on the PPP using low-cost (single-frequency) GNSS hardware, the research that has already been done in single-frequency PPP is also presented.

2.1 Overview of GNSS

The current navigation system can be grouped into two broad categories:

- Systems providing global coverage, called Global Navigation Satellite Systems (GNSS).
- Systems providing regional coverage, referred as Regional Navigation Satellite Systems (RNSS).

GNSS signals are electromagnetic waves travelling at the speed of the light. GNSS signal frequencies fall in the spectrum between about 1.1 and 1.6 GHz (L-band). This bandwidth is selected for these signals since these enable measurements of adequate precision, allows for reasonably simple user equipment and does not suffer from significant attenuation in the atmosphere under challenging weather conditions. GNSSs provide signals on at least two different frequencies to compensate for the ionospheric error (Langley et al. 2017).

GNSS constellations typically adopt a Medium Earth Orbit (MEO) configuration, as this configuration is most suitable for the continuous global coverage. Inclined geosynchronous orbits (IGSO) and geostationary orbits (GEO) are also employed, especially in the regional systems.

An overview of each GNSS is provided in Table 2.1. All GNSSs are described in details by (Hegarty 2017; Revnivykh et al. 2017; Falcone et al. 2017; and Yang et al. 2017).

GNSS	**GPS**	**GLONASS**	**Galileo**	**BeiDou**	**IRNSS/NavIC**	**QZSS**
Number of SVs	24 (MEO)	24 (MEO)	30 (MEO)	27 (MEO), 3 (IGSO), 5 (GEO)	4 (IGSO), 3 (GEO)	3 (IGSO), 1 (GEO)
Constellation	6 planes 56^o inclination	3 planes (Walker) 64.8^o inclination	3 planes (Walker) 56^o inclination	3 planes (Walker) 55^o inclination	IGSO with 29^o inclination	IGSO with 43^o inclination
Initial Service	Dec 1993	Sep 1993	2017	Dec 2012	2016	2018 (planned)
Coverage	Global	Global	Global	Global	East Asia, Oceania region	$-30^o < \phi < 50^o$ $30^o < \lambda < 130^o$
Origin	USA	Russia	Europe	China	India	Japan
Frequency (MHz)	L1 1575.42 L2 1225.60 L5 1176.45	L1 1602.00 L2 1246.00 L3 1202.025	E1 1575.42 E5a 1176.45 E5b 1207.14 E6 1278.75	B1 1561.098 B2 1207.14 B3 1268.52	L5 1157.45 S 2492.028	L1 1575.42 L2 1227.60 L5 1176.45 E6 1278.75

Table 2.1: GNSS, RNSS and their major characteristics (Langley et al. 2017)

2.2 Measurement types

Each GNSS, RNSS allows for receivers to basic types of measurements:

Doppler: The change in the received frequency caused by the Doppler effect is a measure of the range-rate or line-of-sight velocity.

Pseudorange: It is a binary signal and has the time-stamp when it is transmitted from the satellite. It is a measure of the difference between the receiver clock at signal reception and the satellite clock at signal transmission, scaled by speed to light. Its precision is of the decimetre-level with geodetic-grade hardware.

Carrier-phase: It is a sinusoidal wave at a given frequency and has a period of less than 1 m which allows for precise measurements. A measure of the instantaneous beat phase and the accumulated number of zero-crossings obtained after mixing with a reference signal of the nominal frequency. In case of interrupted tracking, the accumulated cycle count is lost, and this phenomenon is known as a cycle slip.

2.3 Measurement processing modes

Depending on the application and accuracy requirements, various GNSS positioning modes of different degrees of complexity, precision and accuracy are available. These range from standard single-frequency pseudorange-based positioning, used by most consumer receivers, including those in cellphones, high-integrity methods for safety-of-life applications to sophisticated multi-frequency, carrier-phase-based techniques capable of a centimetre to the sub-centimetre level of accuracy. This section gives brief descriptions of these techniques. For the sake of simplicity, only the basic point positioning model is presented. For the full treatment of positioning modes

including all error sources, reader can refer to, e.g., Teunissen and Montenbruck (2017); Hofmann-Wellenhof et al. (2007); Kaplan and Hegarty (2006).

2.3.1 Single point positioning

Single point positioning is the most basic form of satellite-based positioning technique. The navigation solution is a least-squares estimate of the measurement equations made at a single epoch. For each satellite the basic observation equation is written as:

$$R_{rec}^{i} = \rho_{rec}^{i} + c(dt^{s} - dt_{rec}) \tag{2.1}$$

where R_{rec}^{i} is the measured pseudorange between receiver *rec* and a satellite *i*, dt^{s} dt_{rec} are the satellite and receiver clock offset from the GPS time, *c* is the speed of light and ρ_{rec}^{i} is the geometric range between a satellite *i* and a receiver.

$$\rho_{rec}^{i} = \sqrt{(X-x)^2 + (Y-y)^2 + (Z-z)^2} \tag{2.2}$$

X, Y, Z are the receiver coordinates in the ECEF frame and x, y, z are the particular satellite coordinates.

Since the observation equation is non-linear in the unknowns, to solve the problem efficiently, the model is to be linearized about the reference state $(X^0 + Y^0 + Z^0 + dt_{rec}^0)$. Once the model is linearized, the least-squares solution can be estimated iteratively as:

$$x = x_0 + \delta \tag{2.3}$$

$$\delta = (H^T P_l H)^{-1} H^T w \tag{2.4}$$

Where x is the state estimate at the current time and x_0 is the apriori estimate, H is known as the Jacobian matrix consists of partial derivates of the observations with respect to the unknowns, and w is the misclosure vector.

$$H = \begin{bmatrix} \frac{dR_{rec}^1}{dX} & \frac{dR_{rec}^1}{dY} & \frac{dR_{rec}^1}{dZ} & 1 \\ \frac{dR_{rec}^2}{dX} & \frac{dR_{rec}^2}{dY} & \frac{dR_{rec}^2}{dZ} & 1 \\ \cdots & \cdots & \cdots & \cdots \\ \frac{dR_{rec}^n}{dX} & \frac{dR_{rec}^n}{dY} & \frac{dR_{rec}^n}{dZ} & 1 \end{bmatrix} \tag{2.5}$$

$$w = \begin{bmatrix} R_{rec}^1 - \rho_{rec}^1 \\ R_{rec}^2 - \rho_{rec}^2 \\ \cdots \\ R_{rec}^n - \rho_{rec}^n \end{bmatrix} \tag{2.6}$$

If no stochastic information is available, the weight (P_l) or covariance matrix can be assumed as an identity matrix:

$$P_l = I$$

The measurement partial in the Jacobian matrix are also known as the direction cosines:

$$\frac{dR}{dX} = \frac{X - x_0}{\sqrt{(X - x_0)^2 + (Y - y_0)^2 + (Z - z_0)^2}} = \frac{X - x_0}{\rho_0}$$
$$\frac{dR}{dY} = \frac{Y - x_0}{\sqrt{(X - x_0)^2 + (Y - y_0)^2 + (Z - z_0)^2}} = \frac{Y - y_0}{\rho_0}$$
$$\frac{dR}{dZ} = \frac{Z - z_0}{\sqrt{(X - x_0)^2 + (Y - y_0)^2 + (Z - z_0)^2}} = \frac{Z - y_0}{\rho_0}$$

(x_0, y_0, z_0) are the approximate receiver coordinates. Post-fit residuals are calculated as follows:

$$r = w - H\delta \tag{2.7}$$

2.3.2 Differential positioning

Differential positioning with GNSS is commonly known as DGNSS is a positioning technique where two or more receivers are used. The receiver usually at rest is known as the base station and is normally set up at a location with known coordinates. On the other hand, the receiver for which position needs to be determined is called the rover station (see Figure 2.1).

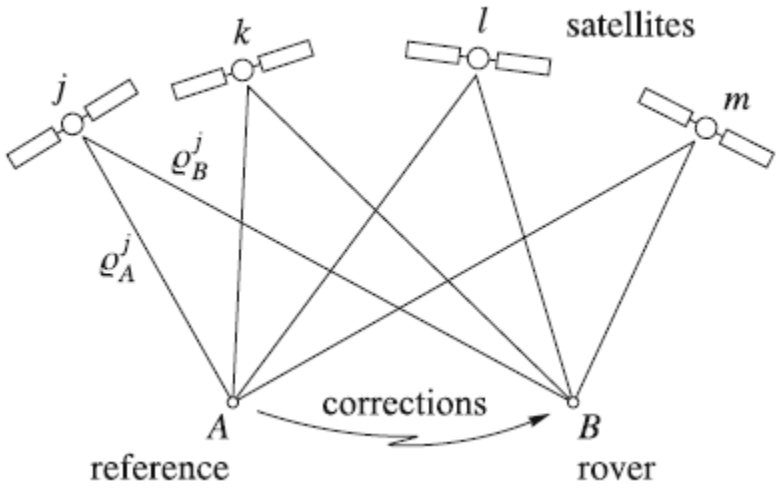

Figure 2.1: Rover and base station setup

Pseudorange corrections (PRC) and range rate corrections (RRC) are calculated at the reference station and then transmitted to the rover station typically using a radio link in real-time. The remote receiver applies the corrections to the measured pseudoranges and then performs basic point-positioning with the corrected pseudoranges (Kaplan, 1996).

$$R_{rec}^{i} = \rho_{rec}^{i} + \Delta\rho_{rec}^{i} + \Delta\rho^{i} + \Delta\rho_{rec} \tag{2.8}$$

where ρ_{rec}^{i} is the geometric range, $\Delta\rho_{rec}^{i}$ represents the biases based on the reciever and the satellite position, e.g., atmospheric delays, orbital errors, $\Delta\rho^{i}, \Delta\rho_{rec}$ represents the biases based on the satellite and the receiver position respectively. PRC for satellite *i* is calculated as below and then transmitted to the rover receiver:

$$PRC^i = \rho^i_{rec} - R^i_{rec} = -(\Delta\rho^i_{rec} + \Delta\rho^i + \rho_{rec}) \tag{2.9}$$

Metre-level positioning accuracy can be achieved using the DGNSS mode. DGNSS can be augmented with carrier-phase observations and sub-metre level of accuracy can be achieved. The interested reader can refer to Hofmann-Wellenhof et al. (2007) for the full treatment of carrier-phase-based DGSS.

2.3.3 Relative positioning

Relative positioning is a technique in which baseline vector between two points is determined (see Figure 2.2). The aim of relative positioning is to determine the location of the unknown point with respect to the location of the known point. If the position vectors are X_A, X_B, the relation is given as:

$$X_B = X_A + b_{AB} \tag{2.10}$$

Components of the baseline vector b_{AB}:

$$b_{AB} = \begin{bmatrix} X_B - X_A \\ Y_B - Y_A \\ Z_B - Z_A \end{bmatrix} \tag{2.11}$$

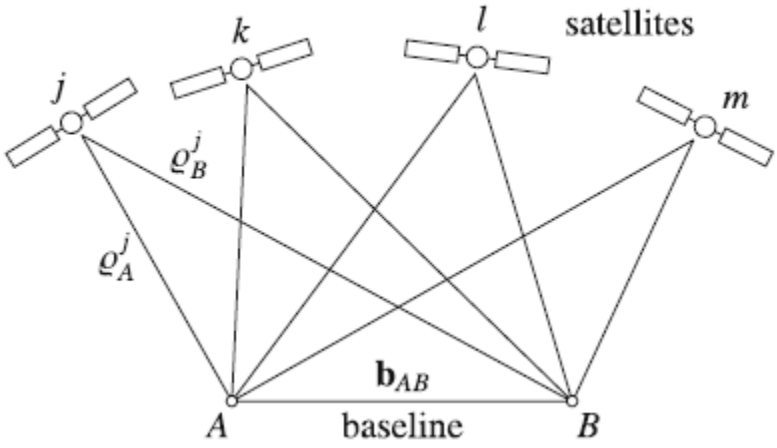

Figure 2.2: Relative positioning concept Source: (Hofmann-Wellenhof et al. 2007)

Relative positioning can be performed with code-only ranges or using both code and carrier-phase measurements. However, because of the higher precision of the phase measurements, carrier-phase measurements are commonly employed in relative positioning for higher accuracy and precision.

Relative positioning can be further sub-divided into following categories:

- Single-differencing
- Double-differencing
- Triple-differencing

Double-differencing is a most commonly employed mode of relative positioning, which cancels out the biases related to the receiver and the satellites. Centimetre-level of horizontal accuracy can be achieved using double differencing.

2.3.4 Precise Point Positioning (PPP)

Precise Point Positioning (PPP) was first introduced in 1997, which makes use of undifferenced carrier-phase and pseudorange observations (Zumberge et al. 1997). Unlike the traditional relative positioning techniques, PPP does not require simultaneous observations at two stations. PPP, is a natural extension to the GNSS pseudorange-based single-point positioning, which replaces the broadcast satellite clock and orbit with the precise estimates (Kouba and Héroux 2001). Use of carrier-phase observations, introduces the initial phase ambiguities unknowns, causing a few tens of minutes of convergence time for a PPP solution. This initial convergence depends on several factors, such as geometry and number of visible satellites, observation quality, environment, etc.

PPP is considered a cost-efficient technique which allows for sub-centiemetre horizontal accuracy with a single GNSS receiver. PPP's applications has been extended to the commercial sector, such

as agriculture industry for precision farming, autonomous navigation, gaming, and mapping (Bisnath and Gao 2009). The basic observation equation for PPP are presented in Chapter 3.

2.4 Error Sources

PPP is based on un-differenced observations, so common mode errors do not cancel out. In order to achieve few cm-dm level accuracy, additional corrections must be applied to the pseudorange and carrier-phase measurements. This section lists and briefly describes all the corrections that are applied in the single-frequency PPP observation model.

Atmospheric errors

Earth atmosphere mainly consists of the troposphere and the ionosphere. In both media, electromagnetic signals are refracted, which needs to be corrected to enable accurate positioning and timing applications (Teunissen and Montenbruck 2017).

Tropospheric delay

The troposphere extends to approximately 50 km into the atmosphere from the surface of Earth. The dry component of the troposphere causes ~ 90% of the delay, whereas only ~10% of the delay is caused by the wet component of the troposphere. It is difficult to completely remove the tropospheric delay because it depends on the atmospheric temperature, pressure, humidity, receiver altitude, and satellite elevation angle.

The delay caused by the dry and the wet components of the troposphere is usually modelled at the zenith angle and then scaled by an appropriate mapping function to any satellite elevation angles. Therefore, the total tropospheric delay can be expressed in an equation as the combination of the delay caused by the dry and the wet components (Choy 2009; Shen 2002).

$$d_{trop} = M_{dry} d_{dry} + M_{wet} d_{wet} \tag{2.12}$$

where:

d_{dry}: ZPD caused by dry component

d_{wet}: ZPD caused by wet component

M_{wet}, M_{dry} : Wet and dry mapping functions, respectively.

Various tropospheric models such as Hopefield and Sasstamoinen and mapping functions such as Niell Mapping Functions (NMF) and Isobaric Mapping Functions (IMF) have been developed over the years. More in-depth analysis of the troposphere can be found in (Aggrey 2015; Seepersad 2012; Choy 2009; Kouba and Héroux 2001). In this research, the wet component is estimated with other parameters in PPP processing to reduce the residuals of the wet troposphere delay, as suggested by Kouba and Héroux (2001).

Ionospheric delay

The ionosphere is the uppermost layer of the atmosphere which extends from 50 km to 1000 km from the surface of the Earth. The main constituents are O, O_2, N, N_2, NO. In this region, the density of electrons is high enough to influence the propagation of the electromagnetic waves (Choy 2009; Teunissen and Kleusberg 1996). The density of the electrons primarily dependent on solar activity, the Earth's magnetic field, as well as the location of the user (Misra and Enge 2006). Ionosphere ranging error can vary from few metres to twenty metres within a day, which depends on the time, user location and variations in the ionosphere (Wells et al. 1999).

The ionosphere is a dispersive medium, whereby the refraction is dependent on the signal frequency passing through it. The ionosphere delay can be defined as being inversely proportional to the square of the transmission frequency. Thus, dual-frequency GPS receivers can measure and remove the ionospheric effect by forming the dual-frequency, ionosphere-free linear combination.

Single-frequency GNSS users have to rely on an external ionospheric product or model to mitigate the ionospheric delay as there is no second frequency to form the ionosphere-free linear combination. The accuracy of these ionospheric models is critical to achieving high accuracy PPP solution (Choy 2009).

Antenna phase centre offset and variation

Receiver Antenna: The receiver electrical phase centre is not aligned with the physical centre of the antenna. For any given GNSS antenna, the variation of the phase centre depends on the changing direction of the incoming GNSS satellite signals, and it is a function of the antenna phase pattern, known as phase centre variations (PCV). The receiver antenna phase centre offset can cause positioning error up to 10 cm in the vertical component and a few centimetres in the horizontal component (Mader 1999).

Satellite Antenna: It originates from the separation between the GNSS satellite centre of mass and the electronic phase centre of its antenna. Force models used by IGS community for satellite orbit modelling refer to the satellite centre of mass. Subsequently, the resulting IGS precise satellite orbit and clock correction products also refer to the satellite centre of mass, and not the antenna phase centre (Zhu et al. 2003).

Phase wind-up

The relative orientation of the transmission and the receiver antennas is important because signals emitted by GNSS satellites are circular polarized. Phase wind-up is an effect that arises from the relative orientation change of a GNSS satellite's antenna with respect to the receiver's antenna. The effect of phase wind-up is modelled as an angle between effective dipoles of receiver and satellite antennas. Phase wind-up correction is only applied to the carrier-phase measurements, which is typically between the range of 0 to 5 cm (Kouba and Héroux 2001; Mander 2011).

Relativistic effects

Technologies of the clocks in GNSS has reached a state where the precision of the measurements is on the order of nanoseconds (Teunissen and Montenbruck 2017). To attain this kind of accuracy corrections must be applied to correct for the relativistic effects. Three types of relativistic effects must be considered:

Sagnac effect: It takes into account the rotation of earth during the time of flight of GNSS signal. The Sagnac effect is a correction for adapting the dilation of time caused to a clock, carried by a rotating object on non-inertial frames (Seepersad 2012).

Periodic clock error: Since the GNSS orbits are not truly circular, there is always an eccentricity which causes the orbit to be slightly elliptical. Thus, the velocity of GNSS satellite varies slightly over one revolution which causes an additional periodic error that varies with the satellite position in its orbit. This effect cancels out in relative positioning but using PPP, one must take into account the relativistic correction to the satellite clock time as suggested in the GPS Interface Control Document (Choy 2009).

Fixed frequency offset effect: The effects of the gravitational potential, velocity of rotation and the gravitational potential of the rotating geoid must also be considered. The net effect of the time dilation and gravitational redshift is that the satellite clock appears to run faster by approximately $38\frac{\mu s}{d}$, compared to the similar clock the Earth's surface (Teunissen and Montenbruck 2017). This effect is removed by giving a slight offset to the GNSS satellite clock prior to the launch.

Solid Earth tide

The "solid" Earth is far from rigid and is pliable enough to respond to the same gravitational forces that generate the ocean tides. Tides are caused by the gravitational attraction and temporal

variations of the Sun and Moon orbital motion. While the ocean tides are strongly influenced by the coastal outlines, the solid Earth tides can be computed quite accurately from simple Earth models (Leick et al. 2015). The effect of tidal variation is larger in the vertical component and can reach as much as 30 cm and 5 cm in the radial and the north directions (Kouba and Héroux 2001).

Ocean loading

The ocean loading is the deformation of the sea floor and adjacent land responding to the redistribution of seawater which takes place during the ocean tide (Witchayangkoon 2000). Ocean tides can be measured at the beach from rising and falling with respect to the benchmark. Ocean loading is more localized compared to the solid Earth tides, i.e., for stations that are located far from the ocean (>1000 km) with the point positioning at 5 cm level, or static positioning over 24 hour periods, the ocean loading can be safely ignored (Kouba 2009). However, this effect needs to be considered for stations that are located along the coastline with an observation length shorter than 24 hours. Otherwise, this error will be mapped into the tropospheric ZPD and station clock solution. The magnitude of the surface displacement caused by the ocean tide loading can reach up to 5 cm in the height and 2 cm in the horizontal component (Kouba and Héroux 2001).

Polar tides

Polar tides are caused by the motion of the Earth's spin axis with respect to the Earth's crust, i.e., polar motion. This correction needs to be subtracted from the position solution in order to be consistent with the ITRF frame and achieve centimetre level of precision. The displacement due to polar tide can reach up to 25 mm in the up component and about 7 mm in the horizontal components (Kouba 2009).

Differential code biases

L1-L2 (P1-P2) DCBs: The difference between L1 and L2 frequencies which are consistent with the P1 and P2 pseudorange measurements, hence the term P1-P2. In general, the satellite DCBs are nearly constant in time, but differ from satellite to satellite. The magnitude of the bias can reach up to 12 ns. If left unaccounted, this may have detrimental effects on the estimated PPP solutions (Aggrey 2015; Choy 2009).

The IGS ACs use ionosphere-free (IF) formulation to produce the satellite clock correction products. In un-combined dual-frequency PPP and in single-frequency PPP, users must apply the satellite L1-L2 DCBs when applying IGS-type clock corrections. This correction can be applied to the range, by first correcting for IGS satellite clocks in order to be compatible with the single-frequency observations (Kouba 2009).

P1-C1 DCBs: The P1-C1 DCBs are the differences between the code observations. Almost all low-cost and ultra-low-cost GNSS receivers do not output P1 measurements and are only limited to the C/A-code measurements. Since, the IGS orbit and clock products are generated using IF formulation, and to avoid introducing biases into the C/A-code observations, P1-C1 DCBs are required. The magnitude of the P1-C1 biases is quite constant, i.e., in the order of 2 ns (60 cm), but they are unique for each satellite and receiver. The values of the P1-C1 biases are estimated by the IGS ACs as part of their precise satellite correction estimation process. These biases can be obtained from the IGS ionospheric maps (Seepersad 2012).

Multipath

Multipath is the error caused by the reflected signals entering the front end of the receiver and masking the real direct signal correlation peak (Parkinson and Spilker 1996). It is mainly caused by the reflected GNSS signals from the near buildings, metal-posts, trees, ground, etc. These

effects tend to be more pronounced in low-cost and ultra-low-cost GNSS receivers near large reflecting surfaces, where the error could grow up to few metres for C/A-code observations and up to few cm for the carrier-phase measurements (Georgiadou and Kleusberg 1988).

Multipath is effectively mitigated by geodetic-grade antennas through the rejection of LHCP signals or reducing the contribution from few types of reflections, e.g., signal bounced from the ground below the antenna. However, because of the cost constraints and absence of such techniques in the low-cost and ultra-low-cost GNSS antennas, observations coming from low-end receivers tend to suffer more from multipath effect, e.g., inability of low-end hardware to distinguish between RHCP and LHCP signals (Rao 2013). The most effective way to mitigate the multipath effect is to place the GNSS antenna away from the reflecting objects**.** Mulitpath can also be mitigated at the receiver end by making GNSS reciever discriminator design less senstive to multipath, for example, by a narrower early-late correlator spacing.

It is also known that low elevation observations are generally more susceptible to multipath effects and the atmospheric refraction than those at high elevation angles, thus affecting the quality of the solution, particularly the vertical component (Rothacher et al. 1996). So, elevation dependent weighting is applied in this study to mitigate the multipath effect as well as the atmospheric errors.

New GNSS signals such as the GPS L5 and Galileo E5a, E5b and E5 are less vulnerable to code-phase mulitpath compared to GPS L1 C/A-code (Kaplan and Hegarty 2006).

Receiver noise

Receiver noise becomes apparent in the low-cost and ultra-low-cost GNSS receivers. Receiver noise is considered as white noise and has zero mean over time. The receiver noise is primarily due to the high-frequency thermal noise along with the effects of dynamic stresses on the tracking

loop. The noise level is a function of the code correlation method, receiver dynamics, and signal strength which varies with the satellite elevation angle (Maybeck 1982; Misra and Enge 2006; Wang 2006). Low-end receiver noise level is generally in the range of few decimetres to metres level; whereas, the noise on the carrier-phase is of the order of few centimetres to decimetres level.

2.5 Current state of single-frequency PPP research

Initially, all the single-frequency PPP processing was based on just using the code observations. Øvsteal (2002) has examined a number of empirical ionospheric models and identified the usefulness of Global Ionospheric Maps (GIMs) in single-frequency point positioning. GIMs are routinely estimated as an additional product by the IGS Analysis Centers (ACs), which contains the information about ionospheric refraction. He observed that by using high-quality, single-frequency measurements, horizontal accuracy of better than 1 m and vertical accuracy of approx. 1 m can be achieved.

Gao et al. (2005) investigated the real-time single-frequency PPP using undifferenced code and phase observations. In their research, they estimated ionospheric gradient parameters – method suggested by Chen and Gao (2005). Positioning accuracy of decimetre to sub-metre was reported. Beran et al. (2005) has also investigated high-accuracy point positioning with single-frequency receivers. Their tecnhique to process observations was based on using pesudorange and time-differenced carrier-phase measurements in a sequential least-squares filter. Ionospheric error was mitigated using ionopsheric delay grid maps and the pseudorange mulitpath was handelled by appropraite stochastic modelling. Horizontal accuracy of 2-decimetre, and 3-decimetre in vertical component were acheieved with geodetic-grade hardware. The authors also processed data from low-cost (< $100) GPS receiver, and horizontal accuracy of few decimetre-level accuracy was reported.

Tiberius et al. (2006) studied error sources in single-frequency PPP and reviewed various approaches to mitigate the errors. To process observations, the authors compared results from a phase-adjusted pseudorange algorithm developed by (Teunissen 1991), and phase-connected algorithm discussed in (Bisnath et al. 2002). Final IGS orbit and clock products were used to mitigate the satellite orbit and clock errors, and final CODE GIMs were used to remove the bulk of ionospheric delay. The authors reported that with phase-adjusted algorithm accuracy of 0.5 m in horizontal and 1 m in vertical could be achieved in static mode, and approximately 2 dm in the horizontal accuracy and 5 dm for vertical could be achieved with high dynamics using a geodetic-grade GNSS receiver and antenna.

Simsky (2006) developed a new algorithm called Dynamic Ambiguities Real-Time Standalone Single Frequency (DARTS-SF) (Simsky 2006). This algorithm was based on the joint processing C/A-code and carrier-phase observations in a Kalman filter. The central idea of his approach is to use the iono-free carrier-phase observable, in which ionospheric delay is accounted for. The ambiguities are not assumed constant and were allowed to change from epoch to epoch. Horizontal accuracy of 1 m and vertical accuracy of 1.5 m were observed.

Choy (2009) performed single-frequency PPP with different grades of hardware, i.e., geodetic-grade, medium-cost and low-cost hardware. Her approach was based on using quasi-phase (iono-free) observable as carrier-phase observation. Author reported that accuracy of 0.1- 0.9 m could be achieved in the post-processing mode. van Bree et al. (2012) reported that with real-time orbit and clocks products along with predicted global ionospheric maps (GIM), positioning accuracies of under 1 m can be achieved with medium-cost hardware (few $100s). However, with the

geodetic-grade equipment, the accuracies of 0.30 m. in horizontal and 0.65 m in vertical can be achieved in the kinematic mode.

Pesyna et al. (2014) reported that cm level accuracy is possible to obtain with cell-phone grade receiver and antenna in the carrier-phase relative positioning. Researchers have also reported that poor antenna suppression and irregular gain pattern in the cellphone antenna cause the large time correlated errors. Kirkko-Jaakkola et al. (2015) demonstrated that in Real-Time-Kinematic mode (RTK) position accuracy of 0.5 m can be achieved with a commercial off-the-shelf (COTS) low-cost GNSS receiver (< $100).

Single-frequency PPP with GPS, GLONASS, Galileo, BeiDou (quad-constellation) and GIM data were investigated by Cai et al (2017). Measurements from all four constellations were processed simultaneously. Model developed by authors is also applicable to process observations from single, dual or triple constellations. Quad-constellation PPP results showed an improvement in the convergence time by 56%, 47%, 41% in the east, north and up components compared to GPS-only single-frequency PPP.

Pan et al. (2017) also investigated the performance of Four-Constellation integrated single-frequency PPP (FCSF-PPP) with GPS, GLONASS, BeiDou and Galileo measurements. In this study, authors processed measurements simultaneously from all four constellations. Code and carrier-phase linear combination (GRAPHIC) was used to mitigate the ionospheric delay. Results indicated a significant improvement in positioning accuracy with FCSF-PPP compared to the GPS-only single-frequency PPP. Few-centimetre level of horizontal accuracy was achieved with FSCF-

PPP. de Bakker et al. (2017) reported that using low-cost GNSS hardware accuracies of 0.35 m in horizontal and 0.89 m in vertical can be achieved in real-time mode with multi-constellation GNSS. Researchers also reported that multi-constellation SF-PPP outperforms GPS-only SF-PPP in case of reduced sky visibility.

Recently, a few researchers have attempted to obtain the best possible positioning solution using raw measurements from cellphones and tablets. Banville and Van Diggelen (2016) demonstrated that with code and carrier-phase measurements, and by carefully modelling of the error sources, centimetre-level displacement of cell-phone can be achieved. Authors also emphasized that the solution obtained from the cell-phone is precise but no means accurate. Gill et al. (2017) has also investigated single-frequency PPP performance with geodetic-grade, low-cost (few $100s), and ultra-low-cost (cellphone, few $10s) GNSS hardware. Authors purposed with low-cost and ultra-low-cost hardware, uncombined measurements provide superior results to the combined measurements. Decimetre-level of horizontal accuracy with geodetic-grade, and few-decimetre to metre-level accuracy using low-cost and cellphone grade GNSS hardware were reported. Riley et al. (2018) analyzed the raw observations and positioning performance using Nexus 9 tablet with two different positioning engines. Horizontal accuracy of 1.90 m and 2.63 m was established with Trimble Code Engine and Trimble RTK Float, respectively.

Most of the single-frequency PPP research was based on L1 and C/A-code measurements from geodetic-grade hardware and only a few researchers have investigated PPP with low-cost and ultra-low-cost GNSS hardware. The quality of the GNSS chips has improved drastically over the years, and there is a need to analyse the ideal positoning performance of these new generation GNSS chips. There is also a need to compare a full a spectrum of single-frequency PPP solution that can

be obtained using different sets of GNSS hardware. Almost all single-frequency PPP reasearch prior to this was based on using GRAPHIC or GIM corrections to mitigate the inosopheric delay. In this research an attemept was made to estimate the ionopsheric delay using GIM as constraint. PPP solution using GIM, GRAPHIC and estimated slant ionospheric delay are also compared.

2.6 Classification of GNSS receivers and antennas

Cost and accuracy are the primary driving factors in selecting the GNSS hardware in almost all applications. Three different grades of GNSS hardware are compared. Figure 2.3 classifies GNSS hardware into (1) geodetic-grade (2) low-cost and (3) ultra-low-cost. As Figure 2.3 suggest, price-range of geodetic-grade GNSS hardware is ~$10,000, low-cost is between $10s- $100s and ultra-low-cost hardware falls in the range of few $10s, for single equipment purchase.

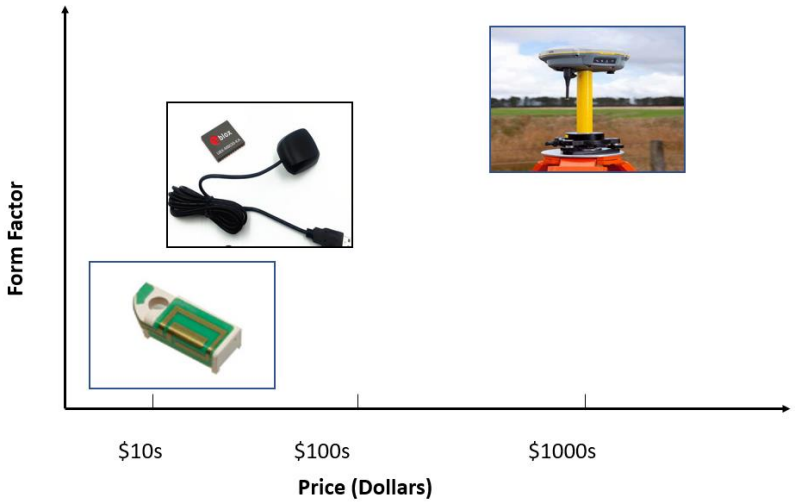

Figure 2.3: Price (and form factor) comparison of the three different grades of GNSS hardware

In this study, a NovAtel FlexPak6, u-blox NEO-M8T and Nexus 9 BCM4752 are used as an instance of geodetic-grade, low-cost and ultra-low-cost GNSS receivers, respectively (see Table 2.2).

Classification	GNSS receiver	Antenna
Geodetic-grade	NovAtel FlexPak6	Multi-point feeding
Low-Cost	u-blox NEO-M8T	Patch
Ultra-Low-Cost	Nexus 9 - Broadcom BCM4752	*n/a*

Table 2.2: Classification of three different grades of GNSS hardware used in the study

Quality and type of the GNSS antenna primarily determine the quality of raw measurements obtained from a receiver. The key parameters that define the performance of a GNSS antenna are listed (Moernaut and Orban 2009):

1. Polarization
2. Axial ratio
3. Phase centre stability
4. Antenna gain

A right-hand circular polarized (RHCP) GNSS antenna is necessary, as transmitted GNSS signals have right-hand circular polarization. Circular polarization is preferred since a linear polarized signal undergoes changes in the polarization when traveling through the Earth's Ionosphere due to the Earth's magnetic field. The other advantage to a RHCP antenna is that it discriminates between the direct signal from the satellite and multipath signals, as the polarization of reflected multipath signals are changed to left-hand circular polarization (Rao 2013).

Axial ratio defines the polarization efficiency with which the receiver antenna can receive RHCP signals transmitted by GNSS signals. Whereas, antenna gain measures the antenna's ability to focus transmitted power in the certain direction (Misra and Enge 2006). Stability and repeatability of the phase centre in a geodetic-grade antenna with respect to variations in elevation and azimuth angle of the received signal are important factors in achieving high accuracy.

Table 2.3 compares the three antennas from which data are collected, in terms of price range, gain pattern, polarization and axial ratio. It can be observed from Table 2.3, the geodetic-grade antenna has the highest gain of 6.8 dB. Whereas ultra-low-cost (cellphone) has the lowest and irregular gain of 3-4.3 dB. Antenna gain is proportional to the size of the antenna, which explains the irregular and low gain values of cell-phone antenna. The cellphone grade antenna loses between 5 and 15 dB in sensitivity as compared to the survey-grade antenna. Such a loss makes it difficult to retain a lock on GNSS signals (Pesyna et al. 2014). The cellphone antenna's linear polarization also makes it susceptible to multipath effects (Banville and Van Diggelen 2016).

As explained above, geodetic-grade and low-cost antennas are RHCP, which is an optimum polarization for the reception of GNSS signals in a "clean" environment. A linearly polarized antenna with nearly omnidirectional pattern can receive both LHCP and RHCP signals, which makes the obtained measurements prone to multipath. On the other hand, such an antenna increases the satellite availability, since its radiation pattern can uniformly cover the entire azimuth plane down to low elevation angles, however, with degraded carrier-to-noise (C/N_0) values (Rao 2013). C/N_0 is the ratio of the carrier power and the noise power per unit bandwidth, which is used to determine the signal strength of tracked satellites.

Hardware	Price ($)	Gain (dB)	Polarization	Axial ratio
Geodetic grade	few 1000s	6.8	RHCP	1 dB
Low-cost (patch antenna)	few 100s	4.3	RHCP	3 dB
Ultra-low-cost	few 10s	3-4.3	Linear	10+ dB

Table 2.3: Specifications of geodetic-grade, low-cost and ultra-low-cost antenna

Chapter 3 Optimal single-frequency estimation process

In the early 2000s, single-frequency PPP started to gain some traction. Single-frequency PPP is not accurate in comparison with dual-frequency PPP, because of the multipath and the un-modelled ionospheric delay. As single-frequency PPP is transitioning into a wider range of applications, e.g., with low-cost and ultra-low-cost GNSS hardware, it poses new challenges in terms of dealing with lower quality of raw observations, relative observation weights in the adjustment, and increased multipath.

3.1 Observable parameterization

Traditional dual-frequency PPP is based on forming ionosphere-free linear combinations of the code and carrier-phase measurements. Also, dual-frequency observation can be processed in an un-combined manner where the slant ionospheric delay to each satellite is estimated in state. As this research is focused on the single-frequency processing, models only concerned with single-frequency are presented.

Single-frequency PPP code and carrier-phase observation equations can be written as (Kouba 2009):

$$l_{C/A} = \rho + c(dT - dt + T_{GD}) + d_{trop} + d_{iono} + \varepsilon_{C/A} \tag{3.1}$$

$$l_{\phi} = \rho + c(dT - dt) + d_{trop} - d_{iono} + N\lambda + \varepsilon_{\phi} \tag{3.2}$$

where:

$l_{C/A}$ is the measured C/A-code pseudorange,

l_{ϕ} is the measured carrier-phase range,

ρ is the geometric range,

c is the speed of light in the vacuum,

dT is the station receiver clock offset from the GPS time,

dt is the satellite clock offset from the GPS time.

d_{iono} is the ionospheric delay,

d_{trop} is the tropospheric delay,

N is the non-integer ambiguity term,

λ is the wavelength on L1,

T_{GD} / DCB is the group delay differential; also known as Differential Code Biases

$\varepsilon_{C/A}, \varepsilon_{\phi}$ are the respective noise components including multipath.

For the sake of simplicity, all error sources in PPP processing are not discussed here. However, for the full treatment of error sources in PPP, the reader can refer to, e.g., (Kouba 2009; Seepersad 2012; Aggrey 2015).

3.2 Functional models

Single-frequency PPP can be classified into code-only processing and combined code and carrier-phase processing. Code-only processing is simpler as there are no ambiguous carrier-phase measurements to deal with. Brief description of both processing methods is provided.

3.2.1 Code-only processing

Single-frequency PPP started as code-only positioning, where carrier-phase measurements are not used in the estimation process. Observation model for code-only PPP is the same as Equation 3.1. An earlier version of CSRS-PPP online service only processes single-frequency code measurements and better than a metre-level accuracy was demonstrated in ideal circumstances, when precise orbit and clock corrections are used.

3.2.2 Combined code and carrier-phase (GRAPHIC)

Carrier-phase and code measurements can be used in both uncombined and combined manner. Uncombined model is previously listed in Equations 3.1 and 3.2. Single-frequency PPP with geodetic-grade hardware could also take advantage of more precise carrier-phase observations along with the code observations to mitigate the ionospheric delay. Single-frequency code and carrier phase combination is commonly known as GRAPHIC (Yunck 1993). This combination takes advantage of the fact that the ionosphere affects the code and the carrier-phase observations with an equal magnitude and but in the opposite direction.

The processing method used in this study (to process geodetic data) is based on the method purposed by Yunck (1993):

$$\phi_{GRAPHIC} = \frac{C/A_{code} + \phi_1}{2} \tag{3.3}$$

The newly formed phase-observable is used as a phase observation in the filter. This combination has its limitations, as noisy C/A-code measurements from low-cost GNSS hardware makes $\phi_{GRAPHIC}$ observable noisy as well. This combination propogates the C/A-code noise to the new phase observable. Because of the antenna and the internal hardware of low-cost and the ultra-low-cost GNSS hardware, observations are noiser and are more susceptible to multipath compared to the measurements from the geodetic-grade of GNSS receivers.

3.2.3 Estimating slant ionospheric delay using uncombined measurements

For geodetic-grade hardware slant ionospheric delays are also estimated using GIM as pseudo-observations in the uncombined filter. This method can be thought as the state augmentation model, and the complete functional model is given as:

$$
\begin{aligned}
l_{C/A} &= \rho + c(dT - dt + T_{GD}) + d_{trop} + d_{iono} + \varepsilon_{C/A} \\
l_{\phi} &= \rho + c(dT - dt) + d_{trop} - d_{iono} + N\lambda + \varepsilon_{\phi} \\
l_{GIM} &= d_{iono}
\end{aligned}
\tag{3.4}
$$

Slant ionospheric delay estimates using GIM observations as constraints, offers better representation of true ionosphere compared to the using corrections from GIM. External ionosphere information from GIMs can potentially help with improving the accuracy and convergence time of the positioning solution.

However, this approach is only limited to the geodetic-grade equipment as the measurement noise and multipath on geodetic measurements is much lower compared to the low-cost and ultra-low-cost hardware. On the other hand, measurements from low-cost equipment are too noisy and more prone to multipath effects. Multipath and noise contamination from the C/A-code measurements does not allow Kalman filter to produce reliable slant ionospheric delay estimates.

3.3 Single-frequency PPP GNSS filter

The well-known position-velocity model is used in this study. Based on the adopted model, the system state vector is given as:

$$X = \begin{bmatrix} X \\ X_{vel} \\ Y \\ Y_{vel} \\ Z \\ Z_{vel} \\ dt \\ zpd \\ N^1 \\ \vdots \\ N^n \end{bmatrix} \tag{3.5}$$

The design matrix *H* is given in Equation 3.6. Each row contains the partial derivatives of each observation with respect to the unknown parameters, which are user position (X, Y, Z), receiver clock offset (dt), zenith path delay (zpd) and the carrier-phase ambiguities (N^i)

$$H = \begin{bmatrix} \frac{dR^1}{dX_i} & 0 & \frac{dR^1}{dY_i} & 0 & \frac{dR^1}{dZ_i} & 0 & \frac{dR^1}{dt_i} & \frac{dR^1}{dZPD_i} & 0 & 0 & ... & 0 \\ \frac{d\phi^1}{dX_i} & 0 & \frac{d\phi^1}{dY_i} & 0 & \frac{d\phi^1}{dZ_i} & 0 & \frac{d\phi^1}{dt_i} & \frac{d\phi^1}{dZPD_i} & \frac{d\phi^1}{dN_{if,1}} & 0 & ... & 0 \\ \vdots & \vdots & \vdots & \vdots & \vdots & \vdots & \vdots & \vdots & 0 & 0 & ... & 0 \\ \frac{dR^n}{dX_i} & 0 & \frac{dR^n}{dY_i} & 0 & \frac{dR^n}{dZ_i} & 0 & \frac{dR^n}{dt_i} & \frac{dR^n}{dZPD_i} & 0 & 0 & ... & 0 \\ \frac{d\phi^n}{dX_i} & 0 & \frac{d\phi^n}{dY_i} & 0 & \frac{d\phi^n}{dZ_i} & 0 & \frac{d\phi^n}{dt_i} & \frac{d\phi^n}{dZPD_i} & 0 & 0 & ... & \frac{d\phi^n}{dN_{if,n}} \end{bmatrix} \tag{3.6}$$

C represents the measurement and process noise matrix, which is given:

$$C = \begin{bmatrix} \sigma_{C/A}^2 & & & & & \\ & \sigma_{\Phi}^2 & & & & \\ & & \ddots & & & \\ & & & \sigma_{C/A}^2 & & \\ & & & & \sigma_{\Phi}^2 \end{bmatrix} \tag{3.7}$$

$\sigma_{C/A}$ and σ_{Φ} represent the standard deviations of C/A-code and carrier-phase measurements, respectively. For each set of hardware, $\sigma_{C/A}$ and σ_{Φ} values are unique, as the noise on measurements from geodetic-grade, low-cost and ultra-low-cost hardware is different. $\sigma_{C/A}$ and σ_{Φ} values for each set of hardware are defined empirically, which are discussed in Chapter 4. σ_{Φ} value for GRAPHIC carrier-phase observations is also different than the uncombined measurements.

Position, velocity (PV) is used as a system model in the Extended Kalman filter given as:

$$X_{K+1} = \Phi_{K+1,k} X_k \tag{3.8}$$

$\Phi_{K+1,k}$ is the transition matrix, X_{K+1} is the predicted state vector at epoch (k+1), and X_k is the filter state vector estimate. $\Phi_{K+1,k}$ is an identity matrix for static datasets processing, whereas for kinematic processing $\Phi_{K+1,k}$ for the position block is given as:

$$\Phi_{k+1,k(position)} = \begin{pmatrix} 1 & \Delta t & 0 & 0 & 0 & 0 \\ 0 & 1 & 0 & 0 & 0 & 0 \\ 0 & 0 & 1 & \Delta t & 0 & 0 \\ 0 & 0 & 0 & 1 & 0 & 0 \\ 0 & 0 & 0 & 0 & 1 & \Delta t \\ 0 & 0 & 0 & 0 & 0 & 1 \end{pmatrix} \tag{3.9}$$

whereas the predicated covariance is gives as:

$$P_{k+1,k} = \Phi_{k+1,k} P_k \Phi_{k+1,k}^T + Q_k \tag{3.10}$$

Sub-block of process noise matrix, Q of position errors is given as:

$$Q_{position} = \begin{bmatrix} \frac{q\Delta t^3}{3} & \frac{q\Delta t^2}{2} & 0 & 0 & 0 & 0 \\ \frac{q\Delta t^2}{2} & q\Delta t & 0 & 0 & 0 & 0 \\ 0 & 0 & \frac{q\Delta t^3}{3} & \frac{q\Delta t^2}{2} & 0 & 0 \\ 0 & 0 & \frac{q\Delta t^2}{2} & q\Delta t & 0 & 0 \\ 0 & 0 & 0 & 0 & \frac{q\Delta t^3}{3} & \frac{q\Delta t^2}{2} \\ 0 & 0 & 0 & 0 & \frac{q\Delta t^2}{2} & q\Delta t \end{bmatrix} \tag{3.11}$$

where q is the spectral density of the velocity.

As the behaviour of the receiver clock is unpredictable, it is modelled as a white noise with a large process noise assigned to Q_{dt}. Wet zenith path delay (zpd) is modelled as a random walk process. Whereas, process noise for ambiguity terms (Q_{sat}^n) is assumed zero, since the carrier-phase ambiguities remain constant over time, as long as there is no cycle-slip.

Practically, the Kalman filter is considered as one of the great discoveries of twentieth-century mathematical engineering (Grewal and Andrews 2001). Kalman filtering is a linear recursive data processing algorithm that processes all available measurements, regardless of their precision, to estimate the current value of the variable of interest, with use of (i) knowledge of the system and measurement device dynamics, (ii) the statistical description of the system noises, measurement

errors, and uncertainty in the dynamics models, and (iii) available information about initial conditions of the variable of interest (Maybeck 1982). If the input data fits the pre-defined linear dynamics and statistical models and prior knowledge is known, the Kalman filter can provide an optimal, in a minimum variance sense, estimate of the state vector (Gelb 1974). Accordingly, the Kalman filter has become the most common technique for estimating the state of a linear system, particularly in navigation systems. Since the estimation process is implemented on a computer, the discrete form of the Kalman filter is generally used. Details of the derivation are available in Gelb (1974), or Verhagen and Teunissen (2017).

Figure 3.1 shows the architecture of the Extended Kalman filter, implemented in the York-PPP engine. Complete architecture of York-PPP single-frequency module is presented in Chapter 4. The Extended Kalman filter stochastic models including the system model are given is the previous section. The implemented filter is capable of processing measurements from all available constellations and from all available frequencies. Measurements along with the required error corrections that pass the initial screening are fed into the filter, and observation equations are formed. Based on the user defined dynamics, process model is initialized as static or kinematic, and then the final position along with other parameters are computed.

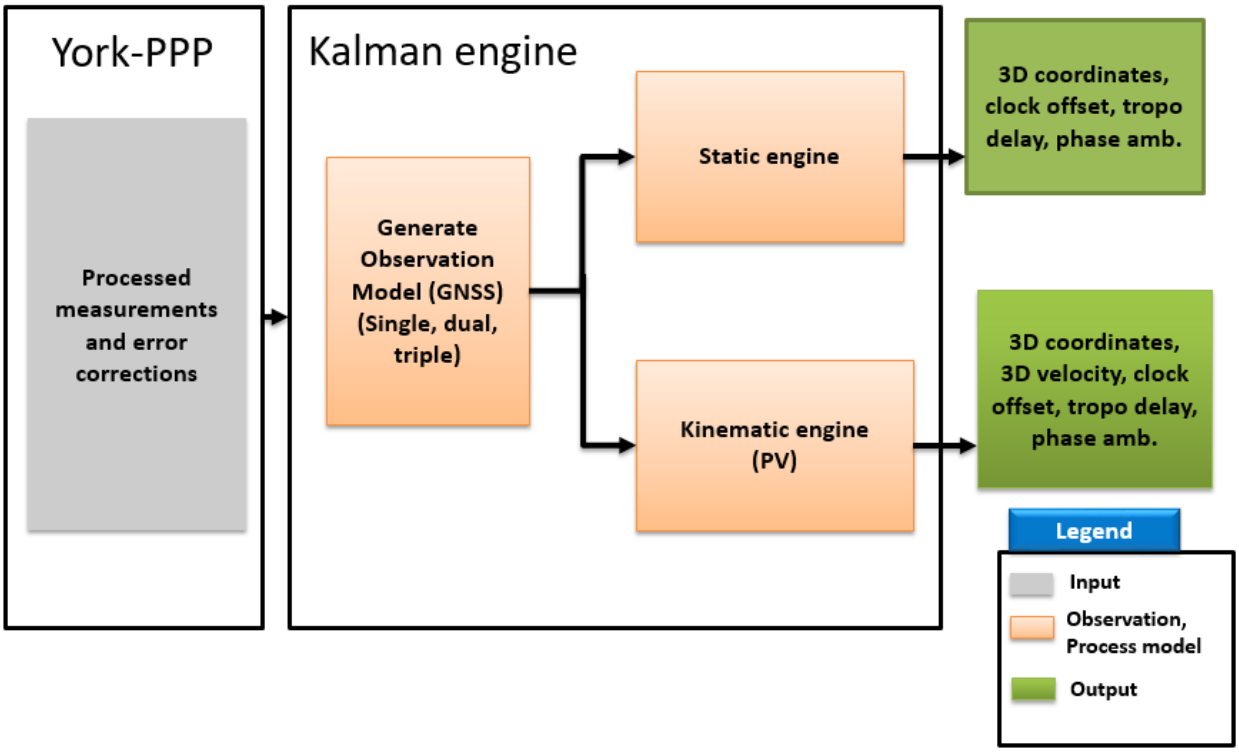

Figure 3.1:Extended Kalman filter architecture of York-PPP engine

Chapter 4 Development of York PPP single-frequency PPP engine

The York GNSS single-frequency PPP engine is a sophisticated positioning software which meets scientific standards and has been tested for various geodetic and non-geodetic research applications. The single-frequency module has been developed by the author, which is an extension of the dual- and triple-frequency PPP software developed by Seepersad et al. (2012) and Aggrey et al. (2015). To optimize the positioning solution, a Kalman filter for York-PPP was also developed during this study. This section gives an overview of the architecture of the York GNSS single-frequency module. It also briefly discusses the observation and the correction models used within this module.

Figure 4.1 illustrates the architecture of York GNSS single-frequency module. It comprises of four major segments: input, pre-processing of observations, filtering, and output. The input segment further consists of reading the raw observation data from the files. The pre-processing component ensures that the checks are in place to reject or flag observations that do not pass the quality control routines. Observations that pass the quality check are fed into the Kalman filter where position estimates along with other parameters are optimally estimated. Post-fit residuals are analyzed for outliers. For flagged residuals, corresponding observations are removed and then the solution is re-computed.

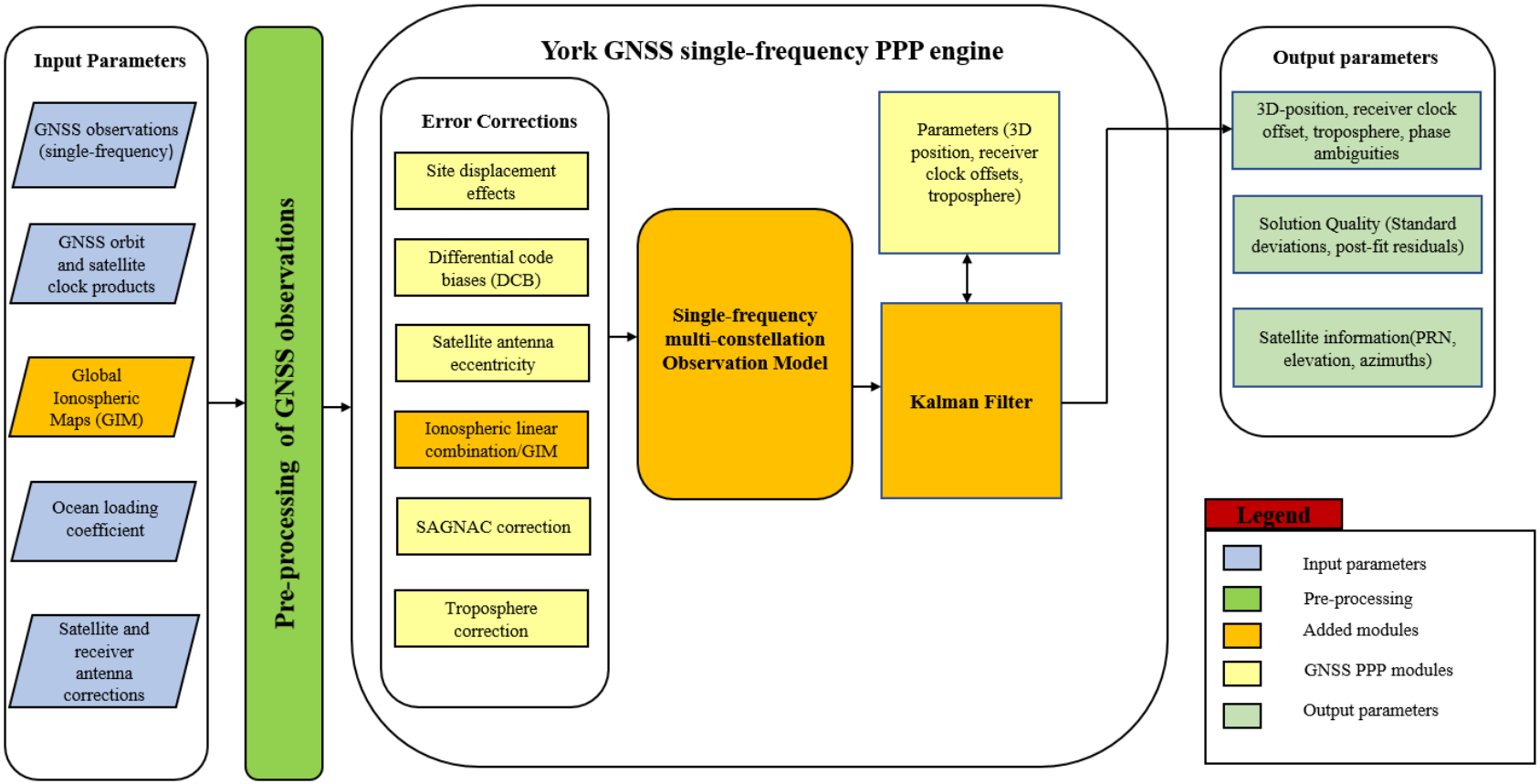

Figure 4.1: Instance of York GNSS PPP engine: single-frequency, expanded from Aggrey (2015)

4.1 York SF-PPP quality control and outlier detection

Un-differenced GNSS measurements are processed in a recursive manner that verifies the quality of the measurements and rejects any outliers. The pre-processing of the measurements is conducted individually for each satellite. First, a basic screening is conducted to detect any large outliers. Then the geometry-free linear combination is formed to detect any cycle-slips. Signal-to-noise ratio values of each satellite are checked for low-cost and ultra-low-cost GNSS receivers. If the signal-to-noise ratio is less than the empirically set threshold value, the measurements associated with the satellite is rejected for that particular epoch.

Once all the measurements passed the initial screening, the solution is computed using all the measurements which have passed initial QC. Residuals are computed and statistically analyzed for outliers. If any residual does not pass the threshold limit, the corresponding observation is then removed and the solution is again computed.

4.2 Cycle slip detection

Carrier-phase measurements are more precise than the pseudoranges. At any epoch, the carrier-phase measurement comprises the observed accumulated phase $\Delta\phi$ and the integer number of wavelengths N, also known as ambiguity term. The receiver measures and keeps track of the $\Delta\phi$, whereas N remains constant as long as there is no loss of signal (Hofmann-Wellenhof et al. 2007). In some events, a receiver loses lock and there is a sudden jump in the carrier-phase measurement which is called a cycle-slip.

Cycle slips are primarily caused by the obstruction in the satellite-receiver line of sight because of trees, buildings, etc. The other source of cycle slip is associated with low signal-to-noise ratio,

because of the difficult atmospheric conditions, multipath, low elevation angle and large acceleration changes.

In this research a carrier-phase and code-pseudorange combination is used to detect the cycle slip. Carrier-phase and code measurements are given as follows (Hofmann-Wellenhof et al. 2007):

$$l_{(C/A)/P} = \rho + c(dT - dt) + d_{trop} + d_{iono} + \varepsilon_{C/A} \tag{4.1}$$

$$l_{\phi} = \rho + c(dT - dt) + d_{trop} - d_{iono} + N\lambda + \varepsilon_{\phi} \tag{4.2}$$

and by subtracting (1) and (2)

$$l_{\phi} - l_{(C/A)/P} = -2d_{iono} + N\lambda + \varepsilon \tag{4.3}$$

By forming the carrier-phase and code-pseudorange difference, the non-dispersive delays such as clocks, geometry, troposphere, etc. are cancelled. The terms that are left in Equation (4.3) are twice the ionospheric delay, ambiguity term, $N\lambda$ and the measurement noise, ε.

The effect of ionosphere term on cycle slips can be safely ignored since the change in the ionosphere is fairly small from epoch-to-epoch. In the research, if the difference in (4.3) is larger than the threshold value – implies that the cycle-slip has occurred and then ambiguity term is reinitialized. The threshold values for geodetic grade hardware is obtained from Seepersad (2012), and for low-cost and ultra-low-cost hardware, thresholds are defined empirically.

4.3 Ionospheric error mitigation models

GNSS signals are affected by the medium through which they travel from a satellite to a receiver. Signal travel distance ranges from 20,000 km to 26,000 km depending on if the satellite is rising/setting or overhead. The 95% of the signal travel can be regarded as in the vacuum or free

space, through which electromagnetic signals travel with a constant speed $c = 299,792,458$ m/s, the well-known universal constant (Misra and Enge 2006).

GNSS signals enters the ionosphere at a height of about 1000 km. The ionosphere region extends from a height of 50 km to 1000 km above the Earth's surface. In this region the density of free electrons and ions are high enough to influence the propagation of satellite signals (Choy 2009). The density of free electrons and ions depends on the intensity of the solar radiation, Earth's magnetic field as well as the geographic location (Choy 2009). As the Sun rises, its ultra-violet radiation separates gas molecules into ions and free electrons, with a peak at around 2 pm local time (Misra and Enge 2006). The presence of free electrons influences the wave propagation the most and can cause an error in GNSS positioning ranging from few metres to tens of metres depending on the user's location and time variations in the ionosphere.

Dual-frequency GNSS receivers can make use of the dual-frequency ionosphere-free linear combination to mitigate ionospheric refraction. In single-frequency GNSS receivers, external model(s) or ionospheric products are required to compensate for the ionospheric error. The section below lists and explains the available models and products that could be used to mitigate the ionospheric delay.

4.3.1 Klobuchar model

The Klobuchar Model was developed approximately three decades ago to mitigate the ionospheric delay for single-frequency users by John A. Klobuchar. It is based on using eight coefficients, transmitted as part of the satellite navigation message, to provide correction for approximately 50% rms of the ionospheric range error (Klobuchar 1987). The satellite navigation message is truncated version of the much larger empirical model of total electron content (TEC) developed

by Bent over four decades ago (Choy 2009). State-of-the-art ionospheric method require as many coefficients to mitigate 70% to 80% of the delay. The ionospheric delay is proportional to the TEC encountered by the EM waves during the signal transit time. Daily TEC values are dependent on many factors such as user location, time of the day, solar flux, etc. This algorithm was based on giving the best fit to the large daytime values of monthly average TEC, and to accept any difference from monthly average TEC behaviour as part of the residual error for a GPS system user (Klobuchar, 1987). This method assumes the correlation distance and correlation time of TEC deviations from monthly average conditions are small. So, the resolution of this method did not capture the short-term changes in the ionosphere. The broadcast model is based on the single-layer model or "thin shell model" of the ionosphere. This model assumes that the TEC has concentrated at an infinitesimally thin spherical layer at a mean ionospheric height of 350 km.

4.3.2 Linear combinations

The primary reason for the availability of the second frequency in GNSSs receivers is to remove the ionospheric delay via combination. Code and carrier-phase observations from dual-frequency receivers can be linearly combined to mitigate the ionospheric delay (Leick 1995), e.g., for GPS L1 and L2:

$$P_{IF} = \frac{f_1^2 P_1 - f_2^2 P_2}{f_1^2 - f_2^2}$$
$$L_{IF} = \frac{f_1^2 (L_1\lambda_1) - f_2^2 (L_2\lambda_2)}{f_1^2 - f_2^2} \quad (4.4)$$

where f_1 = 1775.42 MHz and f_2 = 1227.60 MHz which are the frequencies of the L1 and L2 signals, respectively, and λ_1 = 19 cm and λ_2 = 24.4 cm are the wavelength of the L1 and L2 signals, respectively. The above combination can be used only if the measurements from both frequencies are available.

There is a model available for single-frequency receivers as well, to remove the ionospheric delay known as GRoup And PHase Ionospheric Correction (GRAPHIC). It makes use of the property that ionosphere delays the code ranges, but advances the carrier-phase by the same magnitude (Montenbruck 2003; Bock et al. 2009; Muellerschoen et al. 2004). So, by forming a linear combination of P1 and L1 measurements, ionospheric error is mitigated. The carrier-phase combination $\phi_{GRAPHIC}$ shown in Equation 3.3, can mitigate the first-order ionosphere error.

4.3.3 Global Ionospheric Maps (GIM)

In this research, the ionospheric delay d_{iono} is mitigated by using the Global Ionospheric Maps (GIM) provided by IGS and other organizations, which are in IONsphere map EXchange (IONEX) format (Schaer et al. 1998). It is also the most accurate empirical model available for absolute-positioning using the single-frequency GPS receiver (Øvstedal 2002).

Daily TEC values are available in the IONEX format ranges from $+87.5^{\circ}$ to -87.5° in latitude, with a spatial resolution of 2.5°. In longitude grid points are arranged from -180° to $+180^{\circ}$ with a resolution of 5°. Total of 13 TEC maps are available each day with a temporal resolution of 2 hours (Wienia 2008). GIM model has an accuracy of 2 – 8 TECU (total electron content unit). An accuracy of 2 TECU (1 TECU corresponds to 0.163 m range error in $l_{C/A}$) at grid points can be achieved using GIM (Chen and Gao 2005; Øvstedal 2002).

Other important conventions of the IONEX format are (Schaer et al. 1998; Wienia 2008):

- TEC maps are given in an Earth-fixed reference frame
- TEC rms values are also included.
- TEC maps are given in Universal Time (UT) and are epoch specific.

- TEC maps are given in spherical coordinates.
- The option of 3-dimensional TEC maps is also included into IONEX

Global Ionospheric Maps can be thought as an instance of global ionospheric TEC distribution at a specific interval. Figure 4.2 shows the 2-dimensional global GIM on April 4, 2004, at 12:00 am.

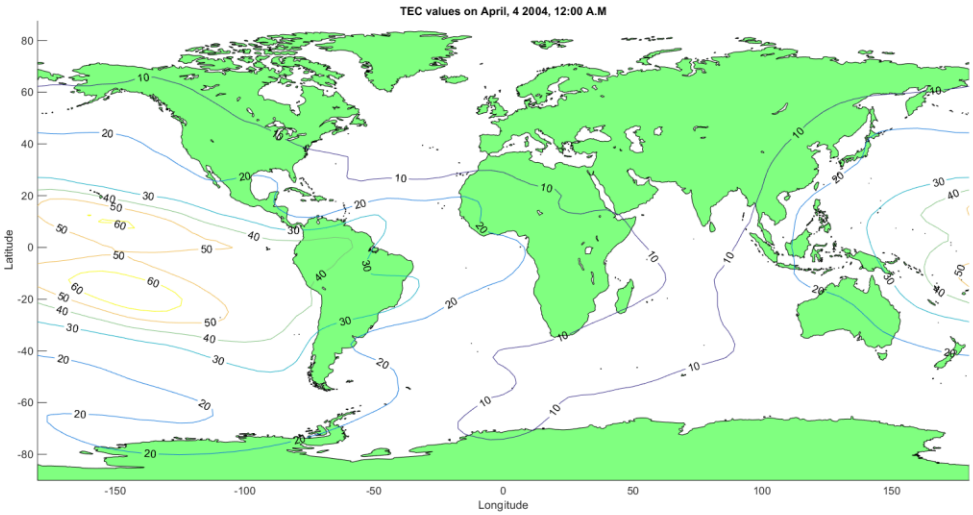

Figure 4.2: Snapshot of TEC values on April 4, 2004, at 12:00 AM

These are also single-layer models which assume that the TEC is concentrated in an infinitesimally thin shell at a certain height (*H*) from the surface of the Earth. The height of the single layer model ranges from approximately 350 km to 450 km, corresponding to the height of the maximum electron density usually adopted for the ionosphere (Schaer et al. 1998). The IGS GIMs assumes a fixed altitude of 450 km for the single-layer model.

Since the satellites are observed in the slant direction, the sub-ionospheric point must be calculated first. The point of interest for which a TEC value is to be estimated is not the location of the receiver, but the location of the sub-ionospheric point as shown in Figure 4.3. The intersection of

the shell and the satellite-receiver line of sight at a given local time is defined as the Ionospheric Pierce point (IPPs). The geocentric spherical coordinates (ϕ, λ) of the sub-ionospheric point can be computed from the known receiver coordinates as:

$$\sin z' = \frac{R}{(R+H)} \sin z \tag{4.5}$$

$$\phi = \sin^{-1}(\sin\phi_r \cos(\Delta z) + \cos\phi_r + \cos\phi_r \sin(\Delta z)\cos\alpha) \tag{4.6}$$

$$\lambda = \lambda_r + \sin^{-1}\left(\frac{\sin(\Delta z)\sin\alpha}{\sin\phi}\right) \tag{4.7}$$

where:

Δz spherical distance at the height of the receiver and IPP

ϕ_r receiver latitude

λ_r receiver longitude

α, z azimuth and the zenith of the receiver, respectively

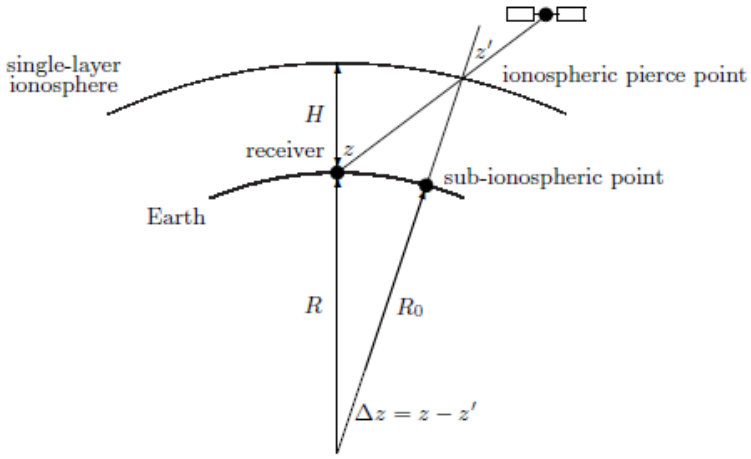

Figure 4.3: Single-layer model (Wienia 2008)

Figure 4.4 represents the location of the sub-ionospheric points with respect to the location of the receiver at station ALGO. Arcs in Figure 4.4 represents the sub-ionospheric points with respect to the receiver location.

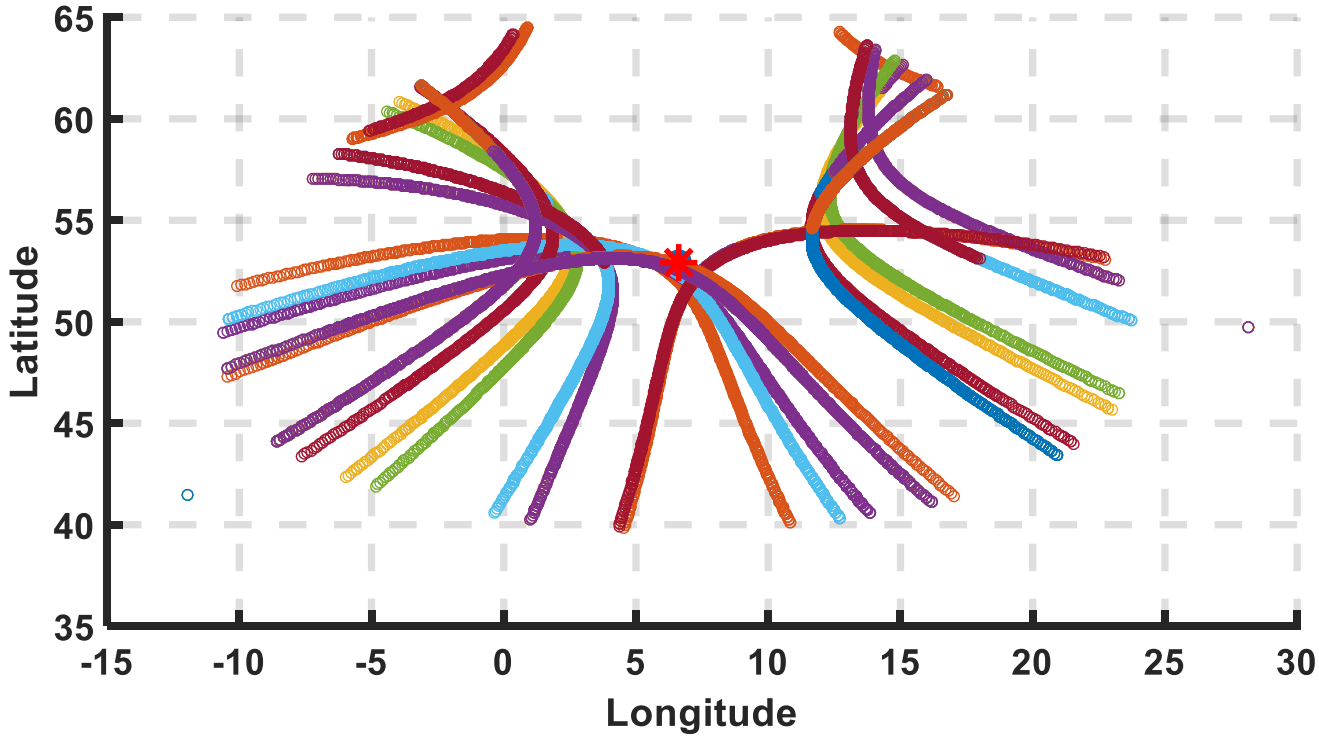

Figure 4.4: Sub-ionospheric points with respect to the user location. Different colours represent satellites

TEC values are interpolated both in space and time to obtain the appropriate TEC value at user location and time. For interpolation in space, a simple 4-point bilinear interpolation is used which is also recommended (Schaer 1998). For interpolation in time, a linear interpolation between two consecutive TEC maps is also recommended by Schaer (1998). The VTEC at the sub-ionospheric point (ϕ, λ) and at a universal time *t* can computed as:

$$TEC(\phi,\lambda,t) = \frac{T_{i+1}-t}{T_{i+1}-T_i} TEC(\phi,\lambda,T_i) + \frac{t-T_i}{T_{i+1}-T_i} TEC(\phi,\lambda,T_{i+1}) \quad (4.8)$$

$$\text{where } T_i \leq t \leq T_{i+1}$$

Because of the strong correlation with the Sun's position (sun-hour angle), this method can be extended with co-rotated TEC maps, in which TEC maps are rotated along the z-axis. In the rotated

TEC maps the coordinate system is co-rotating with the Sun using the sun-hour angle instead of the longitude (Wienia 2008). The rotated longitude λ^{rot} is given by:

$$\lambda_i^{rot} = \lambda + (t - T_i), \lambda_i^{rot} = \lambda + (t - T_{i+1}) \quad . \tag{4.9}$$

Figure 4.5 shows the actual TEC values and the interpolated TEC using different methods, for 24 hours at station ALGO. To investigate, if the higher interpolation methods describe the ionosphere state more accurately, linear interpolations methods (including rotated versions) are compared to the nearest neighbour methods. In Figure 4.5 the nearest methods show a discrete behaviour which is not in agreement with the continuous TEC values.

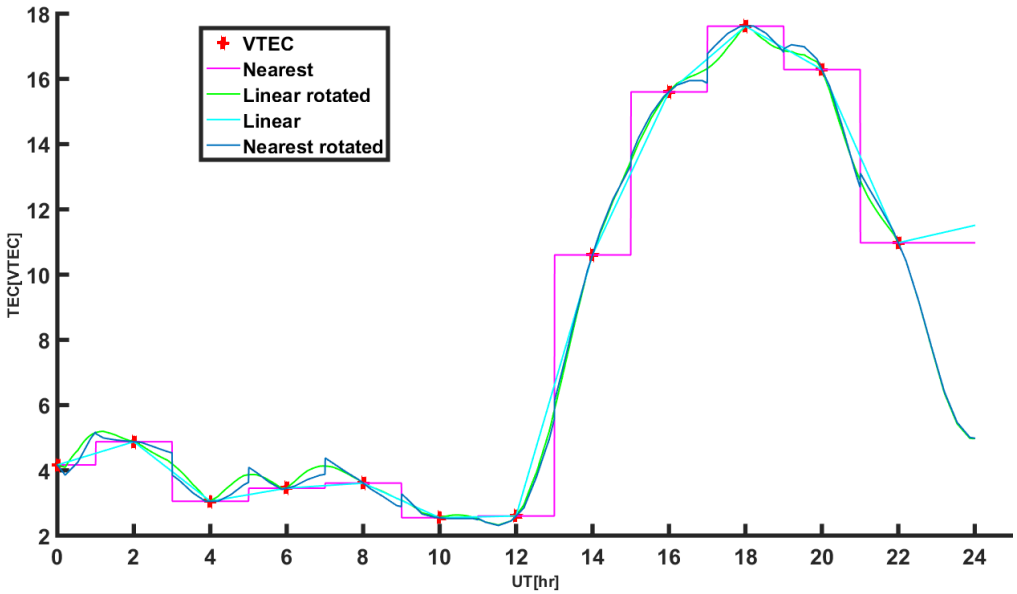

Figure 4.5: VTEC values using different interpolation methods

TEC values are provided along the ray path (i.e. slant TEC). Since VTEC is of the main interest, an elevation dependent mapping function F(z) is defined, which described the ratio between the slant TEC and the VTEC required.

$$slantTEC = F(z)VTEC \tag{4.10}$$

$$F(z) = \frac{1}{\sqrt{1 - \sin^2 z'}} \tag{4.11}$$

Figure 4.5 also suggests that the linear interpolation and linear rotated interpolation results are smooth compared to the nearest interpolation and the nearest rotated interpolation. So, in this study, linear interpolation methods are employed. The behaviour of linear, and linear rotated interpolation methods is found to be similar at station ALGO, but Wienia (2008) suggested that it could be beneficial to apply rotated interpolation in the equatorial region. Second or third order interpolation methods could be explored, but in this research only the linear and the nearest neighbour methods are compared.

Chapter 5 Results and analysis

The previous chapters have provided a background of single-frequency PPP, the estimation model used and outlined the design and architecture of the developed software. This chapter presents the results and analysis of the single-frequency PPP solutions with geodetic, low-cost and ultra-low-cost GNSS receivers. Quality of raw measurements from three grades of GNSS hardware is also investigated by analyzing the C/N_0 values, code-phase linear combination, and post-fit measurements residuals. Raw observations are processed using both combined and uncombined single-frequency PPP filter, and the pros and cons of each filter are discussed. The benefit of using combined GPS and GLONASS measurements in processing are compared to the GPS-only processing from low-cost and ultra-low-cost devices. The chapter concludes with the comparison of positioning solutions from three different grades of GNSS receivers.

5.1 Experimental procedures and datasets

1.5 hours of static data were collected on the roof of the Petrie Science and Engineering building, York University. Figure 5.1 shows the view of three different grades of hardware used in data collection. The data collection was done simultaneously to ensure that analysis can be made under similar environmental conditions, i.e., atmosphere refraction, and multipath.

Figure 5.1: View of data collection at the roof of Petrie Science and Engineering Bldg., York University, Toronto

5.2 Raw measurement quality analysis

Figure 5.2 shows the difference between the C/A-code and the carrier-phase measurements, which represents the multipath, signal noise assuming that ionospheric error is negligible compared to the magnitude of C/A-code multipath and the noise. As stated previously data collection is done simultaneously from three sets of hardware. Figure 5.2 shows the code multipath and code noise on satellite (PRN 24) for approximately 1.5 hrs. For demonstration, only PRN 24 was used, as it was tracked by all three receivers and available for the most duration of data collection. PRN 24 was also tracked at a high elevation angle and hence the signal has suffered less atmospheric refraction. The mean of difference of C/A-code and L1 measurements is also removed.

a)

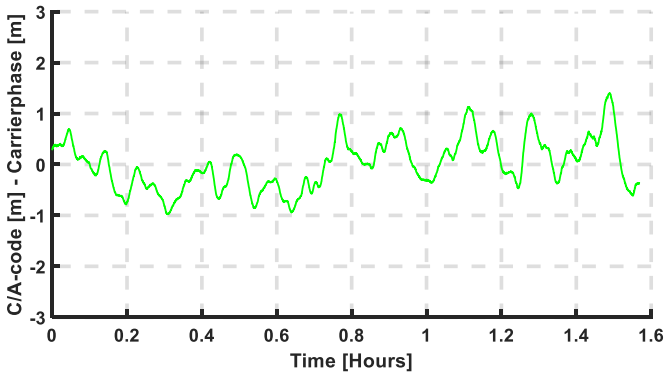

b)

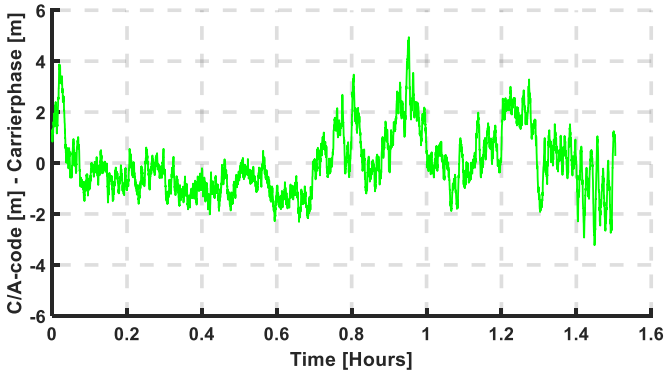

c)

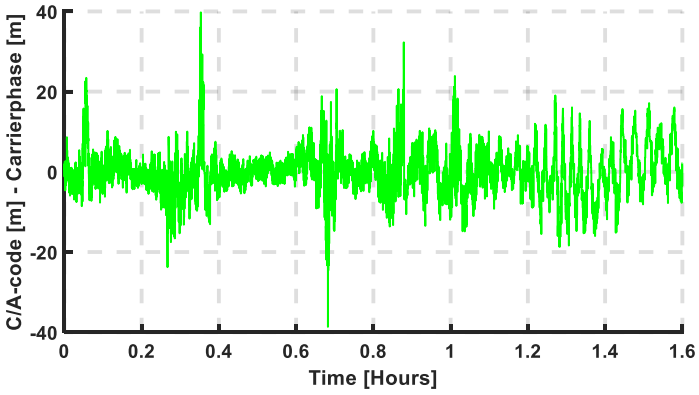

Figure 5.2: Difference in C/A-code range and carrier-phase for PRN 24 a) geodetic b) low-cost c) ultra-low-cost

The magnitude of the multipath from geodetic grade to ultra-low-cost hardware changes drastically. As the data were collected under a clear sky and same environmental conditions, the differential in magnitude is primilarly because of the poor quality of the antenna in the Nexus 9 tablet compared to the high-performance antenna with geodetic-grade.

5.3 Carrier-to-noise ratio analysis

One of the factors determining the ranging performance of GNSS receivers is carrier-to-noise ratio, C/N_0, and the averaging time used by the receiver C/N_0 is the ratio of the power in the received signal to the power spectral density of the competing noise (Misra and Enge 2006). When a GNSS signal is received at the GNSS antenna, the received power depends mainly on three factors: (1) power density of the incoming GNSS signal; (2) effective area of the antenna; and (3) gain (Misra and Enge 2006). C/N_0 values are typically low at lower elevation angles to those at zenith. The primary reason for the low C/N_0 values is the weak signal at lower elevation angles, as signal travel through excess atmospheric refraction at low elevation angles which potentially causes lower antenna gain.

Figure 5.3 illustrates the low and irregular C/N_0 values of a signal from the cellphone grade hardware (green curve) at different elevation angles, compared to that from geodetic-grade (red curve), which points to one of the major downside of cellphone antenna, known as low gain. Whereas, the blue curve suggests that C/N_0 values from low-cost hardware are low compared to geodetic-grade antenna, but not as weak or noisy as signals from the cellphone hardware.

From Figure 5.3 and Table 5.1, it can be observed that C/N_0 values for geodetic grade hardware are on average 3.5 dB-Hz higher than low-cost and 7.5 dB-Hz higher as compared to ultra-low-

cost hardware. Table 5.1 lists the average dB-Hz values of three antennas over all elevation angles. Line in red (geodetic-grade), blue (u-blox), green (Nexus 9) represents the mean C/N_0 values at elevation intervals of 1°. Variation in the green curve may also represents the multipath and the irregular gain pattern of the smartphone antenna compared to the geodetic-grade and the patch antenna, which is a crucial indicator of the low-quality observation from cellphones.

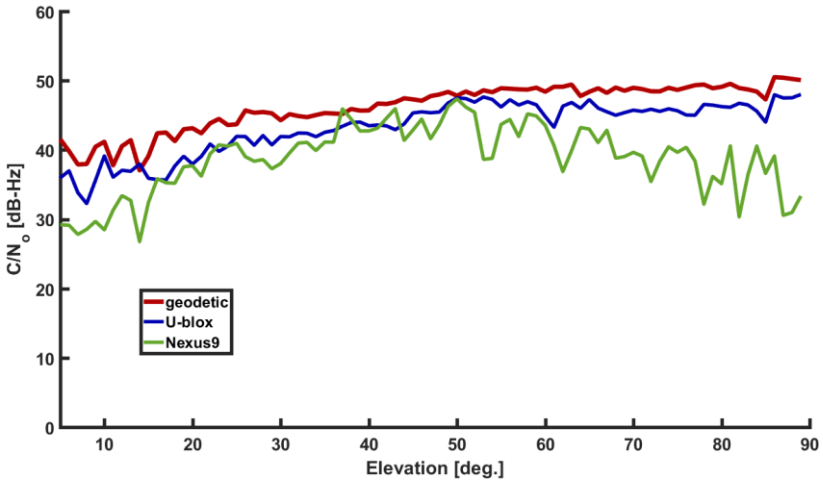

Figure 5.3: Carrier-to-noise ratio at different elevation angles from geodetic-grade and low-cost GNSS hardware

Receiver Type	$\boldsymbol{C/N_0}$
NovAtel FlexPak6	46.2 dB-Hz
u-blox	42.7 dB-Hz
Nexus 9	38.7 dB-Hz

Table 5.1:Average [dB-Hz] values overall elevation angles from geodetic-grade, u-blox, Nexus 9

Measurement noise $\sigma^2_{C/A}$ and σ^2_{L1} of the C/A-code range and carrier-phase measurements, respectively at zenith are directly proportional to the square of the pseudorange chip length, $\lambda_{C/A}$ or carrier wavelength λ_{L1}, and inversely proportional to the carrier-to-noise density ratio

C/N_0 (Braasch and Van Dierendonck 1999; Bona and Tiberius 2000; de Bakker and Tiberius 2017). Therefore:

$$\sigma_{C/A}^2 \sim \frac{\lambda_{C/A}^2}{c/n_0}; \sigma_{L1}^2 \sim \frac{\lambda_{L1}^2}{c/n_0} \tag{5.1}$$

5.4 Weighting scheme

In-order to perform uncombined single-frequency PPP, a different set of standard deviations are employed for each set of hardware. The values in the Table 5.2 are derived empirically for each set of GNSS hardware. The standard deviations are used to determine the relative weighting between the code and carrier-phase measurements. It is also important to note that with low-cost hardware, the noise on the code measurements increases, whereas the quality of the carrier-phase measurements is comparable to the geodetic-grade measurements. As demonstrated in the previous section, the magnitude of the noise on the code measurements from Nexus 9 is much higher compared to the low-cost and the geodetic measurements. This difference is the primary reason for assuming higher standard deviation for measurements from Nexus 9. The higher standard deviation can also be thought in-terms of de-weighting the noisier code measurements in the estimation process, as the a priori standard deviation determines the relative weighting.

Hardware	$\sigma_{C/A}$ [m]	σ_L [mm]
Geodetic	0.4	2
Low-cost	1.0	2
Ultra-low-cost	5	8

Table 5.2: a priori sigma for each GNSS hardware

5.5 Positioning performance analysis

To assess the positioning performance, measurements from all three grades of GNSS hardware are processed using combined and uncombined form. For each set of hardware, results are compared from both processing modes and the best positioning mode for each hardware is purposed.

5.5.1 Uncombined measurements vs. GRAPHIC

Geodetic

For the geodetic single-frequency analysis, two datasets were processed (1) week long raw data from station ALGO obtained on October 1^{st,} 2017 – October 7^{th,} 2017, (2) single-frequency data on July 21^{st,} 2017 from six Canadian IGS stations. Figure 5.4 shows the distribution of the stations, which were selected to analyze the positioning performance over the Canadian land mass.

Figure 5.4: Distribution of Canadian IGS stations used in the analysis

Figure 5.5 and 5.6 shows the horizontal positioning error at station ALGO using L1 and C/A-code – using GRAPHIC and un-combined observations, respectively. In uncombined observations,

ionospheric delay on both code and carrier-phase ranges are corrected using GIM. As shown in Figure 5.5 and 5.6, GRAPHIC performance is much superior compared to the observations processed in an uncombined manner. The solution from GRAPHIC is also much stable after the convergence compared to the converged uncombined solution as demonstrated in Figures 5.5-5.8. Table 5.3 lists the positioning accuracy obtained using GRAPHIC and uncombined processing. An accuracy of 2.7 cm, 8.2 cm, and 8.1 cm in the Northing, Easting and Up component, respectively is achieved using GRAPHIC. Whereas accuracy of 14.1 cm, 22.1 cm, and 24.5 cm is achieved when raw data are processed in uncombined form.

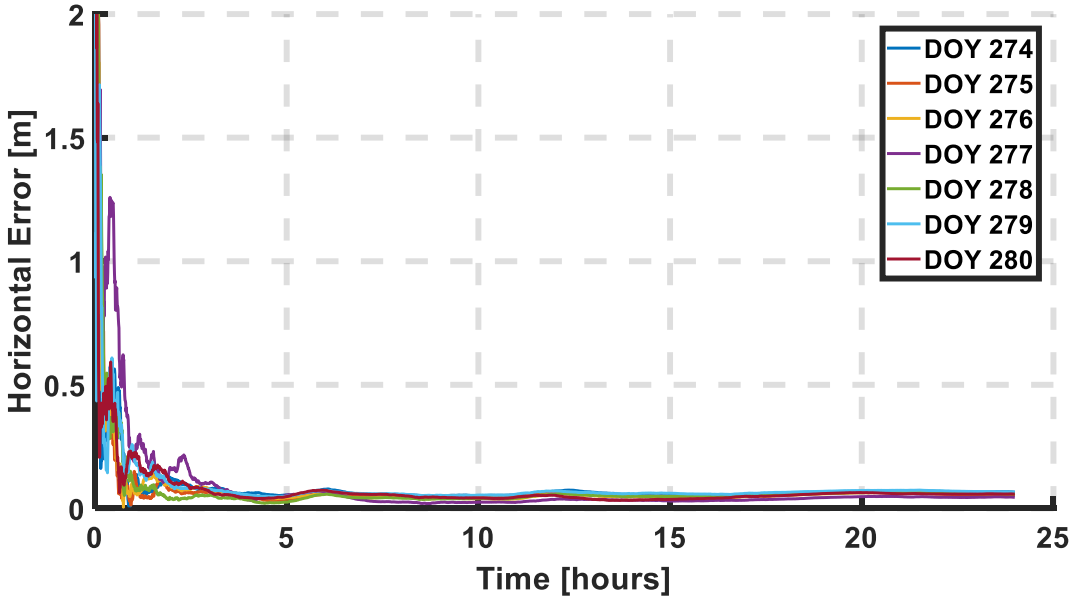

Figure 5.5: Horizontal positioning error from days October 1st, 2017- October 7th, 2017 at station ALGO using GRAPHIC

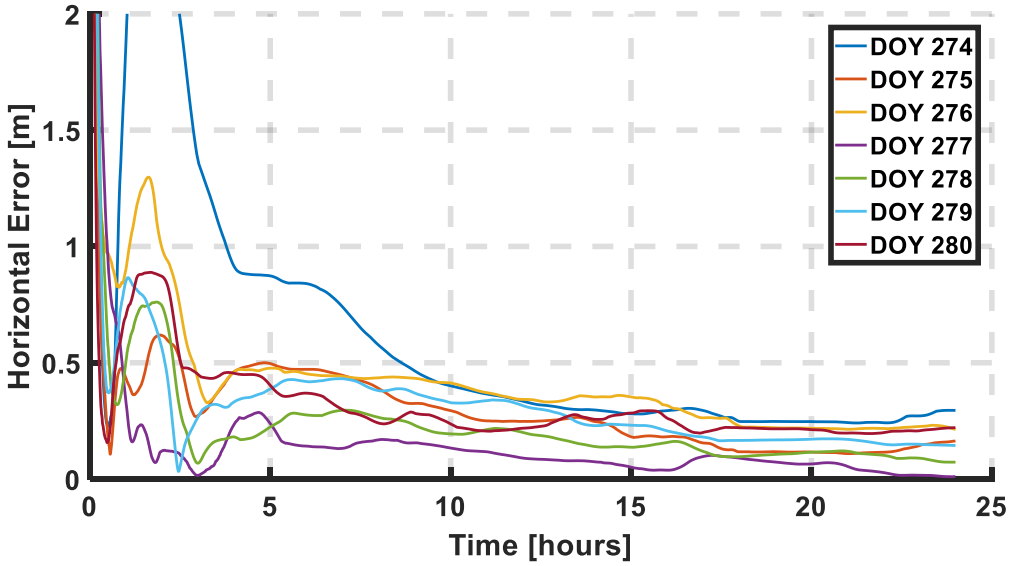

Figure 5.6: Horizontal positioning error from days October 1st, 2017- October 7th, 2017 at station ALGO using uncombined observations

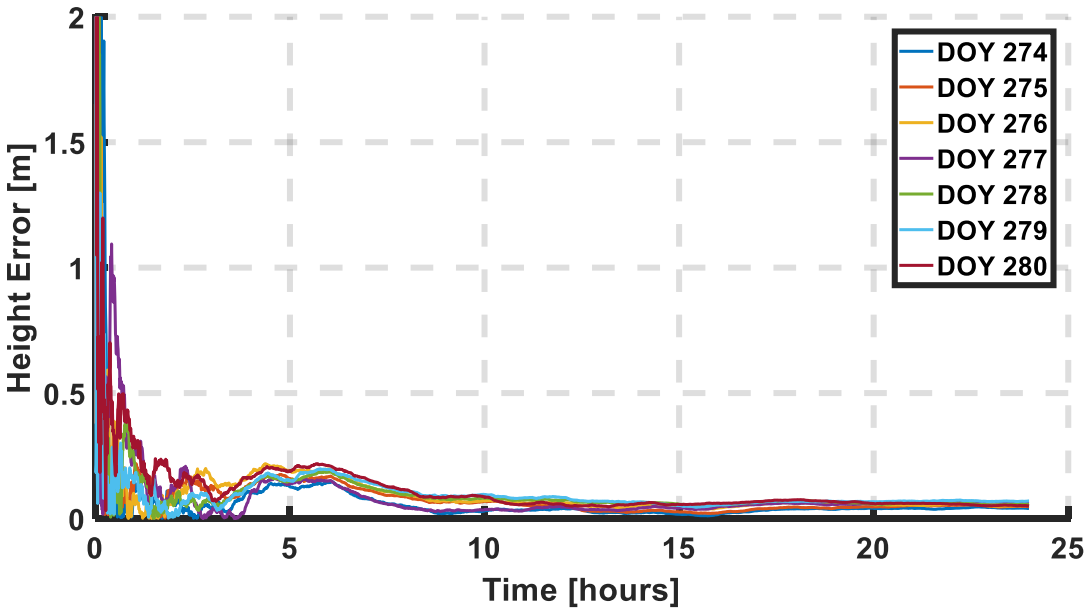

Figure 5.7: Error in height from days October 1st, 2017- October 7th, 2017 at station ALGO using GRAPHIC

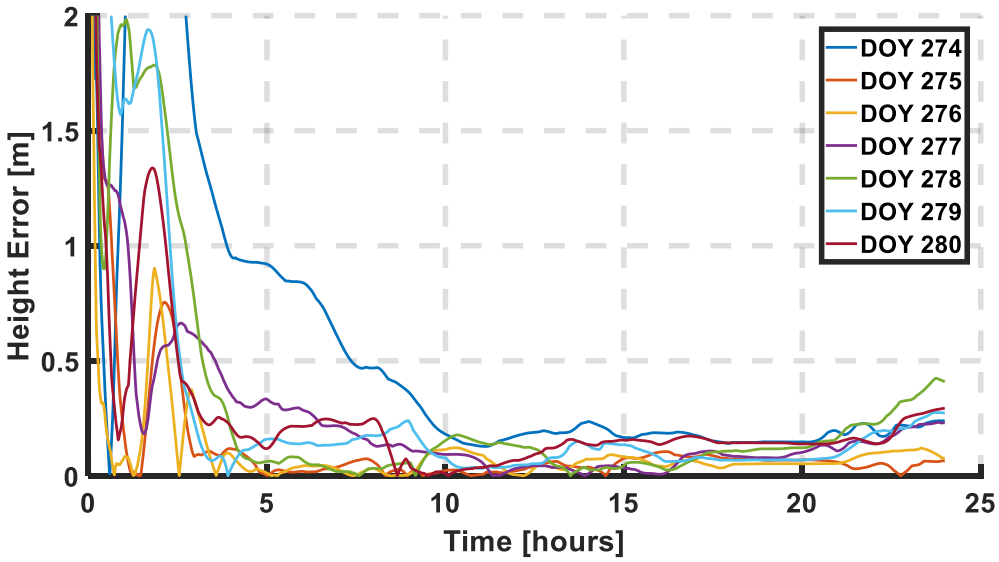

Figure 5.8: Error in height from days October 1st, 2017- October 7th, 2017 at station ALGO using uncombined observations:

:

RMS	Uncombined [cm]	GRAPHIC [cm]
Northing	14.1	2.7
Easting	22.1	8.2
Up	24.5	8.1
2D	26.2	8.6
3D	35.9	11.8

Table 5.3: Final accuracies of geodetic data processing using uncombined and combined filter

Different Stations

The L1 and C/A-code observations were used from multiple stations for analysis. Stations were selected uniformly over the Canadian land mass to assess the single-frequency PPP performance using GIM, GRAPHIC and slant ionosphere delay estimates. As expected GRAPHIC and slant delay estimation, performance is superior to the GIM performance. The primary reason is that GIM can only correct for the ionospheric delay up to 80 percent, and the uncorrected ionospheric bias is appearing in the uncombined SF-PPP solution as presented in Figure 5.10 as compared to the

GRAPHIC solution in Figure 5.9 (Sterle et al. 2015 ; Pan et al. 2017). Figure 5.11 shows the horizontal positioning error using filter estimates of ionospheric delay for each satellite. Convergence period using ionospheric delay estimates are shorter compared to the GRAPHIC results.

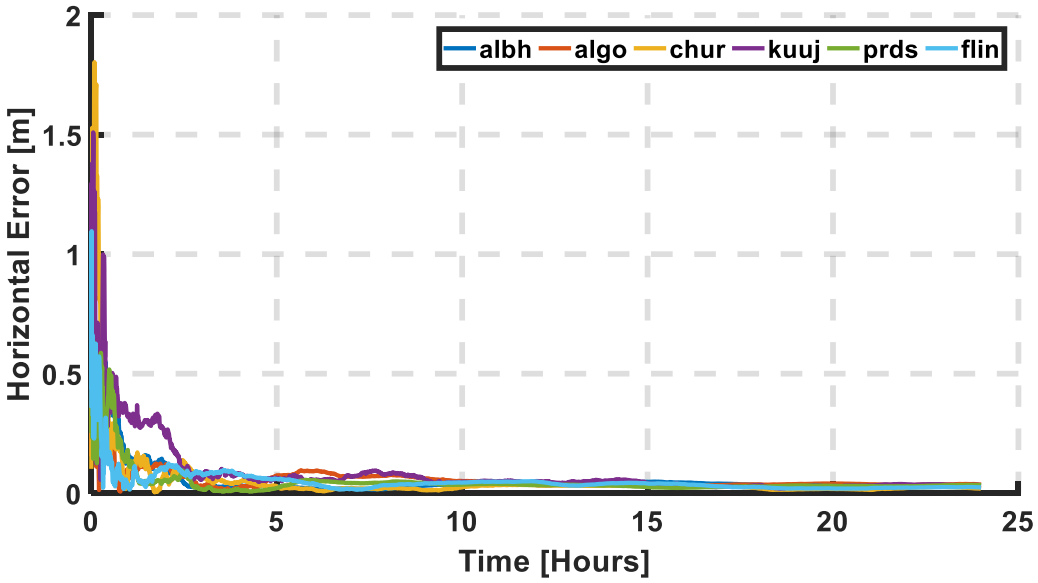

Figure 5.9: Horizontal positioning error on October 1st, 2017 at given stations using GRAPHIC

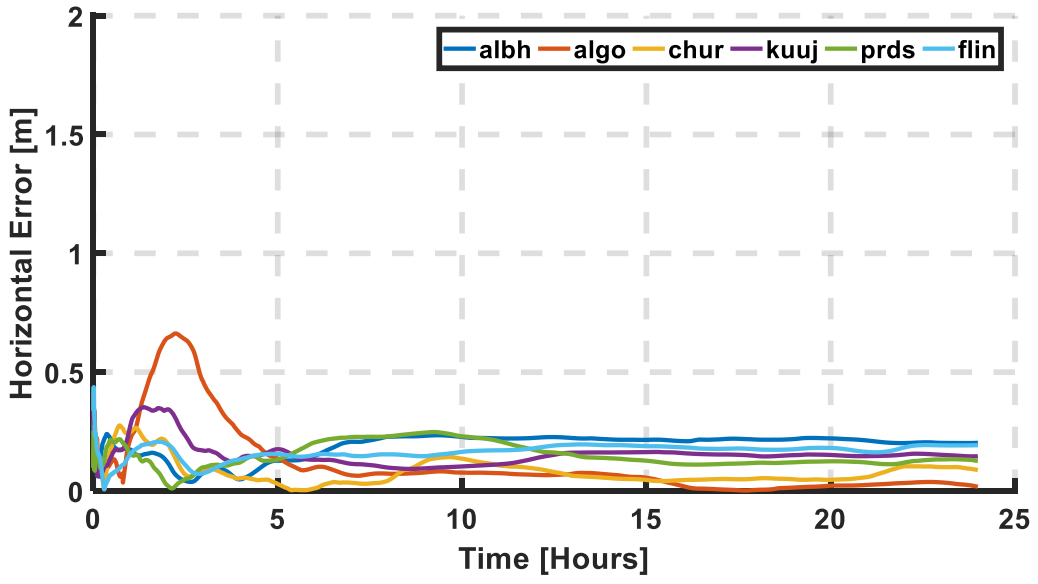

Figure 5.10: Horizontal positioning error on October 1st, 2017 at given stations using uncombined observations

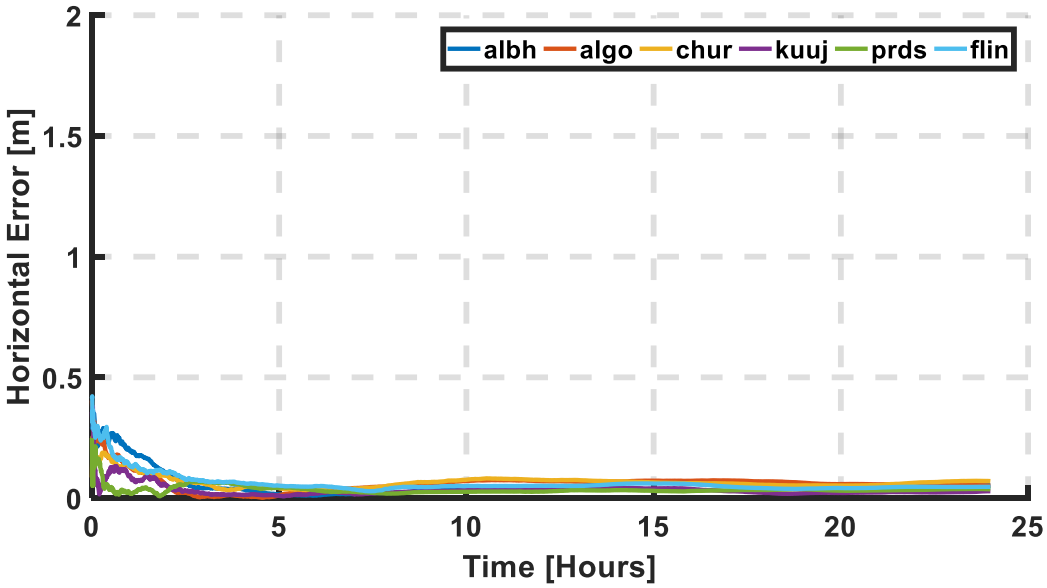

Figure 5.11: Horizontal positioning error on October 1st, 2017 at given stations using ionospheric slant delay estimates in the uncombined filter

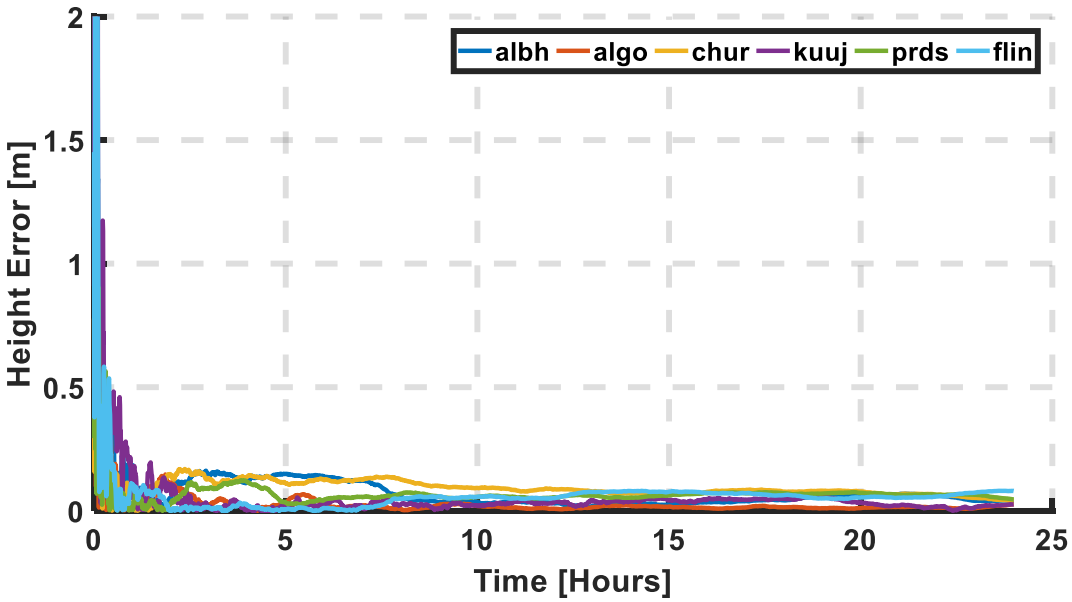

Figure 5.12: Error in height on October 1st, 2017 at given stations using GRAPHIC

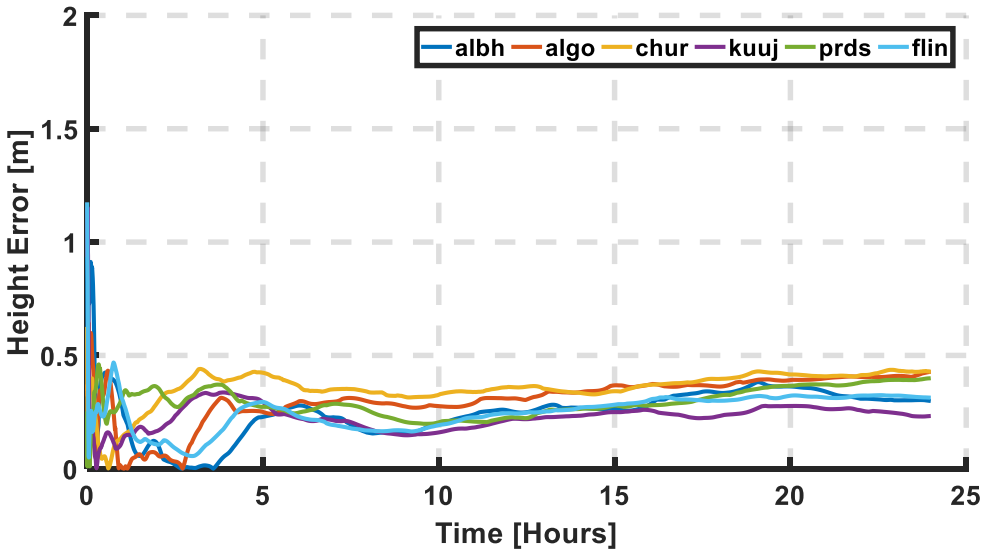

Figure 5.13: Error in height on October 1st, 2017 at given stations using uncombined observations

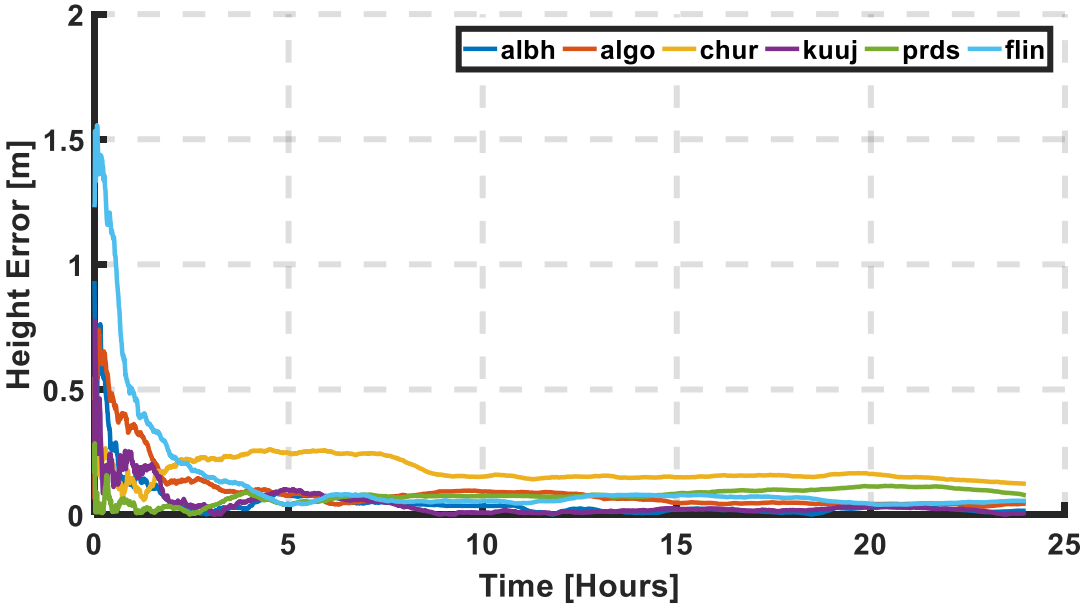

Figure 5.14: Error in height on October 1st, 2017 at given stations using slant delay estimates in the uncombined filter

Figure 5.15 and 5.16 compares the accuracies from multiple stations obtained using uncombined (GIM), uncombined (slant ionospheric delay estimates), and GRAPHIC processing. Horizontal

accuracies are in the range of 3 cm – 5 cm when processed using GRAPHIC combination. CHUR has the lowest horizontal positioning rms of 3 cm. Whereas ALGO has the highest rms of 4.4 cm.

On the other hand, when GIM is used in processing using uncombiend measurements, horizontal rms at each station is greater than 15 cm. ALGO has the lowest horizontal positioning accuracy of 18.3 cm. Whereas accuracies 25.6 cm and 27.7 cm are obtained at stations PRDS and ALBH, respectively. Horizontal accuracy using slant delay estimates is within 4 cm – 9 cm.

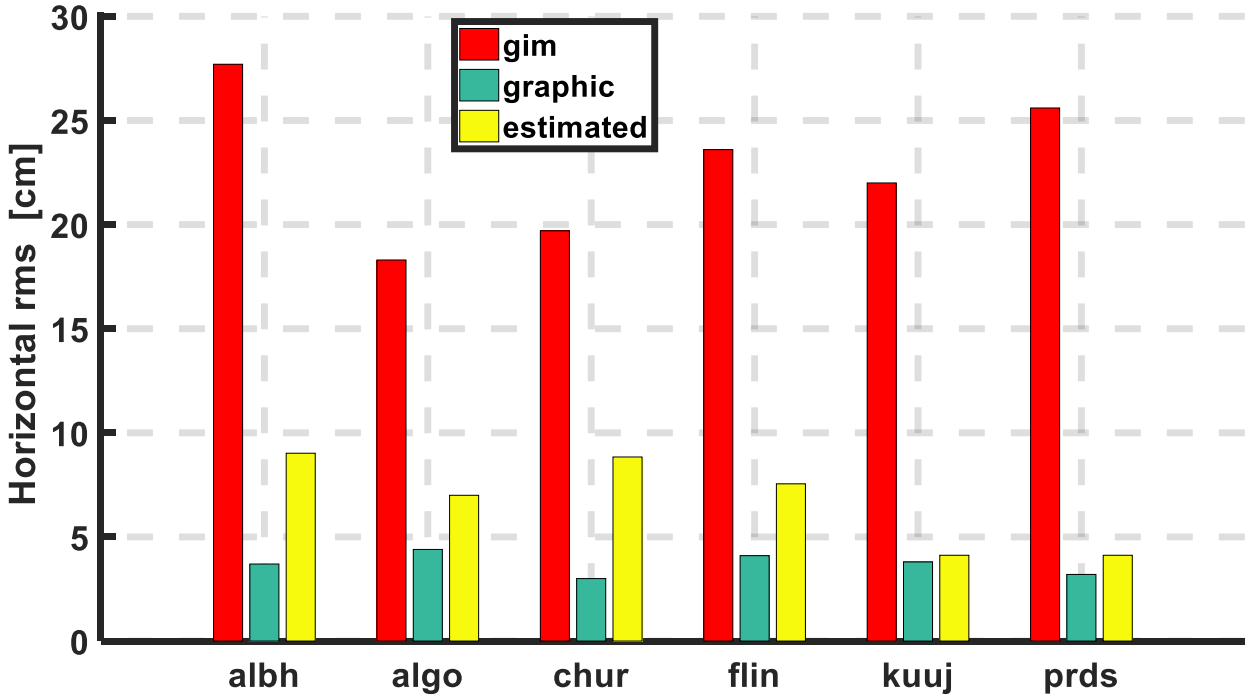

Figure 5.15: Horizontal accuracy comparison of GRAPHIC and uncombined at different stations

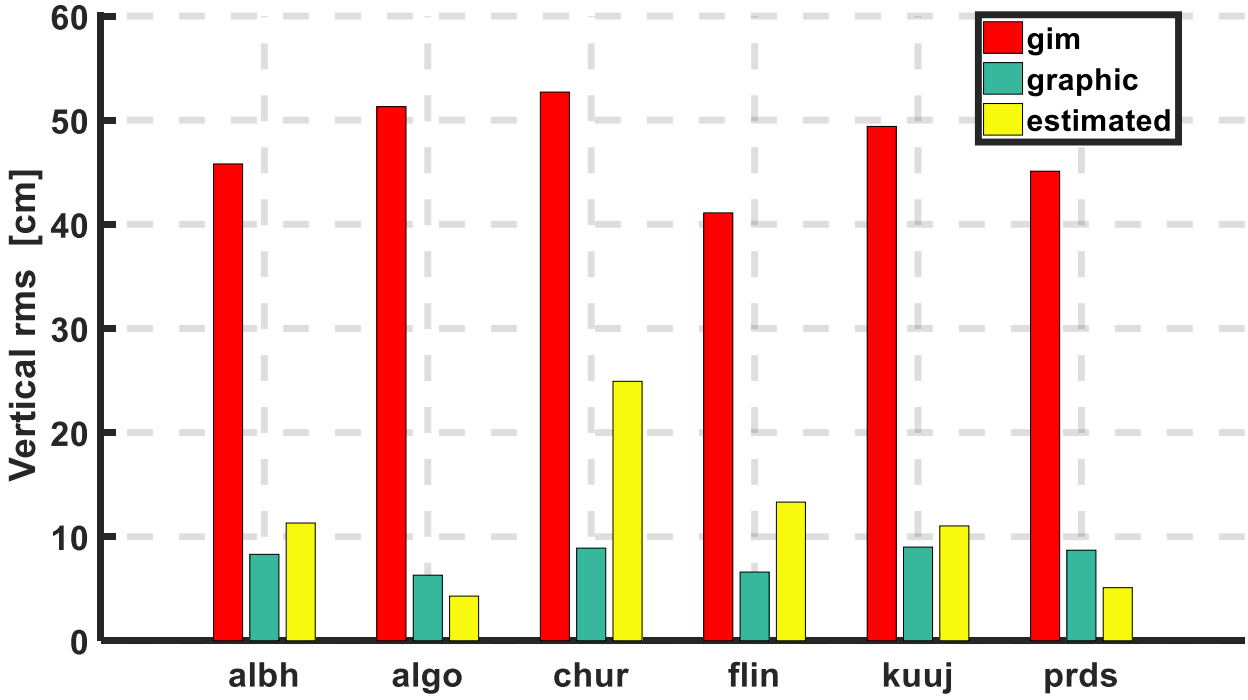

Figure 5.16: Vertical accuracy comparison of GRAPHIC and uncombined at different stations

5.5.2 Low-cost GNSS hardware

Due to the quality of low-cost antenna and GNSS receivers, the quality of the raw observations is inferior compared to raw observations coming from geodetic-grade GNSS hardware. A u-blox NEO-M8T along with a patch antenna was used as an example of low-cost hardware. Two data-sets from NEO-M8T were collected on the rooftop of the Petrie Science and Engineering building, at York University. Datasets were collected at different days during different times to add variability to the analysis.

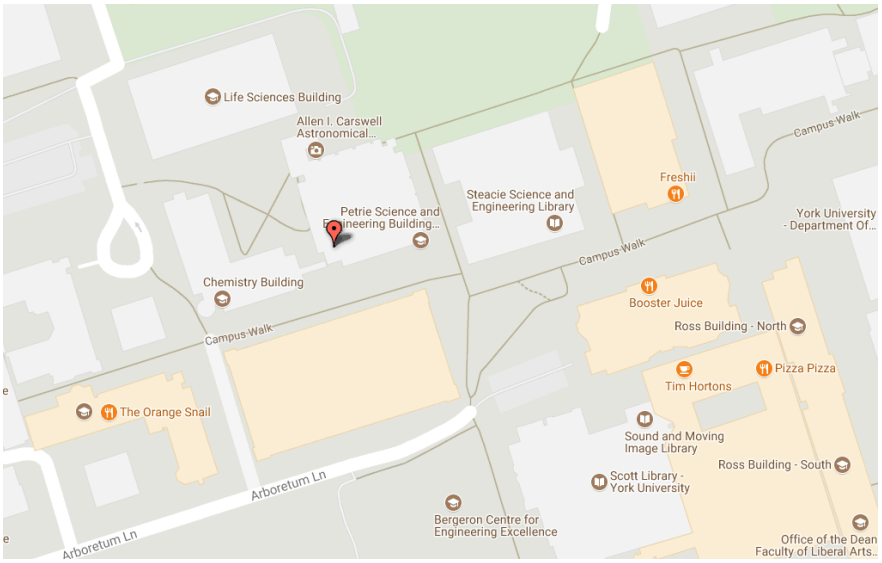

Figure 5.17: Location of Petrie Science and Engineering building., where datasets from low-cost receivers are collected

Figure 5.18 and 5.19 shows the error in northing, easting and up components, processed using GRAPHIC and uncombined observations. It is worth noting that the results from the uncombined processing mode are superior to the combined (GRAPHIC) processing. As listed previously, GRAPHIC is a combination of both code and carrier-phase observation, and the noisy C/A-code observations contaminates the newly formed phase observations. Hence, the uncombined results using GIM are superior to the results from GRAPHIC. The primary reason that uncombined observations, in this case, improve the results is that raw observations coming from low-cost receivers are more affected by multipath and the noise of code observations compared to the raw data from the geodetic grade hardware. Sterle et al. (2015) also note that GIM (uncombined) will improve results when multipath and noisy code observations would prevail over the remaining ionospheric bias.

a). GRAPHIC b). Uncombined

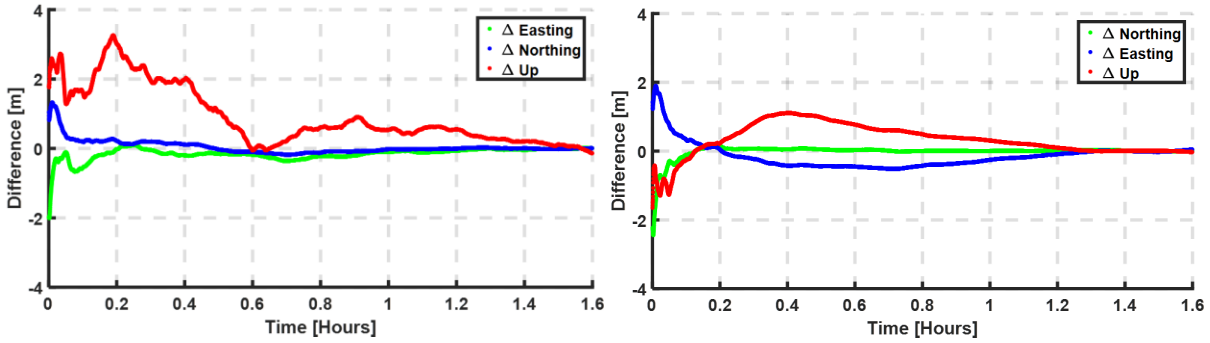

Figure 5.18: Based on raw data collected from NEO-M8T at Petrie Science and Engineering building, York University on Sept 17, 2017. a) represents the discrepancies in N, E and U using GRAPHIC. b) Discrepancies in N, E, U using uncombined

a). GRAPHIC b). Un combined

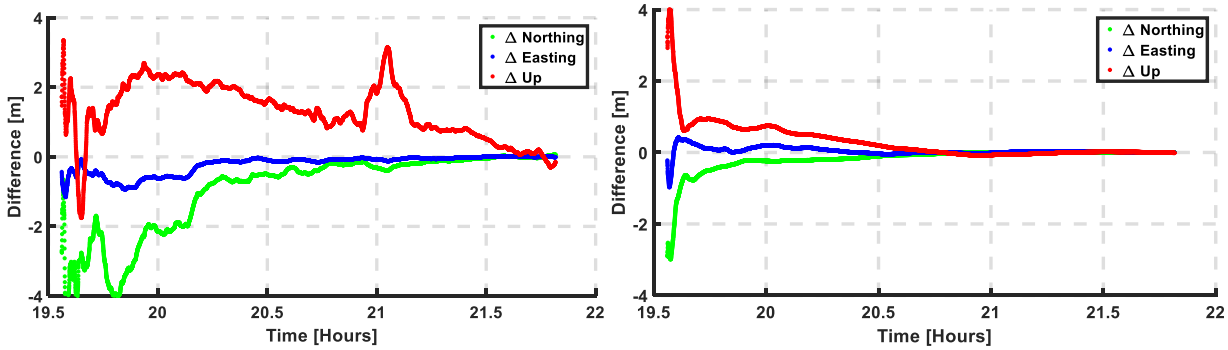

Figure 5.19: Based on raw data collected from NEO-M8T at Petrie Science and Engineering building, York University on Sept 27, 2017. a) represents the discrepancies in N, E and U using GRAPHIC. b) Discrepancies in N, E, U using uncombined

Due to the absence of reference solutions, mean value of last five hundred epochs is assumed as a reference solution.

Table 5.4 below list the biases, standard deviations, and rms of low-cost datasets processing using GRAPHIC and uncombined observations. In uncombined form, horizontal rms is within 10 cm – 15 cm range. Whereas, when using GRAPHIC horizontal rms of approximately 1 metre is observed in the Dataset #2.

Station	Component	Un-Combined [cm]	GRAPHIC [cm]
Dataset# 1	Northing	9	15.7
	Easting	6.1	9.1
	Up	25.4	90.2
	2D	10.9	18.1
	3D	27.6	92
Dataset# 2	Northing	13.3	111.5
	Easting	6.6	29.8
	Up	32.4	155.9
	2D	14.9	115.4
	3D	35.6	194.0

Table 5.4: Final accuracies of un-combined and combined processing of observations from low-cost hardware

5.5.3 Ultra-low-cost hardware

Figure 5.20 shows the PPP results of measurements obtained Nexus 9 tablet. As shown in the previous section, the noise on code observation is few times higher compared to the geodetic observations. Forming the GRAPHIC combination increases the noise on the new phase-observable, which further contaminates the position estimates.

Dataset #1:

a). GRAPHIC b). Uncombined

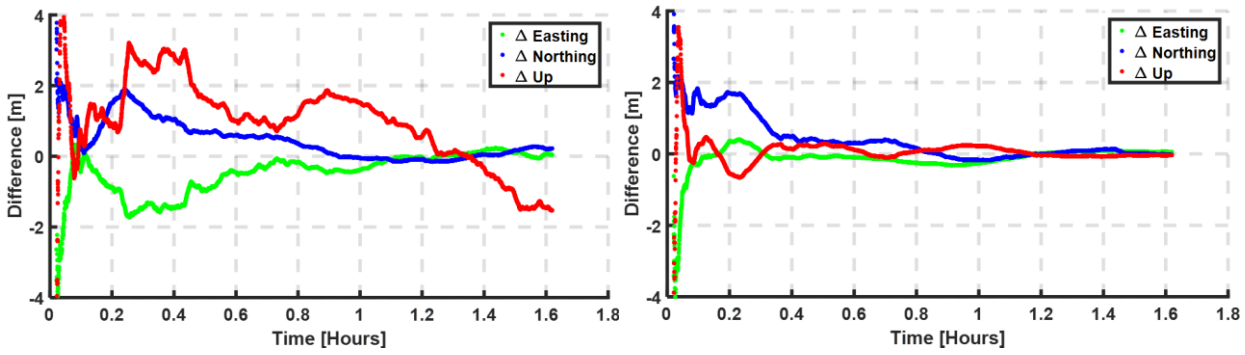

Figure 5.20: Based on raw data collected from Nexus 9 tablet at Petrie Science and Engineering Building., York University on Sept 27, 2017. a) represents the discrepancies in N, E and U using GRAPHIC. b) Discrepancies in N, E, U using uncombined

Table 5.5 below quantifies the accuracies of Nexus 9 dataset processing using GRAPHIC and uncombined form. The horizontal positioning accuracy using GRAPHIC is 81 cm, whereas an accuracy of 35 cm is observed using uncombined observations.

rms	Uncombined [cm]	GRAPHIC [cm]
Northing	15.4	61.4
Easting	31.3	52.8
UP	14	148.4
2D	34.9	80.9
3D	37.6	169.1

Table 5.5: Final accuracies of uncombined and combined processing of observations from ultra-low-cost hardware

5.6 Multi-constellation single-frequency PPP

In the environments such as urban canyons, mountains visibility of signals is hindered and available signals become insufficient. The integration of GPS, GLONASS, Galilo and BeiDou constellations provides more signal, enhances signal geometry and improves the convergence and the quality of the solutions in PPP processing (Lou et al. 2016; Li et al. 2015; Cai and Gao 2013). This integration becomes much more vital in today's dense urban world, especially with the low-cost and ultra-low-cost hardware as most of the users of these devices are situated in the urban setting.

This section lists and compares PPP performance of geodetic-grade hardware using four constellations (GPS, GLONASS, Galileo and BeiDou), and combined GPS and GLONASS to the GPS-only performance. The low-cost and ultra-low-cost hardware analysis is limited to GPS-only and GPS + GLONASS, as the hardware is capable to track signals for these two constellations.

5.6.1 High-end hardware

Figure 5.21 and 5.22 represents the two-dimensional positioning error at station ALGO, processed using GPS-only and GPS + GLONASS measurements, respectively. Vertical errors are depicted in Figures 5.23 and 5.24. Daily horizontal error of 8.6 cm is obtained with GPS-only processing over a week of data, whereas an error of 3.2 cm is obtained when processed using GPS + GLONASS observations. Table 5.6 shows the statistics of the positional components for GPS-only and the combined GPS and GLONASS single-frequency PPP processing for station ALGO over the period of one week. Table 5.6 suggests that the GPS + GLONASS vertical also improved over the GPS single-frequency solutions considering a vertical error of 2.1 cm.

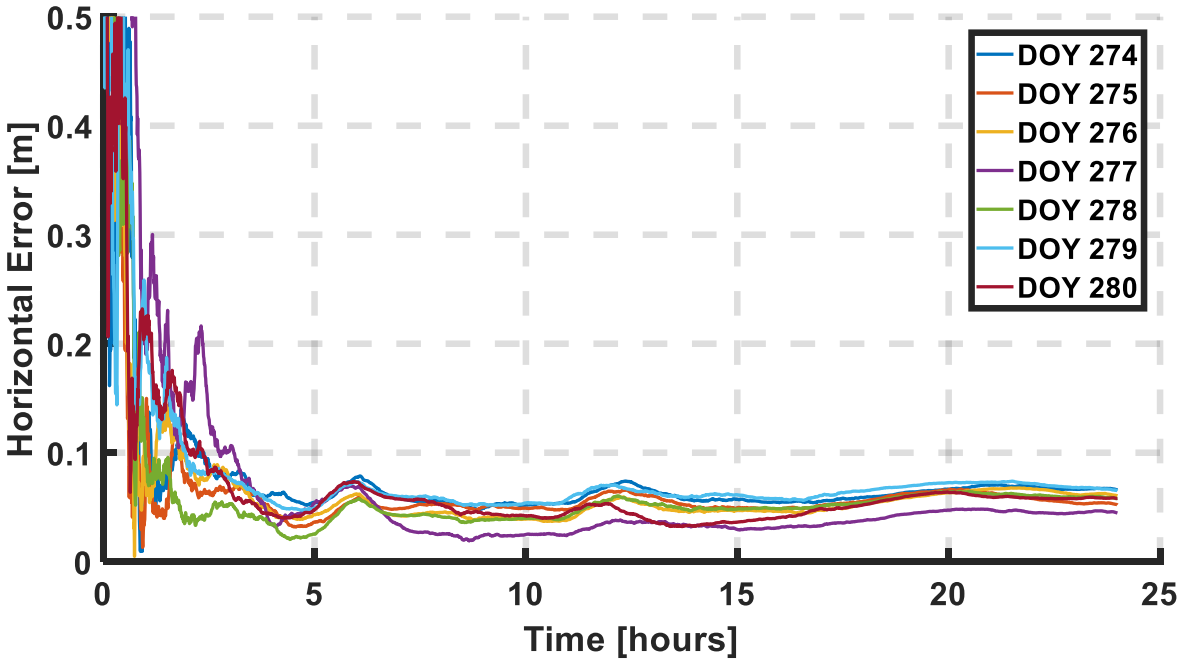

Figure 5.21: Horizontal positioning error on October 1st, 2017- Oct 7, 2017, at station ALGO using GPS-only processing

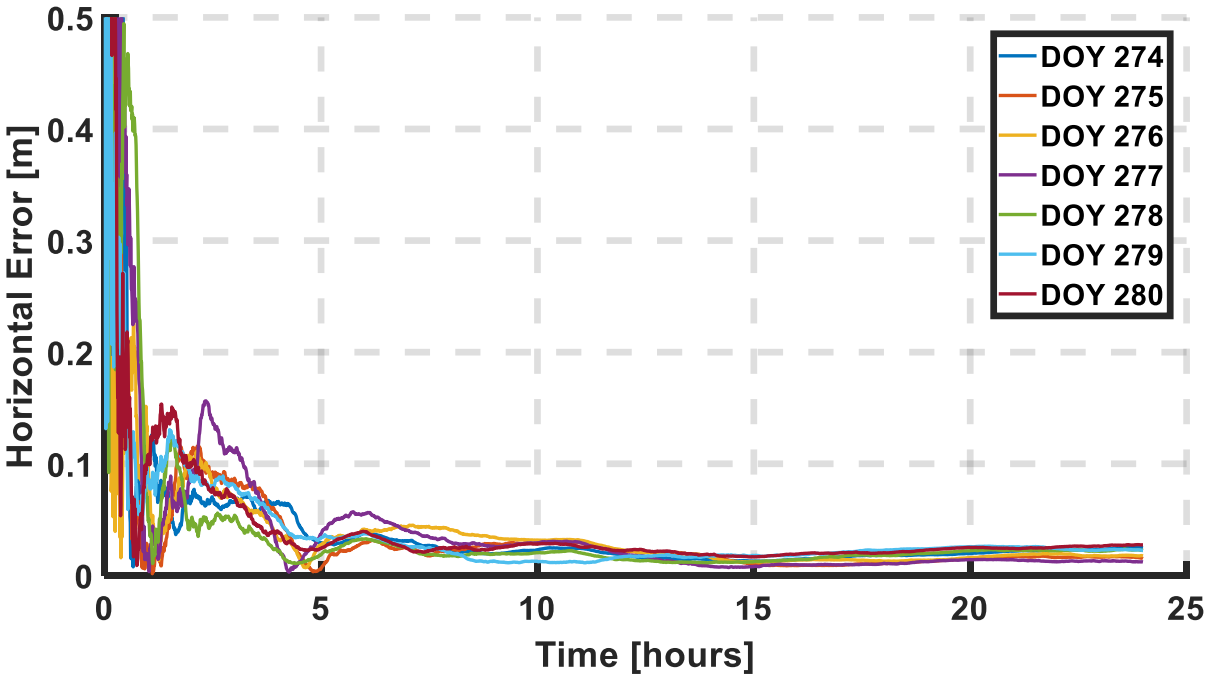

Figure 5.22: Horizontal positioning error on October 1st, 2017- Oct 7, 2017, at station ALGO using GPS+GLONASS

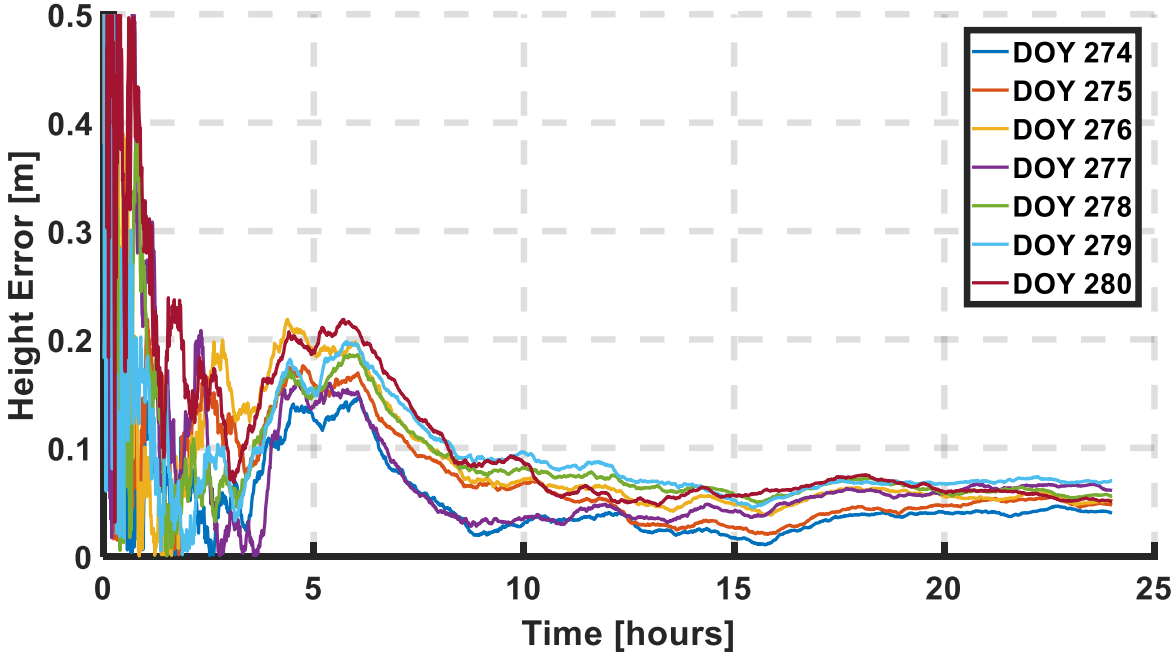

Figure 5.23: Error in height on October 1st, 2017- Oct 7, 2017, at station ALGO using GPS-only processing

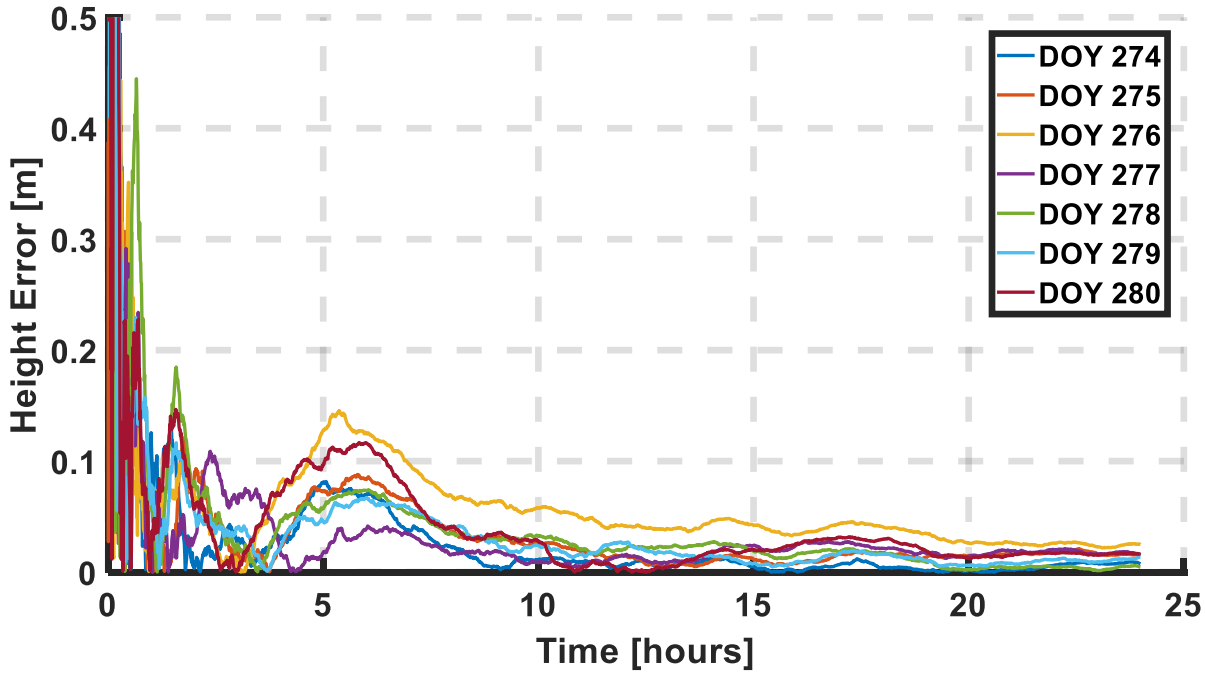

Figure 5.24: Error in height on October 1st, 2017- Oct 7, 2017, at station ALGO using GPS+GLONASS processing

rms	GPS-only [cm]	GPS + GLONASS [cm]
Northing	2.7	2.0
Easting	8.2	2.5
Up	8.1	2.1
2D	8.6	3.2
3D	11.8	3.9

Table 5.6: Average daily results from York GNSS PPP for GPS-only and combined GPS and GLONASS PPP for station ALGO over a one-week period

Results presented suggests that GPS+GLONASS single-frequency PPP performance is significantly superior to GPS-only single-frequency PPP. The inclusion of GLONASS increases

the number of observations, provides good geometry and strengthens the solution accuracy and integrity.

Figure 5.25 shows the horizontal error during first sixty minutes of single-frequency PPP with GPS-only and GPS + GLONASS processing at station ALGO. 90% of the time horizontal error using combined GPS and GLONASS is less than 2 m. Whereas, horizontal error stays at approximately 2 m, 50% of the time when GPS-only observations are used.

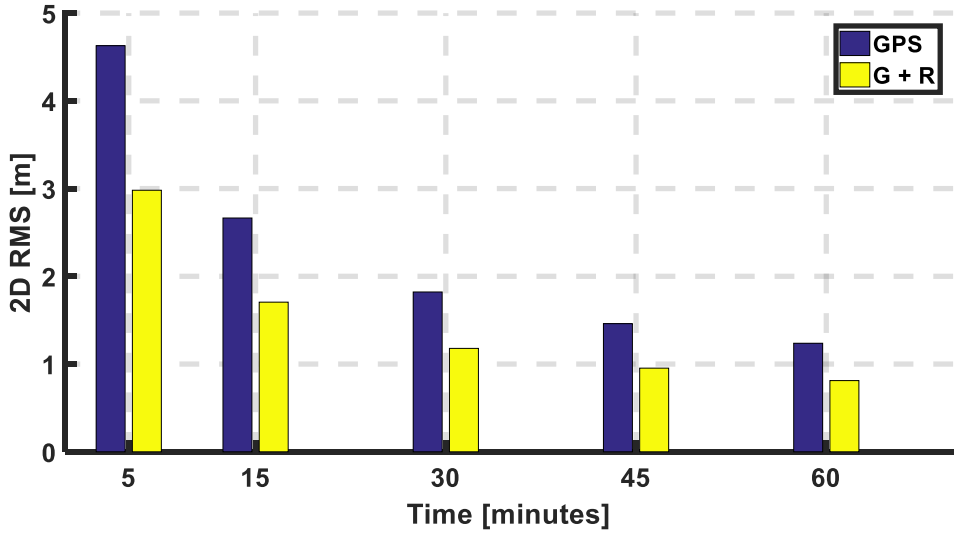

Figure 5.25: Comparison of horizontal positioning error between GPS-only and GPS + GLONASS processing during first 60 minutes of processing

It can be concluded that combined GPS and GLONASS single-frequency PPP not only improves positioning accuracy, but also helps in the reduction of convergence time. The solution quality gets better as GLONASS contributes more signal and satellites and improves the satellite geometry, leading to a stronger DOP. However, the position accuracy in a combined GPS and GLONASS solution can be said to be driven by the GPS solution as 50% of less weight is assigned to the noisier GLONASS observations.

Different stations

To further access the performance of York PPP processor, 24-hour of L1 and C/A-code-only observations were processed using the distribution of 6 Canadian IGS stations as previously listed in Figure 5.4. Figure 5.26 and 5.27 shows the horizontal and vertical accuracies comparison of SF-PPP with GPS-only and GPS + GLONASS observations. Final horizontal positioning accuracy for all stations using GPS-only observations is within the range of 3 to 5 cm. On the other hand, when combined GPS and GLONASS observations are used, the errors are in the range of 3 to 4 cm in horizontal, and 5 to 8 cm in the vertical component.

With combined GPS and GLONASS observations, the minimum horizontal positioning error observed is 2.6 cm at station PRDS and FLIN has a maximum error of 3.7 cm. At station ALGO error in the vertical component is 2.8 cm when GPS + GLONASS observations are used, whereas, an error of 6.3 cm is observed when GPS-only observations are used. Similar drastic improvements in the vertical component are also observed at stations CHUR, FLIN, and PRDS. Maximum improvement in the horizontal positioning occured at station PRDS, where accuracy improved from 3.2 cm to 2.6 cm when combined GPS and GLONASS observations were used.

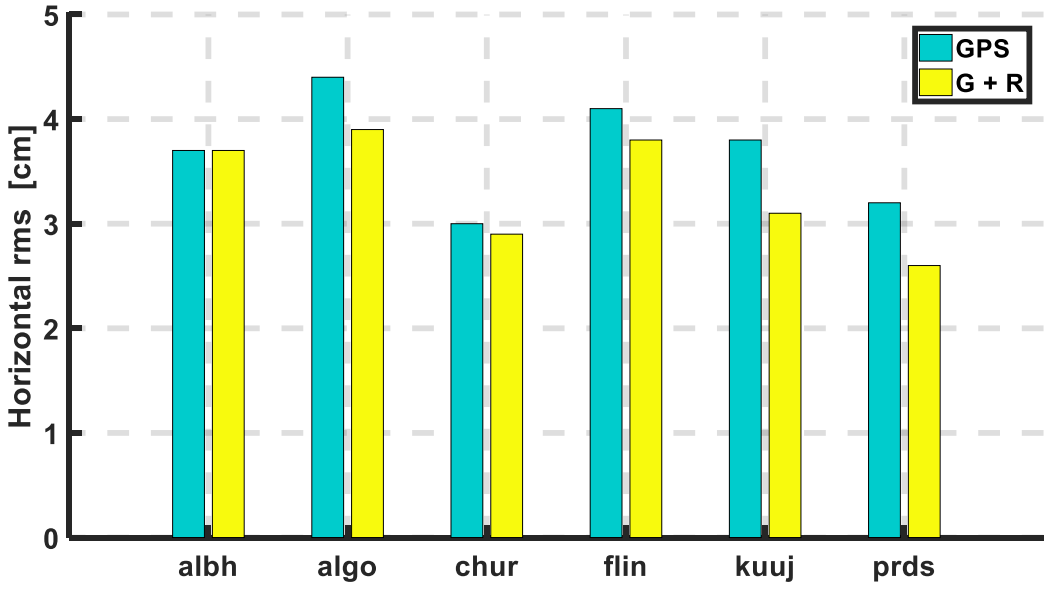

Figure 5.26: Horizontal accuracy comparison for GPS-only and combined GPS and GLONASS processing at different stations

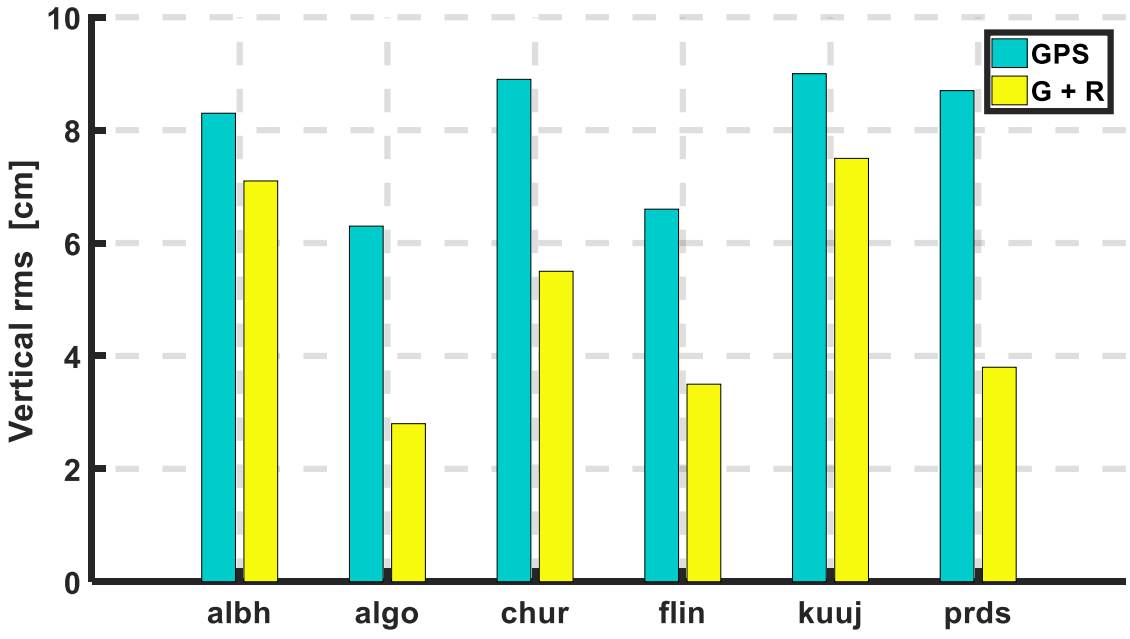

Figure 5.27: Vertical accuracy comparison for GPS-only and combined GPS and GLONASS processing at different stations

Figure 5.26 and 5.27 shows an improvement in the positioning rms with combined GPS and GLONASS observations. However, the statistics represent the converged accuracy, i.e., statistics are computed after the convergence period.

Despite of the improvements in the converged accuracies, Figures 5.26 and 5.27 does not capture the full spectrum of benefits of using combined GPS and GLONASS. Figure 5.28 depicts the convergence time of York single-frequency PPP engine with GPS-only and GPS + GLONASS observations. The threshold of 1 dm for geodetic-grade hardware is assumed in this research, i.e., the time it takes PPP solution to converge to 1 dm level of accuracy.

At station ALBH, CHUR and KUUJ it takes more than an hour for a GPS-only solution to converge to 1 dm whereas combined GPS and GLONASS solution converge to the same level of accuracy within less than half an hour. It is also interesting to note that combined GPS and GLONASS solution did not provide much further improvement in terms of convergence at station ALGO and PRDS, where GPS-only convergence time is already less than 30 minutes. So, combined GPS and GLONASS provided more consistent initial convergence.

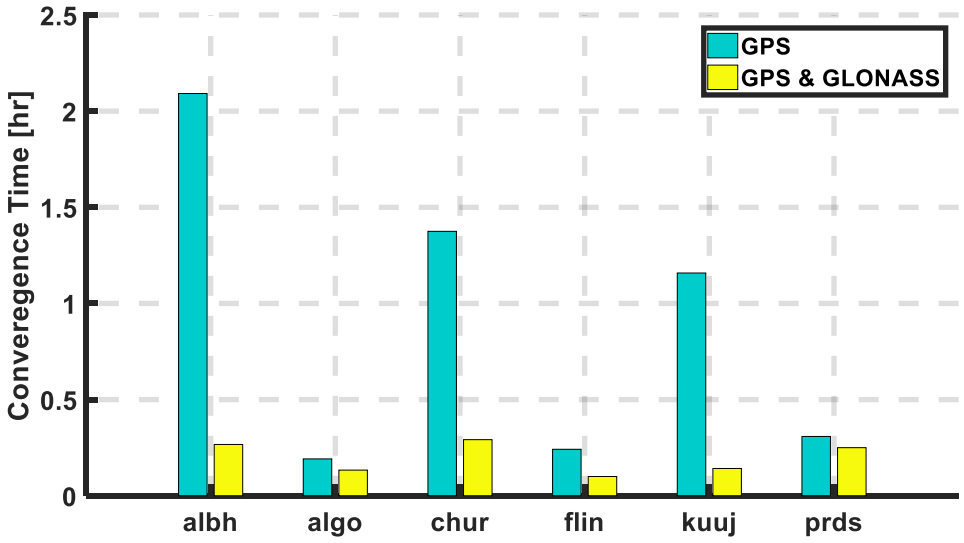

Figure 5.28: Convergence time for 6 Canadian IGS stations for the horizontal position processed using GPS-only and combined GPS and GLONASS with the threshold of 1 dm.

Different station with GPS, GLONASS, Galileo and BeiDou

Figure 5.29 compares the horizontal positioning results at station FTNA on February 1, 2016 using four constellations (GPS, GLONASS, Galileo and BeiDou). Yellow curve (GPS + GLONASS, Galileo, and BeiDou) suggests that the all constellation solution converges (< 0.1 m) faster than the GPS + GLONASS and GPS-only solution. Figure 5.30 shows the daily mean horizontal and vertical rms of 4 stations (FTNA, REDU, GMSD and DYNG). As expected, four constellation solution accuracies are superior to the combined GPS and GLONASS.

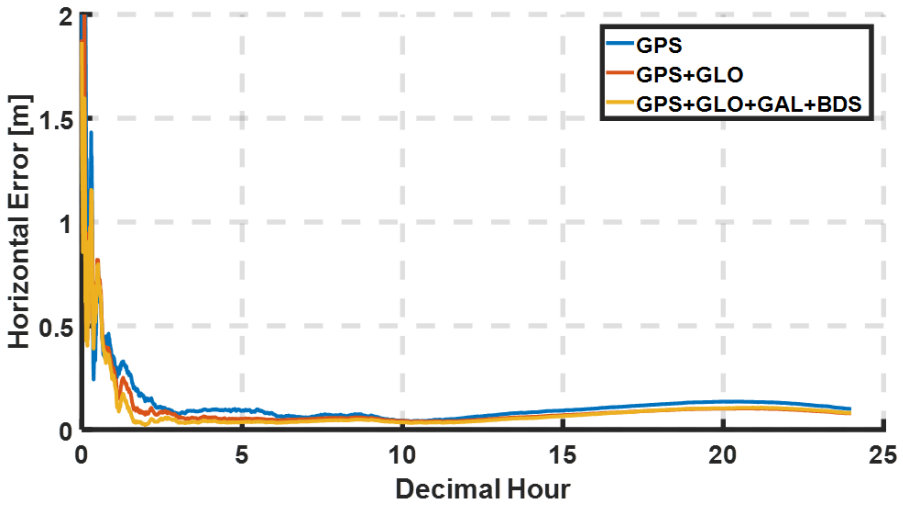

Figure 5.29: Horizontal positioning error at station FTNA on February 1, 2016 using all four constellations, combined GPS and GLONASS, and GPS-only processing

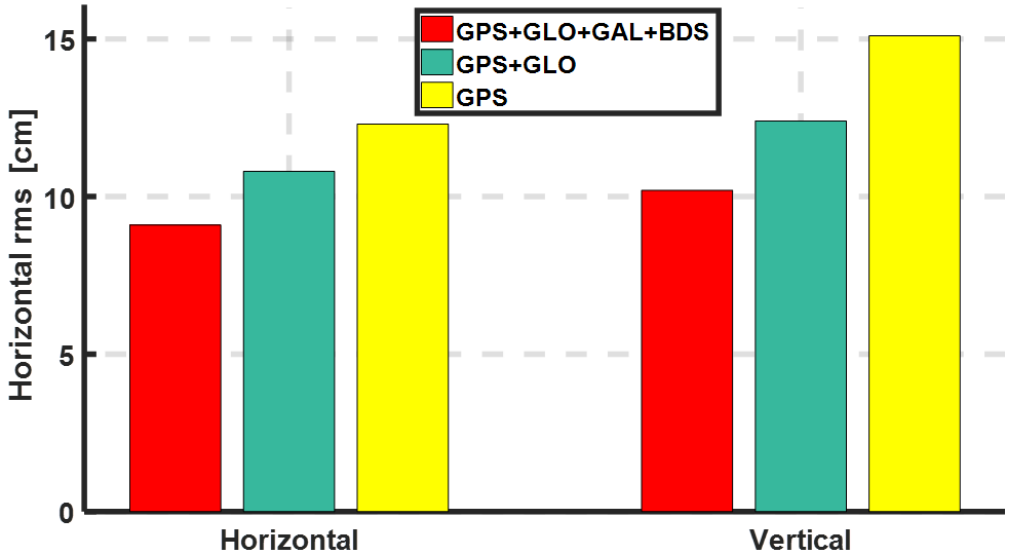

Figure 5.30: Horizontal and vertical rms comparison of all four constellations, combined GPS and GLONASS to GPS-only

5.6.2 Low-cost hardware

York single-frequency PPP engine performance is further assessed with observations processed from the u-blox NEO-M8T receiver and patch antenna. This section lists the comparison of GPS-

only PPP processing to the GPS + GLONASS. Three datasets were collected, as previously listed in Figure 5.13 on different days and time intervals to ensure the variability in the geometry of the satellites.

Figure 5.31 – 5.36 shows the error is northing, easting and the vertical component of three datasets processed with the York single-frequency PPP engine using GPS-only L1 and C/A-code, and combined GPS and GLONASS measurements. Due to the absence of a reference solution, the reference coordinates have been estimated from the datasets themselves, so potential biases make the interpretation of results somewhat optimistic.

From Figures 5.32, 5.34, 5.36 it is apparent that in all three datasets the combined GPS and GLONASS results are superior to the GPS-only results. It can also be noticed that combined GPS and GLONASS solution is more stable after the convergence compared to the GPS-only solution.

Dataset #1

GPS-only

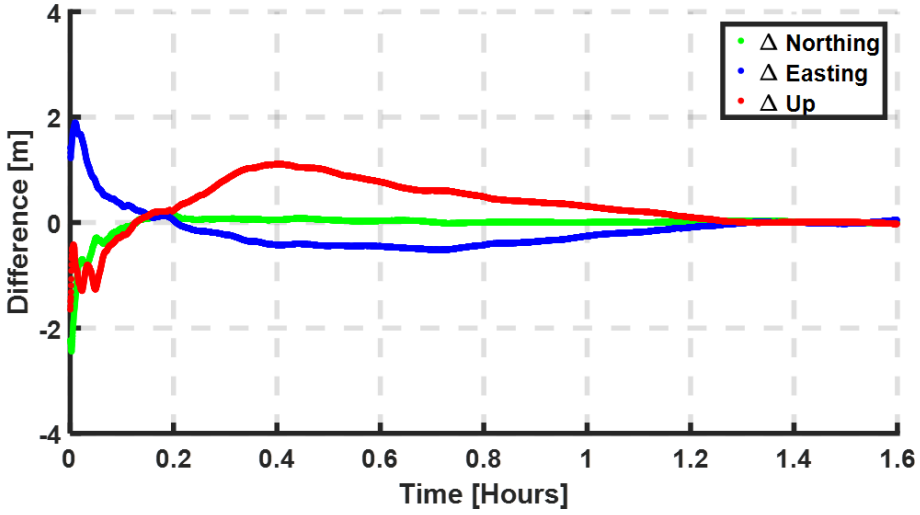

Figure 5.31: Discrepancies in N, E, U components in Dataset# 1, collected at York University processed using GPS-only measurements

GPS + GLONASS

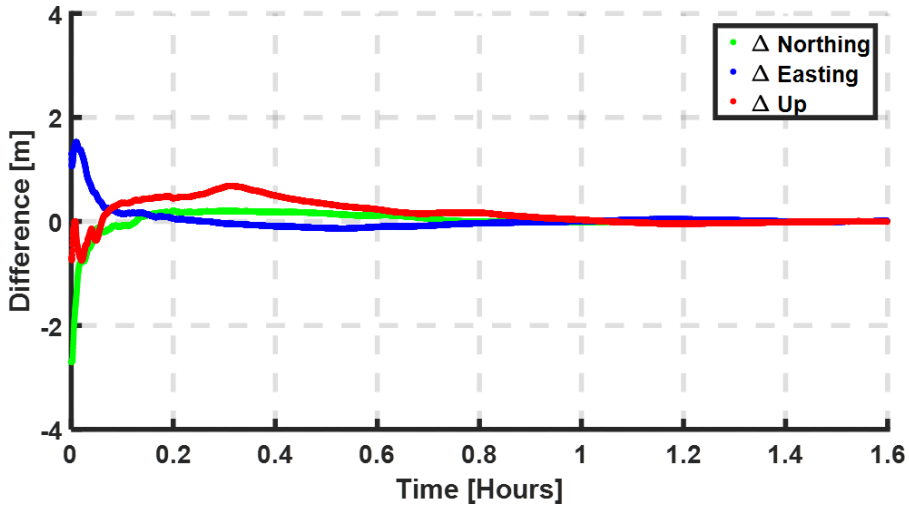

Figure 5.32: Discrepancies in N, E, U components in Dataset# 1, collected at York University processed using GPS + GLONASS measurements

Dataset #2

GPS-only

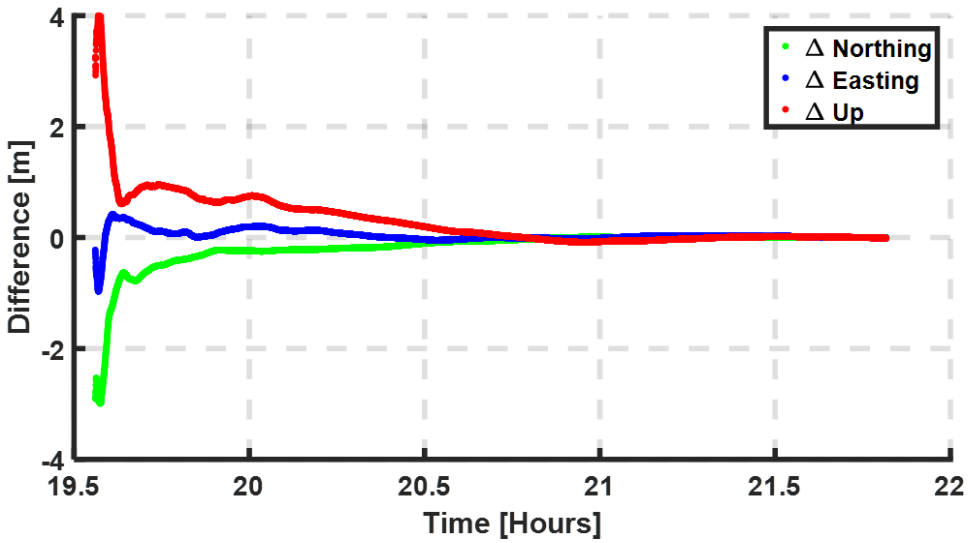

Figure 5.33: Discrepancies in N, E, U components in Dataset# 2, collected at York University processed using GPS-only measurements

GPS + GLONASS

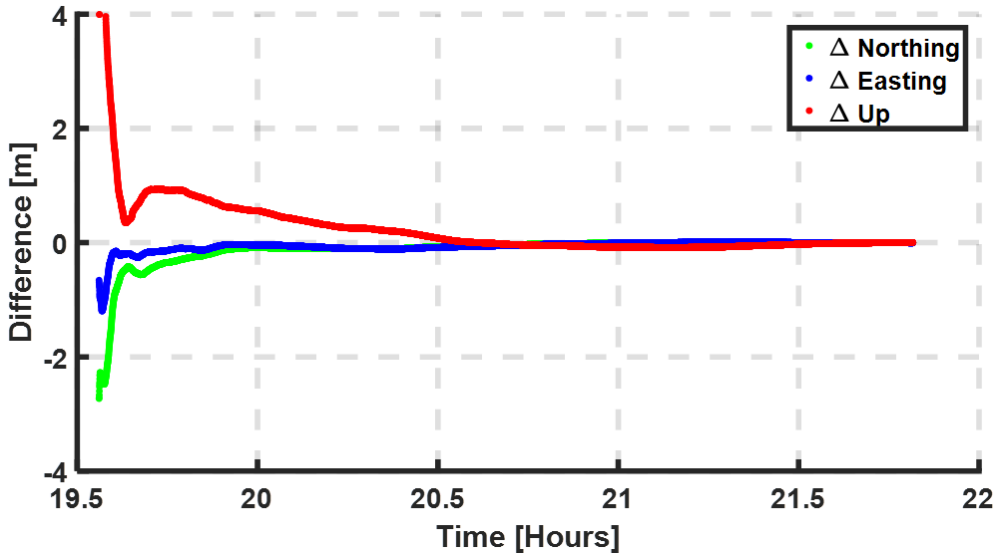

Figure 5.34: Discrepancies in N, E, U components in Dataset# 2, collected at York University processed using GPS + GLONASS measurements

Dataset #3

GPS-only

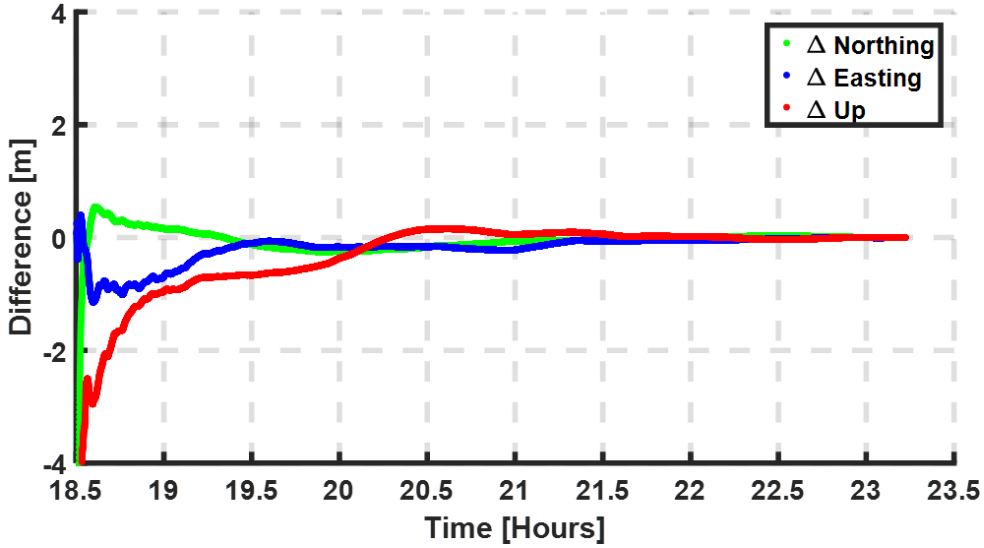

Figure 5.35:Discrepancies in N, E, U components in Dataset# 3, collected at York University processed using GPS-only measurements

GPS + GLONASS

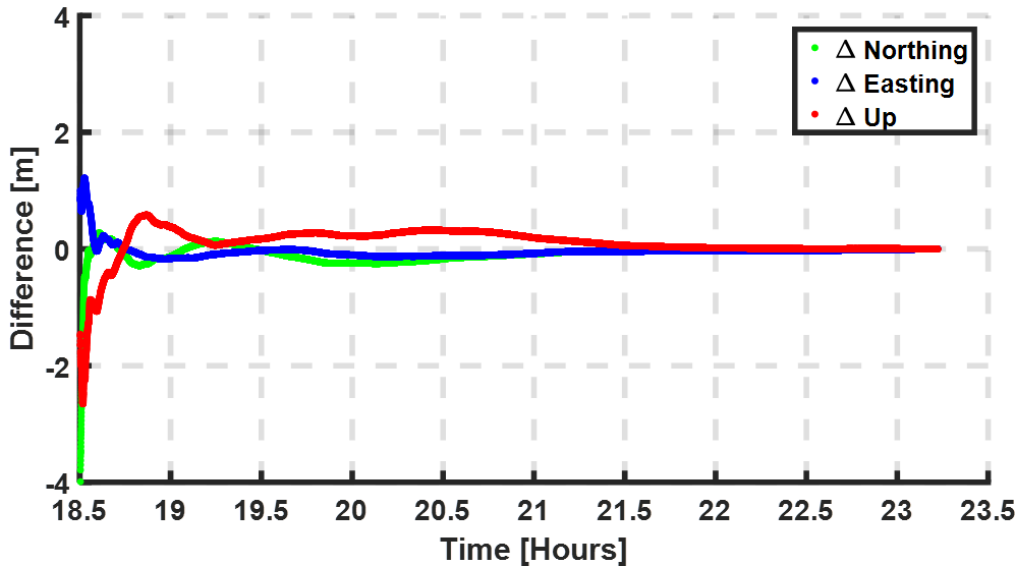

Figure 5.36: Discrepancies in N, E, U components in Dataset# 3, collected at York University processed using GPS + GLONASS measurements

Figure 5.37 shows the rms comparison of the three datasets processed using GPS-only and GPS + GLONASS observations. Average horizontal and vertical positioning error from the three datasets is 18 cm and 38 cm, respectively, when processed using GPS-only observations. On the other hand, horizontal and vertical accuracies of 10 cm and 24 cm are observed with combined GPS and GLONASS processing. Dataset #3 shows the greatest improvement in the horizontal positioning error: the accuracy improved by 14 cm when combined GPS and GLONASS measurements are introduced. Noticeable improvements in the vertical components of all three datasets are also observed with combined GPS and GLONASS processing.

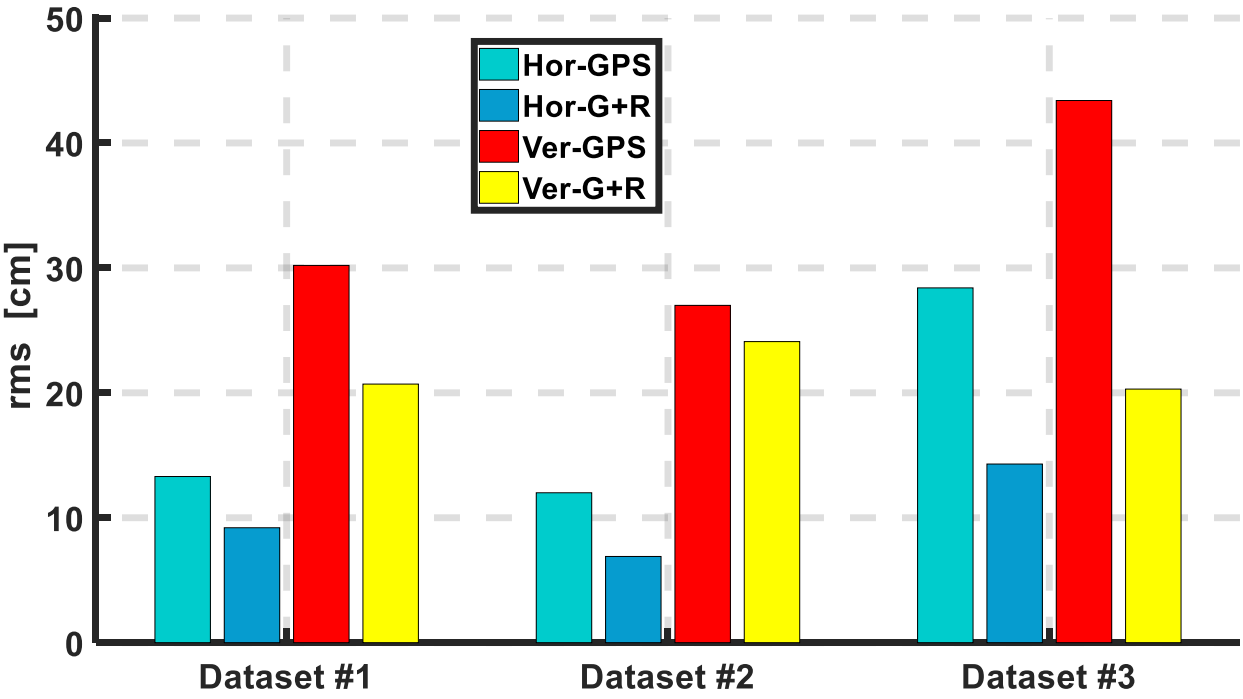

Figure 5.37: Horizontal and vertical rms of three datasets obtained from u-blox NEO-M8T processed using GPS-only and GPS + GLONASS measurements

Figure 5.38 represents the horizontal error in first 60 minutes of processing using GPS and GPS + GLONASS observations. Few decimetre-level improvement in horizontal accuracy is observed in two datasets when combined GPS + GLONASS measurements are used. Whereas, improvement at the few metres-level in horizontal accuracy is observed at Dataset #3. It is interesting to note that when the horizontal accuracy of GPS-only processing is approximately 3 metres then combined GPS + GLONASS observations do not provide a significant improvement in the convergence time. Less improvement in accuracy is primarily because raw GNSS signals from low-cost hardware are noisy compared to signals from geodetic-grade receivers. The extra degree of freedom and variability in geometry that combined GPS and GLONASS measurements bring are used initially towards averaging out unmodelled ionospheric biases and the signal noise. This is the foremost reason why there is an overall improvement in accuracy with combined GPS and

GLONASS observations, but the benefits are less significant in first tens of minutes of processing when the GPS-only horizontal accuracy is a few metres. In dataset #3 accuracy using GPS-only measurements is poor compared to the dataset #1 and #2. Low number of satellites and high DOP values are the primary reasons for the poor initial accuracy in dataset #3.

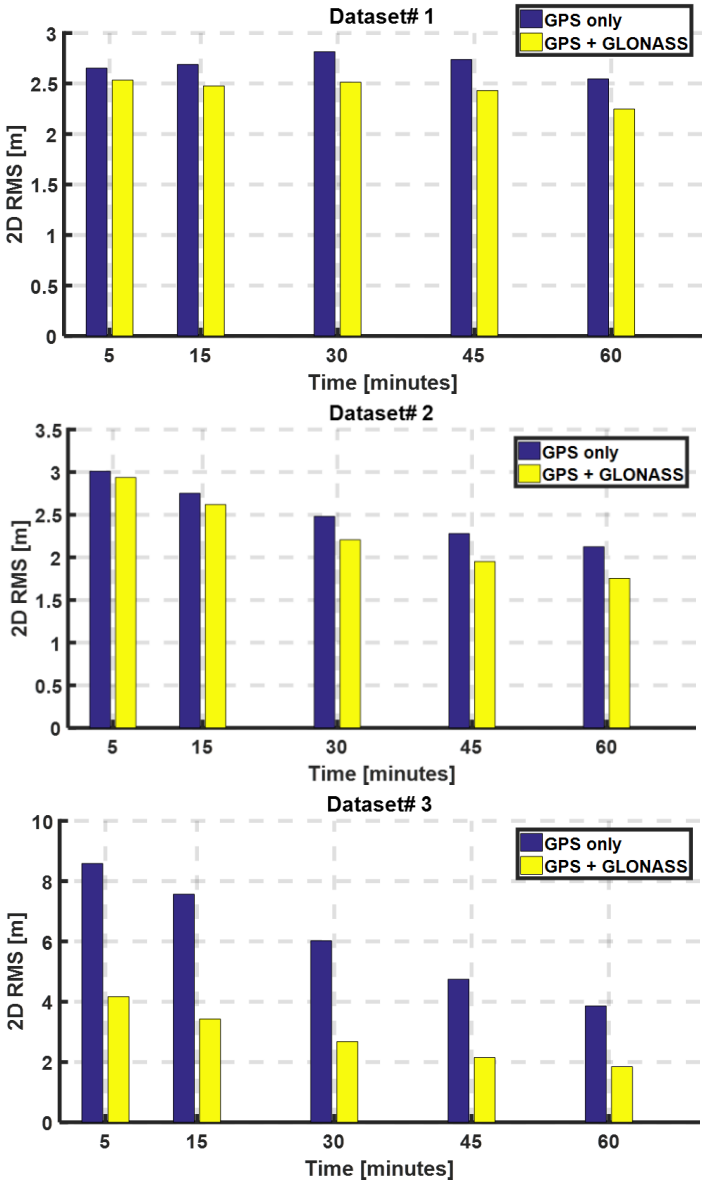

Figure 5.38: Horizontal positioning error from three datasets, during first 60 minutes of processing of L1 and C/A-code GPS-only and combined GPS and GLONASS observations

5.6.3 Ultra-low-cost hardware

This section compares the PPP results of datasets collected using a Nexus 9 tablet. GPS-only PPP results are compared to GPS + GLONASS. As shown in the previous sections, signals are much noiser from Nexus 9 datasets compared as to those from geodetic and low-cost hardware. So, using GLONASS helps more in covering the deficiencies in the GPS-only processing. Figures 5.39 – 5.42 shows the error is northing, easting and the vertical components of two datasets processed with the York single-frequency PPP engine using GPS-only and combined GPS and GLONASS observations. Similar to the low-cost reference solution, the reference coordinates have been estimated from the datasets themselves, so the presence of potential biases in the computed reference solution may make the results a little optimistic. As expected, Figures 5.40 and 5.42 shows that the combined GPS and GLONASS results are superior to the GPS-only results as the combined GPS and GLONASS solution is more stable after the initial solution convergence compared to the GPS-only solution.

Dataset #1

<u>GPS-only</u>

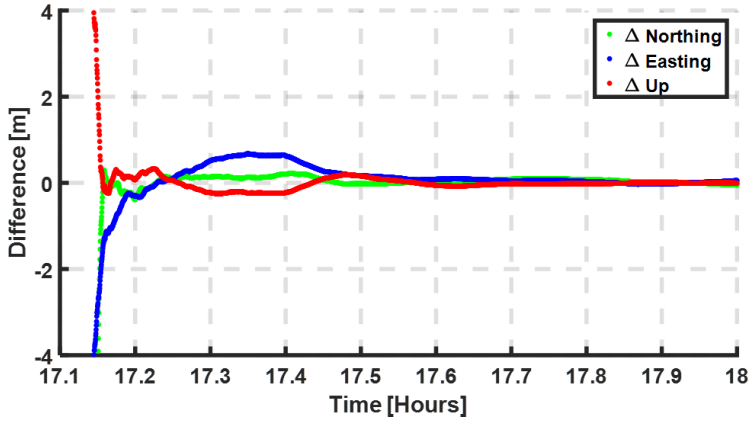

Figure 5.39: Discrepancies in N, E, U component in Dataset #1 collected at York University processed using GPS-only measurements from Nexus 9

GPS + GLONASS

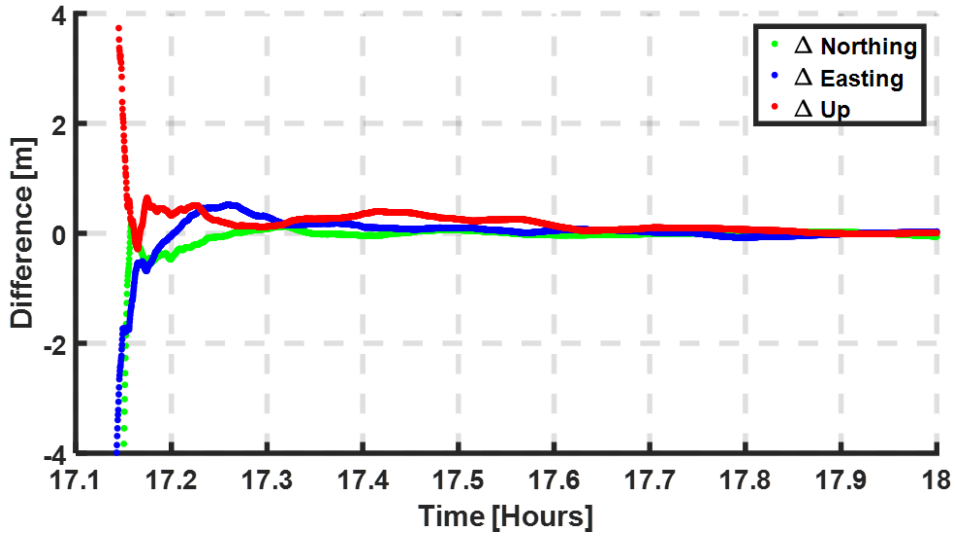

Figure 5.40: Discrepancies in N, E, U component in Dataset #1 collected at York University processed using GPS + GLONASS measurements from Nexus 9

Dataset #2

GPS-only

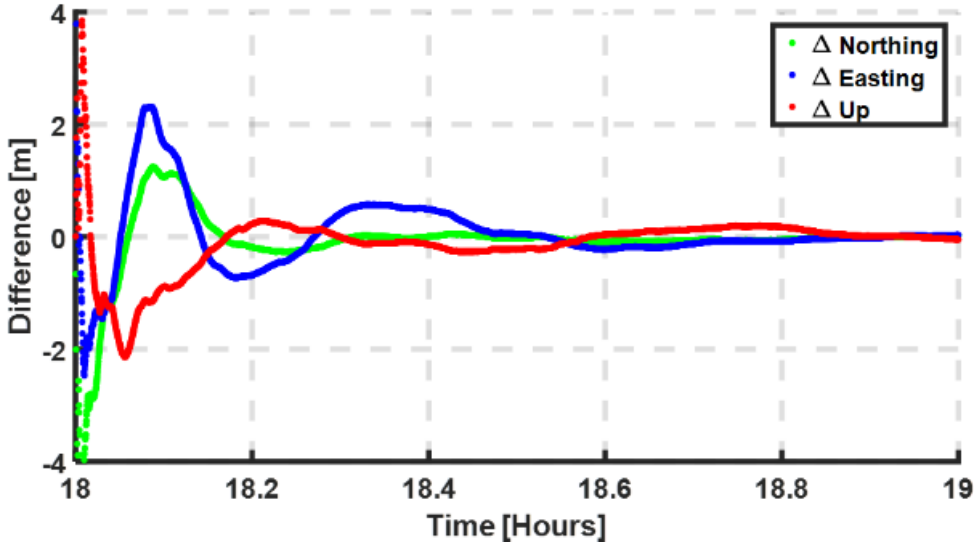

Figure 5.41: Discrepancies in N, E, U component in Dataset #2 collected at York University processed using GPS-only measurements from Nexus 9

GPS + GLONASS

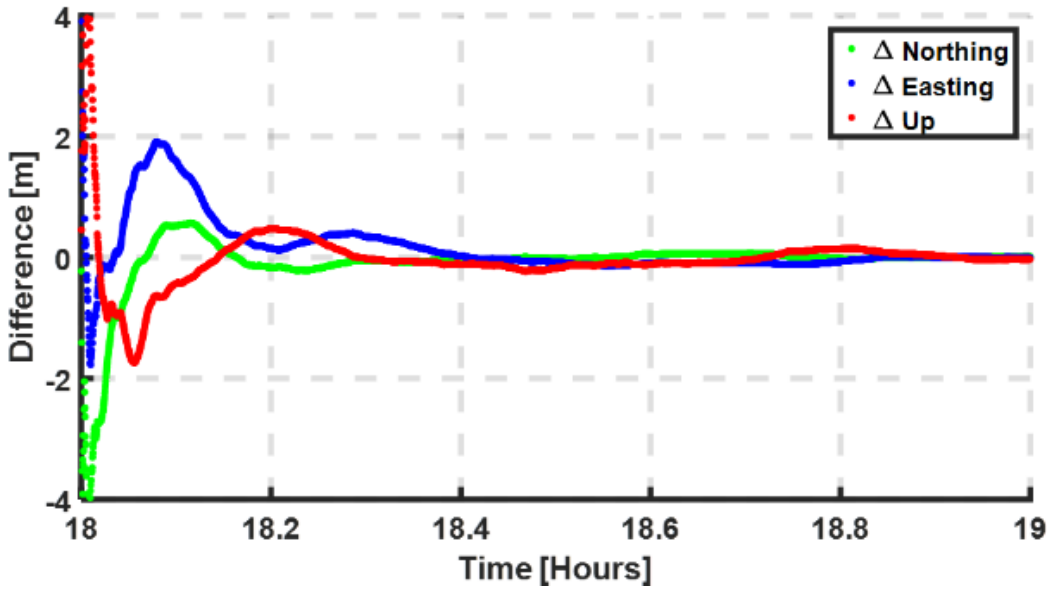

Figure 5.42: Discrepancies in N, E, U component in Dataset #2 collected at York University processed using GPS + GLONASS measurements from Nexus 9

Figure 5.43 shows the rms and the comparison of two datasets processed using GPS-only and combined GPS and GLONASS observations. Horizontal positioning error from the processed datasets is 28 cm, when processed using GPS-only observations. On the other hand, horizontal accuracies of 16 cm and 9 cm are observed with combined GPS and GLONASS processing.

Noticeable improvements in horizontal and vertical components of both datasets are observed with combined GPS and GLONASS processing.

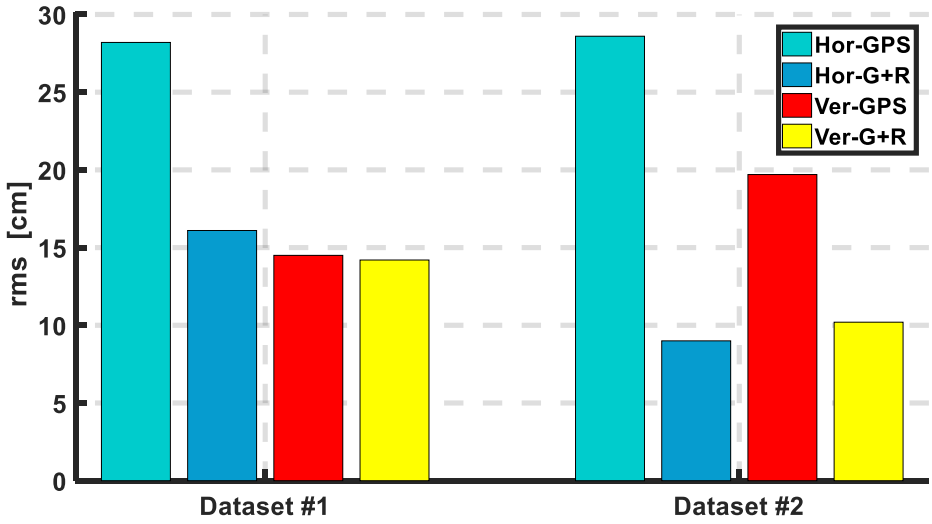

Figure 5.43: Horizontal and vertical rms of two datasets obtained from Nexus 9 tablet, and processed using GPS-only and GPS + GLONASS measurements

Figure 5.44 shows the convergence time of York single-frequency PPP engine processed with GPS-only and GPS + GLONASS observations with a threshold of 3 dm. Slight improvement in convergence time is observed in Dataset #1. However, the magnitude of improvement is negligible compared to the improvements seen with geodetic hardware. In the previous section, it is shown that the raw observations from geodetic-grade hardware are much less noisy compared to the Nexus 9 GNSS observations. As the convergence time is mainly proportional to the unmodelled ionospheric biases and the noise on the signal. So, the more signals and variability in geometry that GLONASS brings is used initially to average out unmodelled ionosphere and signal noise. So, the noise on the measurements and the quality of GLONASS measurements from Nexus 9 is the primary reason why there is less improvement observed in the first few minutes with Nexus 9 datasets processed with GPS + GLONASS compared to GPS-only processing.

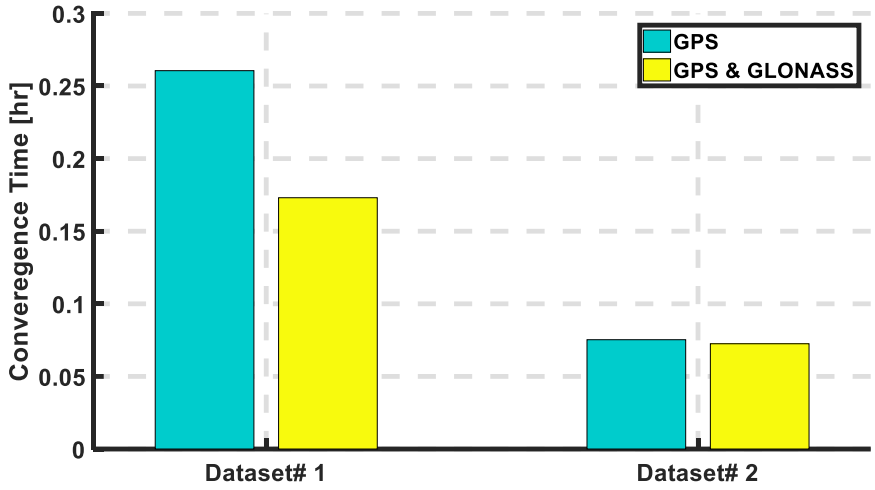

Figure 5.44: Convergence time of datasets from Nexus 9, for the horizontal position processed using GPS-only and combined GPS and GLONASS with the threshold of 3 dm.

5.6.4 Post-fit residuals

Figure 5.45 and Figure 5.46 show the comparison in the magnitude of code and carrier-phase residuals from geodetic-grade, u-blox and Nexus 9 for all observed satellites. The residuals are plotted as a function of time. In general, the residuals are caused by the fact that not all errors are considered in the data processing software, e.g., multipath, GNSS receiver, antenna type, internal tracking methodology (Choy 2009).

It can be observed from Figures 5.45 and 5.46 that post-fit residuals from the Nexus 9 have highest RMS of 3.11 m and 0.18 m of C/A-code and carrier-phase, respectively. Whereas, the geodetic-grade has the lowest RMS of 35 cm and 2 cm from post-fit C/A-code and carrier-phase residuals. The primary reasons for the high RMS of Nexus 9 residuals are the receiver and the antenna type as listed above. Because of the linearly polarized nature of Nexus 9 antenna, the signal from Nexus 9 is more prone to the multipath, which is also one the reason for the high rms of Nexus 9 post-fit residuals compared to the geodetic-grade and u-blox.

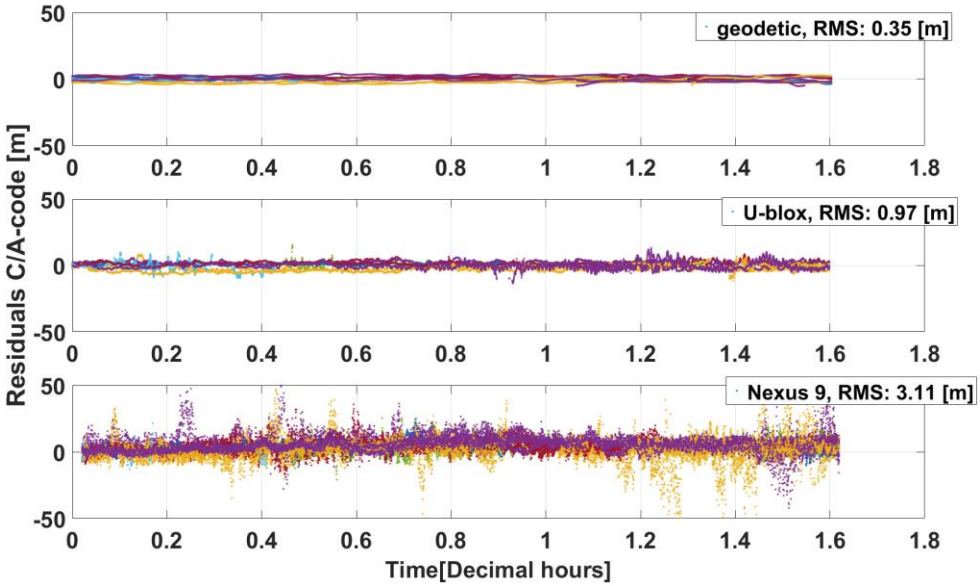

Figure 5.45: C/A-code post-fit residuals from geodetic-grade, u-blox, and Nexus 9

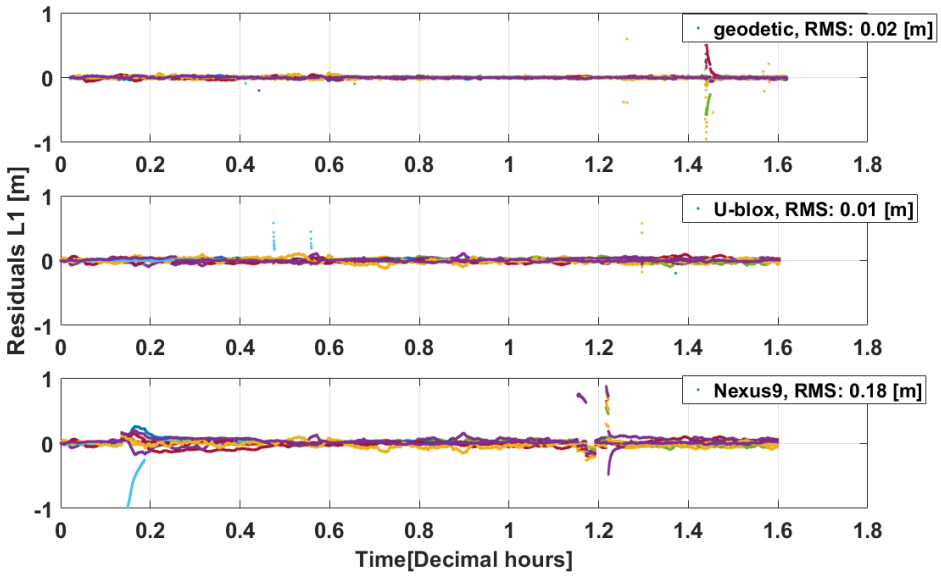

Figure 5.46: Post-fit L1 residuals from geodetic-grade, u-blox, Nexus 9

5.7 Summary and comparison of positioning solutions

To conclude, accuracy metrices from geodetic, low-cost and ultra-low-cost hardware are presented together and compared. Figure 5.47 and Figure 5.48 show the comparison of horizontal and vertical component accuracies from the three grades of GNSS hardware. Figure 5.47 indicates that geodetic-grade and low-cost PPP solution takes approximately 10 minutes to converge to the horizontal error of 0.5 m, whereas the Nexus 9 solution takes about 20 minutes to converge to the same accuracy.

The differences are magnified in the up component as demonstrated in Figure 5.48. The geodetic-grade and low-cost up component converges to <1 m accuracy in about 10 minutes, whereas ultra-low-cost takes few extra minutes of processing to reach the similar accuracy. It is also important to note that the Nexus 9 solution starts-off at a few metres and slowly converges to a few decimetres. The potential reasons for this slow convergence are poor multipath suppression and irregular gain pattern of the cellphone antenna.

Figure 5.49 compares horizontal and vertical rms values from the geodetic-grade, u-blox and Nexus 9 equipment. There is a noticeable difference in the vertical component accuracy of 25 cm of u-blox compared to rms of 51 cm from Nexus 9. Figures 5.47 – 5.49 also suggests that the accuracies from different hardware are comparable after the solution converges, whereas the major difference lies in the convergence period of each solution.

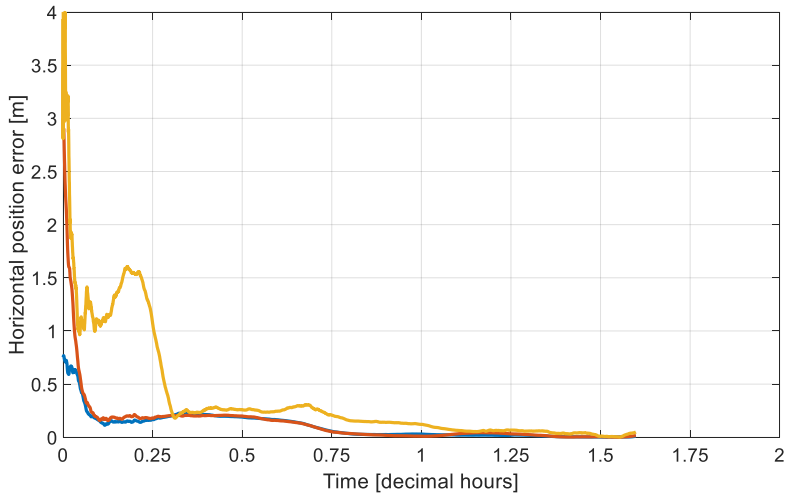

Figure 5.47: Horizontal accuracy comparison of Geodetic grade, u-blox and Nexus 9

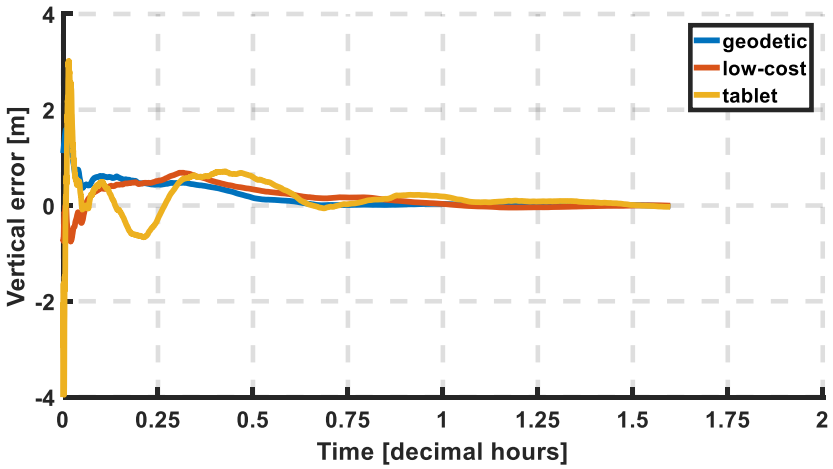

Figure 5.48: Vertical accuracy comparison of geodetic-grade, u-blox and Nexus 9

As presented in the previous sections, C/N_0 values decrease drastically from geodetic-grade to ultra-low-cost hardware, which is the main indicator determining the quality of raw GNSS data. The low-quality (noisier) raw observations are manifesting in the accuracy as well, especially in the vertical component.

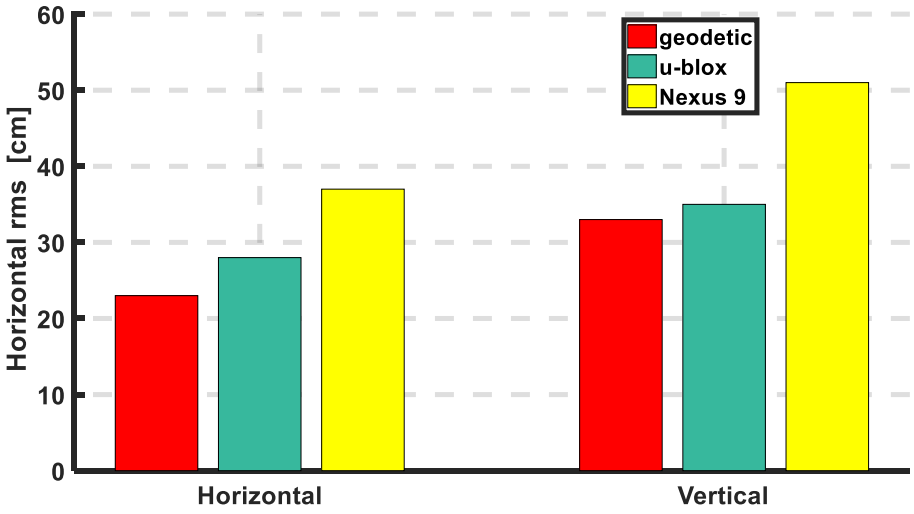

Figure 5.49: Horizontal and vertical rms comparison of geodetic-grade, u-blox and Nexus 9

Chapter 6 Conclusions and future work

As the cost and form factor of the electronic chips are shrinking, GNSS chips are now part of the consumer grade embedded systems such as cellphones, tablets, autonomous navigation systems, watches, wrist-bands, etc. Ever evolving applications such as mobile-mapping, and gaming drives the need for a precise solution to be available at a low cost. The availability of raw GNSS code and carrier-phase measurements from cellphones/tablets open doors for a wide variety of brand new applications such as personal assistance and navigation, infotainment, etc. New applications will allow GNSS to step into the markets which potentially will generate much larger revenues than the traditional surveying and agriculture markets.

6.1 Conclusions

At the time of writing, almost all low-cost and ultra-low-cost GNSS receivers are single-frequency units, which poses challenges in terms of effectively mitigating ionospheric refraction and multipath. The quality of measurements from ultra-low-cost devices are also poor compared to the geodetic-quality measurements.

Single-frequency PPP research prior to this was primarily focused on processing C/A-code and L1 measurements from geodetic-grade receivers. A few researchers have investigated the performance of PPP using medium-cost and low-cost GNSS hardware. Quality of measurements from newer generation of low-cost GNSS chips has improved drastically from last few years. As a result, earlier research findings may not represent the true capabilities of newer generation of low-cost chips. Also, since 2016, pseudorange and carrier-phase measurements are available from tablet/cellphone devices running Android N or higher. This research along with Banville and Van Diggelen (2016) and Riley et al. (2018) are one of the first few to assess PPP performance from a

cellphone GNSS hardware and represents the true positioning capabilities of a cellphone-grade GNSS hardware. A comprehensive comparison of the quality of raw measurements from geodetic-grade, newer generation of low-cost chips and ultra-low-cost (cellphone-grade) GNSS chips is also been made. As the quality of raw measurements deteriorates from geodetic-grade to the cellphone-grade GNSS hardware – different mathematical models are required for each set of hardware to obtain an optimal solution. In this research, an attempt is also made to process data using all three grades of hardware with different mathematical models. In the end, different mathematical models with unique apriori sigma are also purposed for each set of hardware.

This research commences with investigating the single-frequency PPP solution with geodetic-grade hardware. A Kalman filter was implemented to optimize the PPP solution. Quality of raw observations from three different grades of GNSS hardware is also compared. The objective was also to use the best available ionosphere model for each set of hardware.

Software development of the York GNSS single-frequency module was done according to the ANSI C++ standard and on the Microsoft.NET platform. The current version of York GNSS PPP has approximately 150 functions which are structured into appropriate classes and namespaces. The goal of the object-oriented approach is to reduce complexity, enhance re-usability of the existing functions and classes, and increase scalability, so that the current set-up can provide a framework for the future expansion of the software, e.g., adding new constellations, sensor fusion etc.

Geodetic grade data from 6 IGS stations were processed using both the GRAPHIC observable linear combination and the uncombined form. The magnitude of noise on the C/A-code observations from geodetic-grade is low. So, the overall noise of a new phase observable using GRAPHIC combination is low. It was established that GRAPHIC combination performance is

superior to the uncombined form because the magnitude of the signal noise is less than the residual ionospheric error. The GRAPHIC combination eliminates most of the ionospheric delay, whereas GIM is only capable to remove the approximately 75 percent of the delay. Horizontal accuracy of 8.6 cm is established with GRAPHIC compared to the accuracy of 26.2 cm from the uncombined fashion.

On the other hand, it was established that processing observations in uncombined form is superior to the GRAPHIC combination, when processing measurements from low-cost and ultra-low-cost hardware. The primary reason for this is found to be the noisy C/A-code observations. Noisy C/A-code observations from low-cost and ultra-low-cost hardware contaminate the newly formed phase observable. Horizontal positioning accuracy of 21 cm is established from low-cost hardware compared to the accuracy of 67 cm when the GRAPHIC combination is used. Similar trends are also observed with the ultra-low-cost processing. Horizontal positioning accuracy using GRAPHIC is 81 cm, whereas from uncombined observations an accuracy of 35 cm is computed. Using measurements from all four constellations (GPS, GLONASS, Galileo and BeiDou) also further improved the accuracy and convergence time of PPP solution using geodetic hardware.

Different measurement weighting schemes for each set of hardware is also purposed. Optimal results for Nexus 9 data processing is obtained when an apriori code sigma of 5 m is used. To process data from low-cost GNSS receivers a priori sigma of 1.0 m provides the best solution. On the other hand, GRAPHIC and estimated slant ionospheric delay results are found superior to the uncombined (using GIM as corrections) solution when data are processed from geodetic-grade hardware.

York-PPP engine performance is also accessed with multi-constellation single-frequency observations. Single-frequency PPP engine performance is comparable to the high scientific

standard. With geodetic-grade hardware, the horizontal positioning accuracy of 3 cm is established with combined GPS and GLONASS observations.

6.2 Recommendations

A modified weighting scheme for processing data from low-cost and ultra-low-cost GNSS hardware could potentially improve positioning performance. As demonstrated in this study, the carrier-to-noise density ratio of the Nexus 9 measurements does not have any definitve trend with respect to the elevation angle. Satellites with low carrier-to-noise density ratio values are assigned same weights in the estimation process compared to the satellites with reasonble or high values. An altered weigthing scheme in the estimation process can be employed, which takes carrier-to-noise density values of satellites into account.

As the code and the phase bias products for GPS are readily available, future work can also be branched into resolving ambiguities with single-frequency measurements. Resolving ambiguities with ultra-low-cost hardware could be a very tedious task, because of the quality of the raw observations and unmodelled geometric errors.

The single-frequency PPP solution could also be fused with the other sensors such as Inertial Measurement Unit (IMU). This combination could prove to be fruitful with the tablet/cell-phone positioning as both IMUs and a GNSS chip are present on a typical modern cellphone and IMU could provide a serious assistance in filling the gaps, which are left there by the poor quality of the cellphone GNSS antenna.

At the time of this research, the majority of the available cellphone and tablets with duty-cycling off are only able to track GPS and GLONASS satellites. Using Galileo and BeiDou will increase number of visible satellites, redundant observations will help in improving the positioning

accuracy, reliability and the convergence time. York GNSS single-frequency module has already provisions to process measurements from Galileo and BeiDou constellation.

References

Aggrey JE (2015) Multi-GNSS precise point positioning software architecture and analysis of GLONASS pseudorange biases. MSc Thesis, York University

Banville S (2014) Improved convergence for GNSS Precise Point Positioning. PhD Thesis, University of New Brunswick

Banville S, Van Diggelen F (2016) Precise positioning using raw GPS measurements from Android smartphones. GPS World vol 27:43:48

Beran T, Kim D, Langley RB (2003) High-precision single-frequency GPS point positioning. In: Proceedings of ION GPS 2003. Portland, Oregon, pp 9–12

Bisnath S, Gao Y (2009) Current state of precise point positioning and future prospects and limitations. In: Observing our changing earth. Springer, pp 615–623

Bisnath SB, Beran T, Langley R (2002) INNOVATION-Precise Platform Positioning with a Single GPS Receiver-Something new, something old: A previously abandoned technique can position moving platforms with accuracies of a few decimeters. GPS World 13:42–49

Bock H, Jäggi A, Dach R, et al (2009) GPS single-frequency orbit determination for low Earth orbiting satellites. Adv Space Res 43:783–791

Bona P, Tiberius C (2000) An experimental comparison of noise characteristics of seven high-end dual frequency GPS receiver-sets. In: Position Location and Navigation Symposium, IEEE 2000. IEEE, pp 237–244

Braasch MS, Van Dierendonck A (1999) GPS receiver architectures and measurements. Proc IEEE 87:48–64

Cai C, Gong Y, Gao Y, Kuang C (2017) An Approach to Speed up Single-Frequency PPP Convergence with Quad-Constellation GNSS and GIM. Sensors 17:1302. doi: 10.3390/s17061302

Chen K, Gao Y (2005) Real-time precise point positioning using single frequency data. In: Proceedings of ION GNSS. Long Beach, CA, pp 1514–1523

Choy S (2009) An investigation into the accuracy of single frequency Precise Point Positioning (PPP). PhD Dissertation, RMIT University

de Bakker PF, Tiberius CCJM (2017) Real-time multi-GNSS single-frequency precise point positioning. GPS Solut. doi: 10.1007/s10291-017-0653-2

Falcone M, Hahn J, Burger T (2017) Galileo. In: Springer Handbook of Global Navigation Satellite Systems. Springer, pp 247–272

Gelb A (1974) Applied optimal estimation. MIT press, Cambridge,MA

Georgiadou Y, Kleusberg A (1988) On carrier signal multipath effects in relative GPS positioning. Manuscripta Geod 13:172–179

Gill M, Bisnath S, Aggrey J, Seepersad G (2017) Precise Point Positioning (PPP) using Low-Cost and Ultra-Low-Cost GNSS Receivers. In: Proceeedings of the 30th International Technical Meeting of The Satellite Division of the Institute of Navgation (ION GNSS+ 2017). p 11

Grewal MS, Andrews AP (2001) Kalman filtering: theory and practice using MATLAB, 2nd ed. Wiley, New York

Hegarty CJ (2017) The Global Positioning System (GPS). In: Springer Handbook of Global Navigation Satellite Systems. Springer, pp 197–218

Hofmann-Wellenhof B, Lichtenegger H, Wasle E (2007) GNSS–global navigation satellite systems: GPS, GLONASS, Galileo, and more. Springer Science & Business Media

Kaplan ED (ed) (1996) Understanding GPS: principles and applications. Artech House, Boston

Kaplan ED, Hegarty C (eds) (2006) Understanding GPS: principles and applications, 2nd ed. Artech House, Boston

Kirkko-Jaakkola M, Söderholm S, Honkala S, et al (2015) Low-Cost Precise Positioning Using a National GNSS Network. In: ION GNSS+ 2015, Session E1, Tampa, FL, USA

Kouba J (2009) A guide to using International GNSS Service (IGS) products

Kouba J, Héroux P (2001) Precise point positioning using IGS orbit and clock products. GPS Solut 5:12–28

Landau H, Chen X, Klose S, et al (2009) Trimble's RTK and DGPS solutions in comparison with precise point positioning. In: Observing our Changing Earth. Springer, pp 709–718

Langley RB, Teunissen PJ, Montenbruck O (2017) Introduction to GNSS. In: Springer Handbook of Global Navigation Satellite Systems. Springer, pp 3–23

Laurichesse D, Blot A (2016) Fast PPP Convergence Using Multi-Constellation and Triple-Frequency Ambiguity Resolution. In: Proceedings of the 29th International Technical Meeting of The Satellite Division of the Institute of Navigation (ION GNSS+ 2016). pp 2082–2088

Le AQ, Tiberius C (2006) Single-frequency precise point positioning with optimal filtering. GPS Solut 11:61–69. doi: 10.1007/s10291-006-0033-9

Leick A (1995) GPS satellite surveying, 2nd ed. Wiley, New York

Leick A, Rapoport L, Tatarnikov D (2015) GPS satellite surveying, 4th ed. John Wiley & Sons

Li X, Zhang X, Ren X, et al (2015) Precise positioning with current multi-constellation Global Navigation Satellite Systems: GPS, GLONASS, Galileo and BeiDou. Sci Rep 5:8328. doi: 10.1038/srep08328

Lou Y, Zheng F, Gu S, et al (2016) Multi-GNSS precise point positioning with raw single-frequency and dual-frequency measurement models. GPS Solut 20:849–862. doi: 10.1007/s10291-015-0495-8

Mader GL (1999) GPS antenna calibration at the National Geodetic Survey. GPS Solut 3:50–58

Mander A (2011) Constrained GPS-based precise orbit determination of low earth orbiters. MSc Thesis, York University

Maybeck PS (1982) Stochastic models, estimation, and control. Academic press, New York

Misra P, Enge P (2006) Global Positioning System: Signals, Measurements and Performance, 2nd edn. Ganga-Jamuna Press, Massachusetts

Moernaut GJ, Orban D (2009) An Introduction to Bandwidth, Gain Pattern, Polarization, and All That. GPS World 20:42

Montenbruck O (2003) Kinematic GPS positioning of LEO satellites using ionosphere-free single frequency measurements. Aerosp Sci Technol 7:396–405. doi: 10.1016/S1270-9638(03)00034-8

Muellerschoen RJ, Iijima B, Meyer R, et al (2004) Real-time point positioning performance evaluation of single-frequency receivers using NASA's global differential GPS system. Pasadena, CA: Jet Propulsion Laboratory, National Aeronautics and Space Administration

Øvstedal O (2002) Absolute positioning with single-frequency GPS receivers. GPS Solut 5:33–44

Pan L, Zhang X, Li X, et al (2017) Characteristics of inter-frequency clock bias for Block IIF satellites and its effect on triple-frequency GPS precise point positioning. GPS Solut 21:811–822. doi: 10.1007/s10291-016-0571-8

Parkinson BW, Spilker JJ (1996) The global positioning system: theory and applications. American Institute of Aeronautics and Astronautics, Washington, DC

Pesyna KM, Heath RW, Humphreys TE (2014) Centimeter positioning with a smartphone-quality GNSS antenna. In: Proceedings of the ION GNSS+ Meeting. Tampa, FL, pp 1568–1577

Rao BR, Fante R, Waldemar K (2012) GPS/GNSS Antennas. Artech House, Boston, MA

Revnivykh S, Bolkunov A, Serdyukov A, Montenbruck O (2017) GLONASS. In: Springer Handbook of Global Navigation Satellite Systems. Springer, pp 219–245

Riley S, Landau H, Gomez V, et al (2018) Positioning with Android:GNSS observables. GPS World 29:14

Rothacher M, Beutler G, Mervart, L (1996) The perturbation of the orbital elements of GPS satellites through direct radiation pressure and Y-bias. In: Proceedings of the IGS Workshop" Special Topics and New Directions"

Schaer S, Gurtner W, Feltens J (1998) IONEX: The ionosphere map exchange format version 1. In: Proceedings of the IGS AC Workshop, Darmstadt, Germany

Seepersad G (2012) Reduction of initial convergence period in GPS PPP data processing. MSc Thesis, York University

Shen X (2002) Improving ambiguity convergence in carrier phase-based PPP. MSc Thesis, University of Calgary, Department of Geomatics Engineering

Simsky A (2006) Standalone Real-time Navigation Algorithm for Single-frequency Ionosphere-free Positioning Based on Dynamic Ambiguities (DARTS-SF). In: Proceedings of ION GNSS 18th International Technical Meeting of the Satellite Division, Fort Worth, Texas. p pp.301-308

Sterle O, Stopar B, Pavlovčič Prešeren P (2015) Single-frequency precise point positioning: an analytical approach. J Geod. doi: 10.1007/s00190-015-0816-2

Teunissen P (1991) The GPS phase-adjusted pseudorange. In: Proceedings of the 2nd international workshop on high precision navigation Stuttgart/Freudenstadt, Germany. pp 115–125

Teunissen P, Montenbruck O (2017) In Springer handbook of global navigation satellite systems, (eds). Springer, Berlin

Teunissen PJ, Kleusberg A (1996) GPS observation equations and positioning concepts. In: GPS for Geodesy. Springer, pp 175–217

van Bree RJP, Tiberius CCJM (2012) Real-time single-frequency precise point positioning: accuracy assessment. GPS Solut 16:259–266. doi: 10.1007/s10291-011-0228-6

Verhagen S, Teunissen PJ (2017) Least-Squares Estimation and Kalman Filtering. In: Springer Handbook of Global Navigation Satellite Systems. Springer, pp 639–660

Wang J-H (2005) Intelligent MEMS INS/GPS integration for land vehicle navigation. PhD Dissertation, University of Calgary

Wells D, Beck N, Delikaraoglou D, et al (1999) Guide to GPS Positioning, Canadian GPS Associates. University of New Brunswick, Fredericton, N.B., Canada

Wienia RJ (2008) Use of global ionospheric maps for precise point positioning. MSc Thesis, Delft University of Technology

Witchayangkoon B (2000) Elements of GPS precise point positioning. PhD Dissertation, The University of Maine, USA

Yang Y, Tang J, Montenbruck O (2017) Chinese navigation satellite system. In: Springer Handbook of Global Navigation Satellite Systems. Springer, pp 273–304

Yunck TP (1993) Coping with the atmosphere and ionosphere in precise satellite and ground positioning. Geophys Monogr vol.13:1–16

Zhu SY, Massmann F-H, Yu Y, Reigber C (2003) Satellite antenna phase center offsets and scale errors in GPS solutions. J Geod 76:668–672. doi: 10.1007/s00190-002-0294-1

Zumberge JF, Heflin MB, Jefferson DC, et al (1997) Precise point positioning for the efficient and robust analysis of GPS data from large networks. J Geophys Res Solid Earth 1978–2012 102:5005–5017